Predictive Design of Ultrastretchable Electrodes with Strain-Insensitive Performance *via* Machine Intelligence

Haochen Yang[a], Qiongyu Chen[b], Tianle Chen[a], Yang Li[a], Elizabeth A. Norris[a], Joshua M. Little[a], Jiayue Sun[c], Snehi Shrestha[a], Shenqiang Ren[d], Teng Li[b*] & Po-Yen Chen[a,e,*]

[a] Department of Chemical and Biomolecular Engineering, University of Maryland, College Park, MD 20742, United States

[b] Department of Mechanical Engineering, University of Maryland, College Park, MD 20742, United States

[c] Department of Chemistry, University of Maryland, College Park, MD 20742, United States

[d] Department of Materials Science and Engineering, University of Maryland, College Park, MD 20742, United States

[e] Maryland Robotics Center, College Park, MD 20742, United States

* Email: lit@umd.edu (T.L.)

checp@umd.edu (P.-Y. C.)

Keywords: Conductive interlayers; machine learning; collaborative robotics; stretchable gold conductors; strain-resilient zinc batteries.

Table of Content

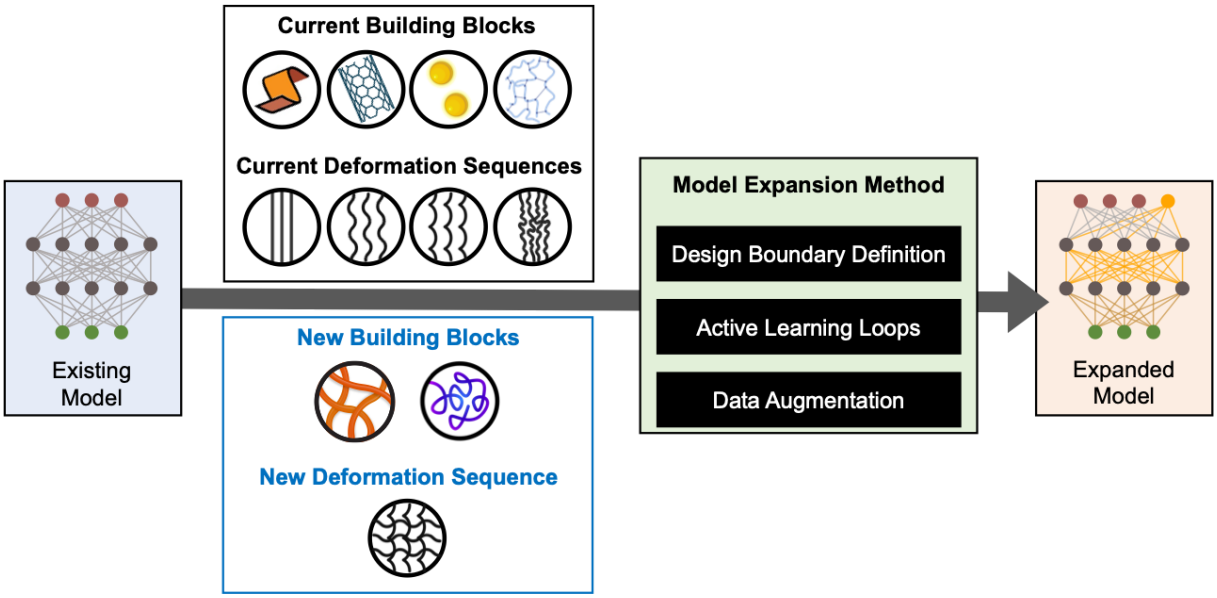

Fig. S1. Schematic illustration of a model expansion strategy. Workflow of a model expansion method.

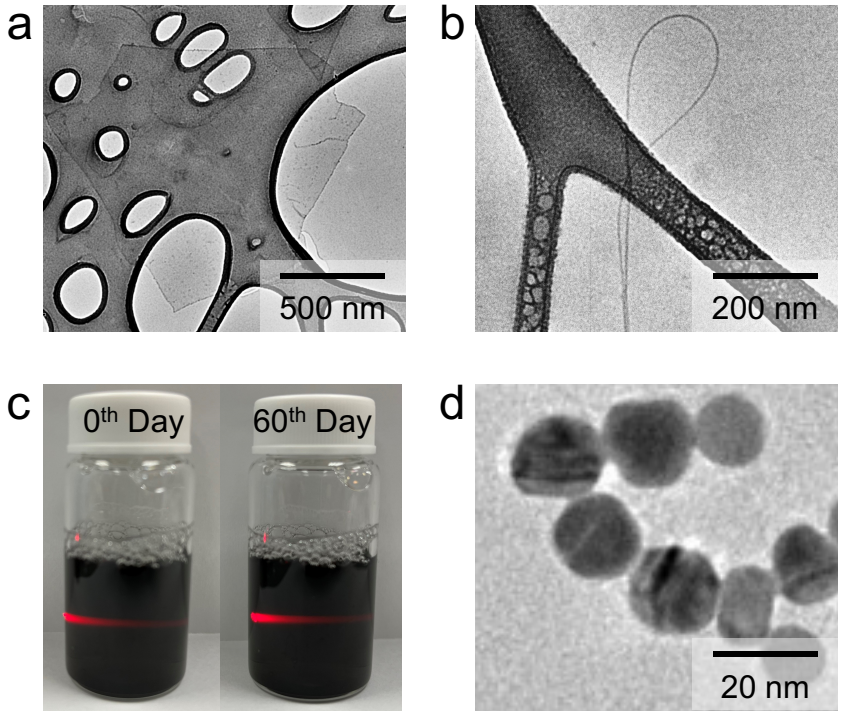

Fig. S2. Characterization of building blocks. (**a**) TEM image of $Ti_3C_2T_x$ MXene nanosheets, with an average lateral dimension of 1 × 1 μm^2. (**b**) TEM image of single-walled carbon nanotubes (SWNTs), with an average diameter of 1 nm and an average length of 10 μm. (**c**) Tyndall effect of SWNT dispersion that contained sodium dodecyl sulfate (SDS). No SWNT aggregation was observed after ambient storage for 60 days. (**d**) TEM image of gold nanoparticles (AuNPs), with an average diameter of 20 nm.

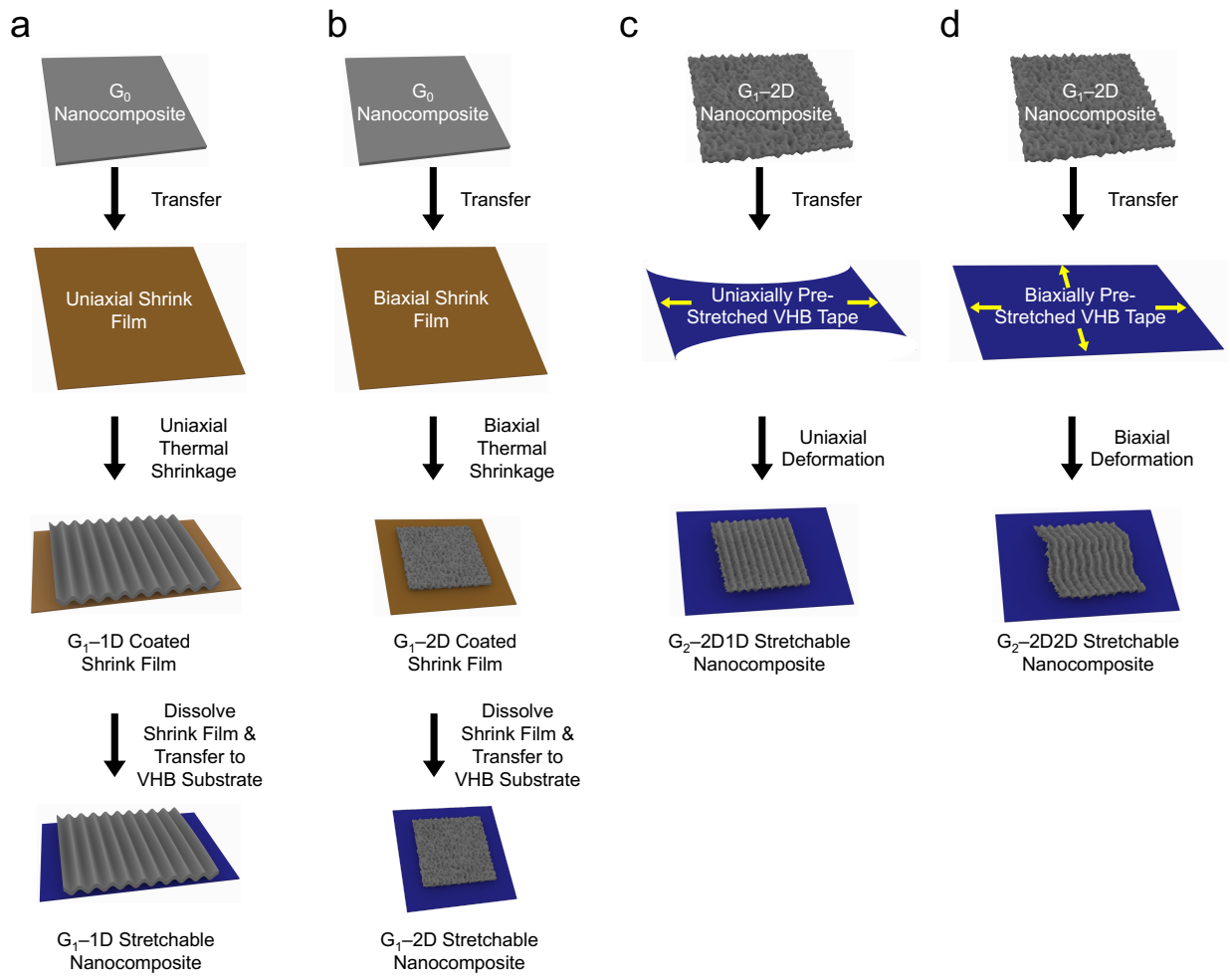

Fig. S3. Fabrication of G_1/G_2 stretchable nanocomposites. (**a**) Fabrication of G_1–1D stretchable nanocomposites using uniaxial shrink films. (**b**) Fabrication of G_1–2D stretchable nanocomposites using biaxial shrink films. (**c**) Fabrication of G_2–2D1D stretchable nanocomposites using biaxial shrink films and uniaxially pre-stretched VHB substrates sequentially. (**d**) Fabrication of G_2–2D2D stretchable nanocomposites using biaxial shrink films and biaxially pre-stretched VHB substrates sequentially.

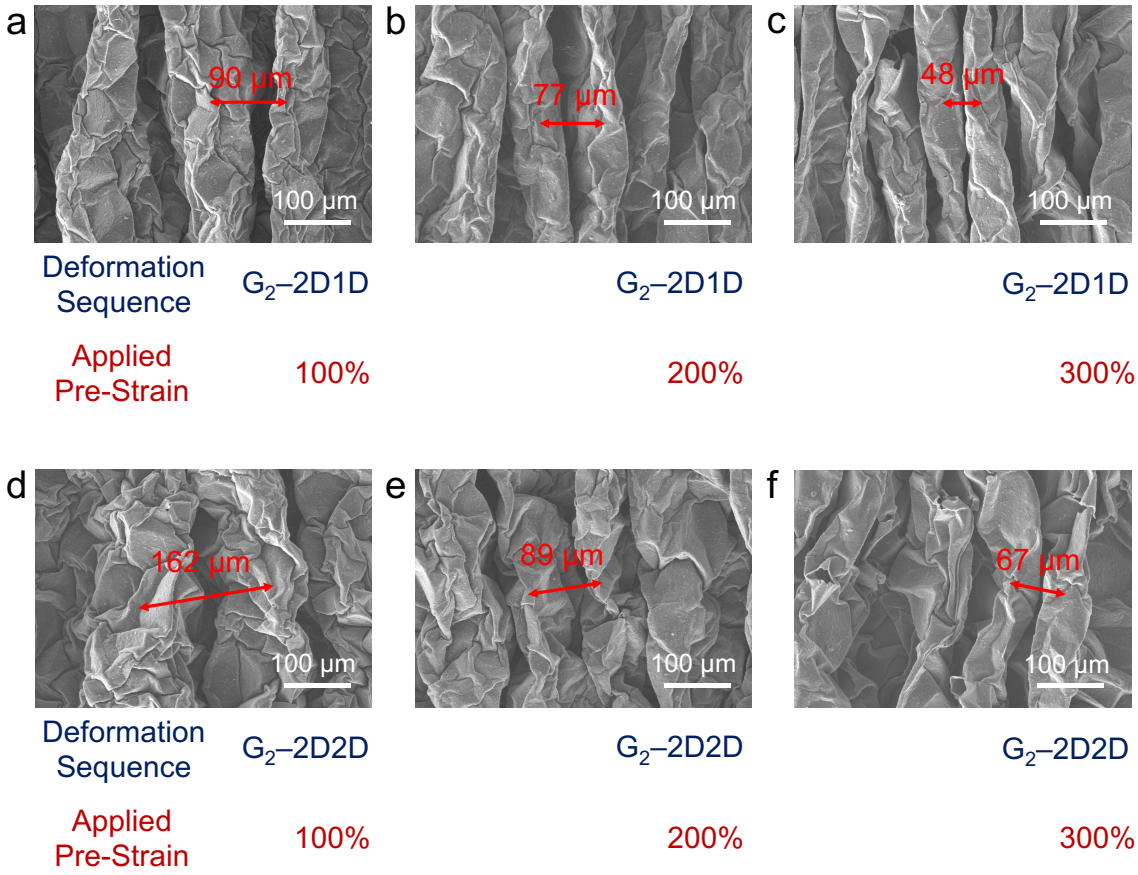

Fig. S4. Tunable wavelengths of G_2–2D1D and G_2–2D2D stretchable nanocomposites. (**a**)–(**c**) Wavelengths of G_2–2D1D stretchable nanocomposites were tunable from 90 to 48 μm by controlling the applied pre-strains of VHB substrates from 100% to 300%, respectively. (**d**)–(**f**) Wavelengths of G_2–2D2D stretchable nanocomposites were tunable from 162 to 67 μm by controlling the applied pre-strains of VHB substrates from 100% to 300%, respectively.

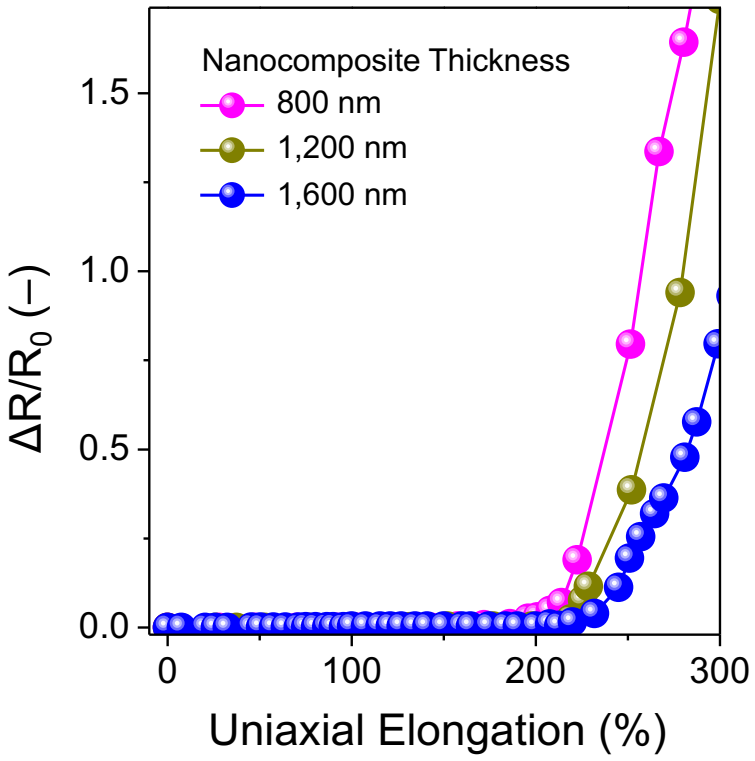

Fig. S5. Effect of thickness on the resistance–elongation curves of G_1/G_2 stretchable nanocomposites. Resistance–elongation curves of various G_2–2D1D stretchable nanocomposites with different thicknesses. All G_2–2D1D nanocomposites were at the same MXene/SWNT/AuNP/PVA ratio of 45/45/8/2, and the applied pre-strain was controlled to be the same at 100%.

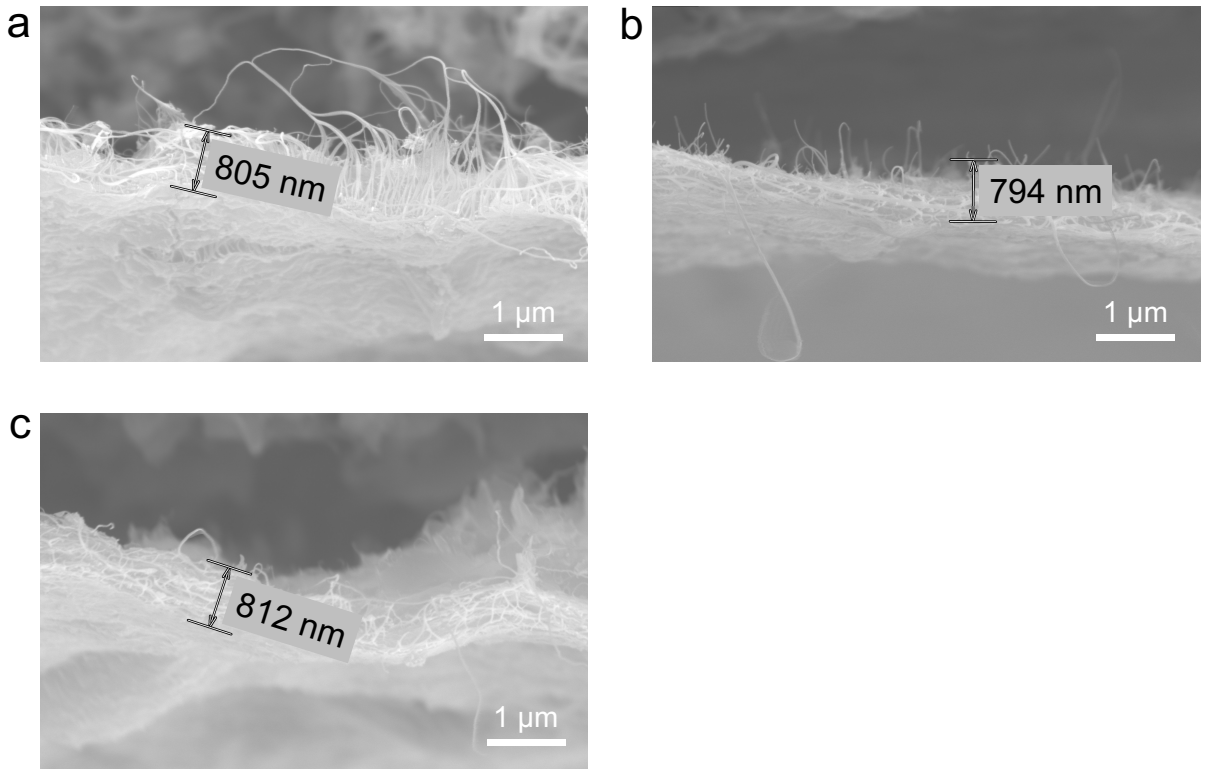

Fig. S6. Fabrication of G_0 nanocomposites with controlled thicknesses. During the SVM model construction, the thicknesses of all G_0 nanocomposites were controlled to be ~800 nm. The MXene/SWNT/AuNP/PVA ratios of three G_0 nanocomposites were (**a**) 10.1/79.5/5.7/4.7, (**b**) 40.3/41.2/8.7/9.8, and (**c**) 61.2/25.3/12.4/1.1.

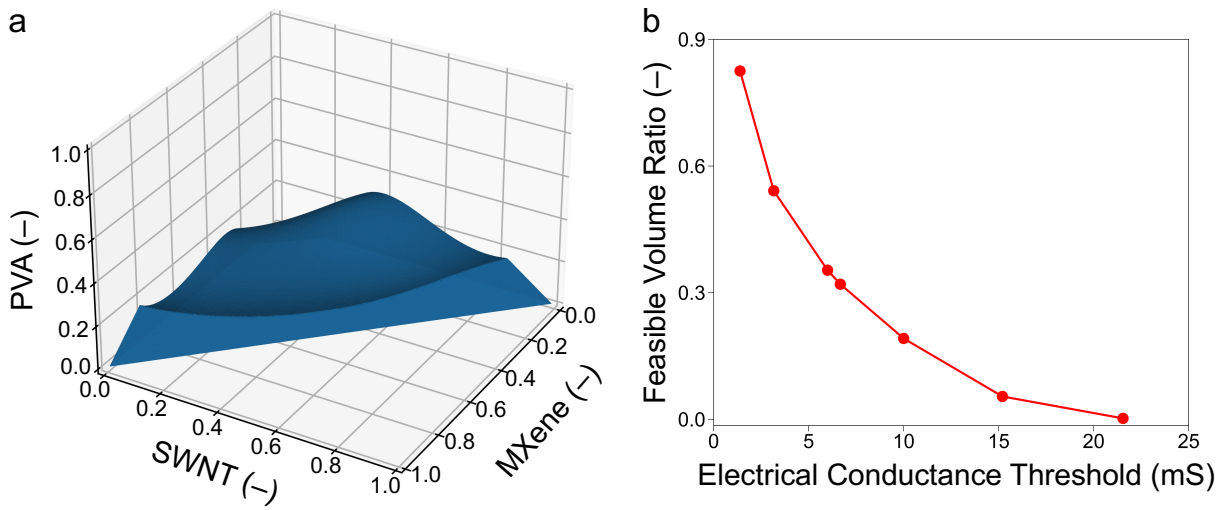

Fig. S7. Determination of a feasible parameter space. (**a**) Feasible parameter space of G_0 nanocomposites with high electrical conductance values >6.67 mS. (**b**) By selecting the iso-surfaces with different electrical conductance values, the volume of a feasible parameter space changed accordingly. By setting the electrical conductance value of 6.67 mS as the threshold, a feasible parameter space was defined and held ~34% of the entire parameter space.

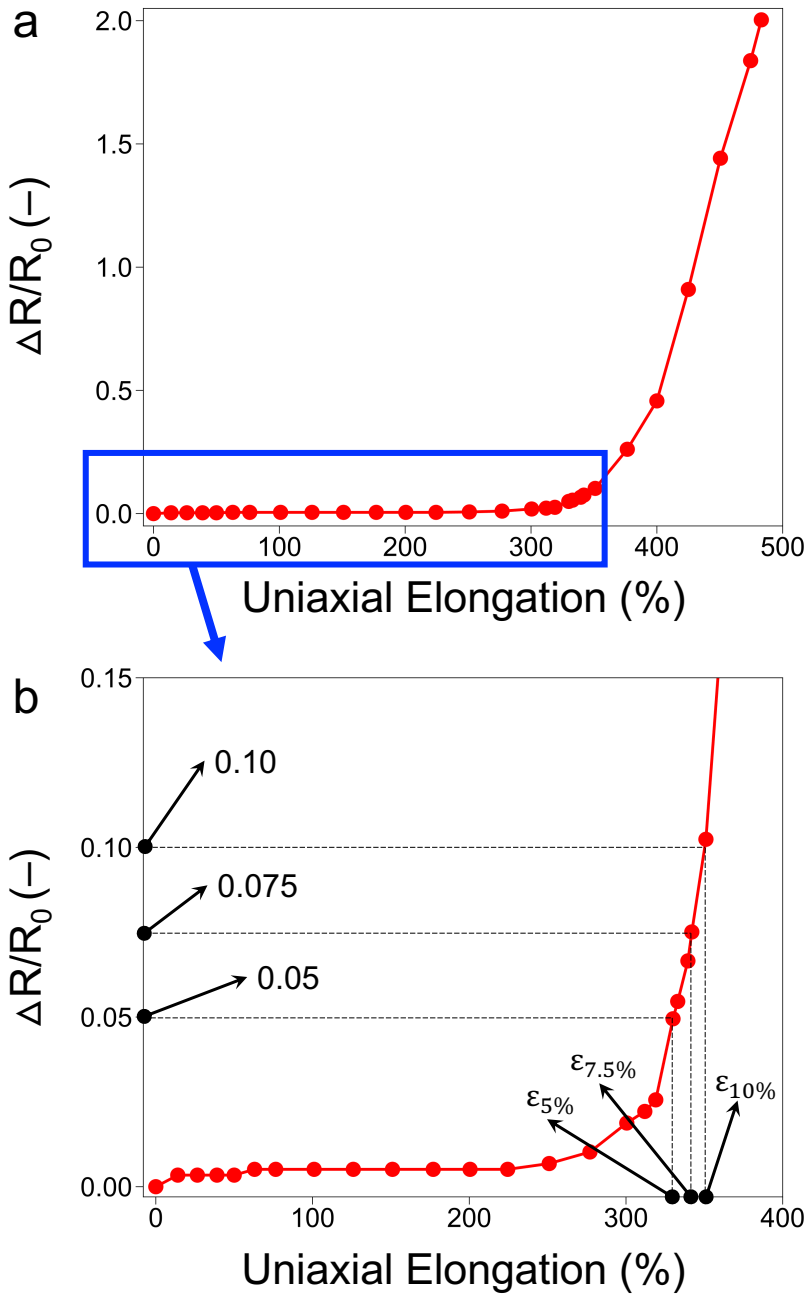

Fig. S8. Response labels of G_1/G_2 stretchable nanocomposites. A resistance–elongation profile of a G_2–2D1D stretchable nanocomposite was used as an example. $\varepsilon_{5\%}$ represents the uniaxial elongation that increases the initial resistance (R_0) by 5%. $\varepsilon_{7.5\%}$ represents the uniaxial elongation that increases R_0 by 7.5%. $\varepsilon_{10\%}$ represents the uniaxial elongation that increases R_0 by 10%.

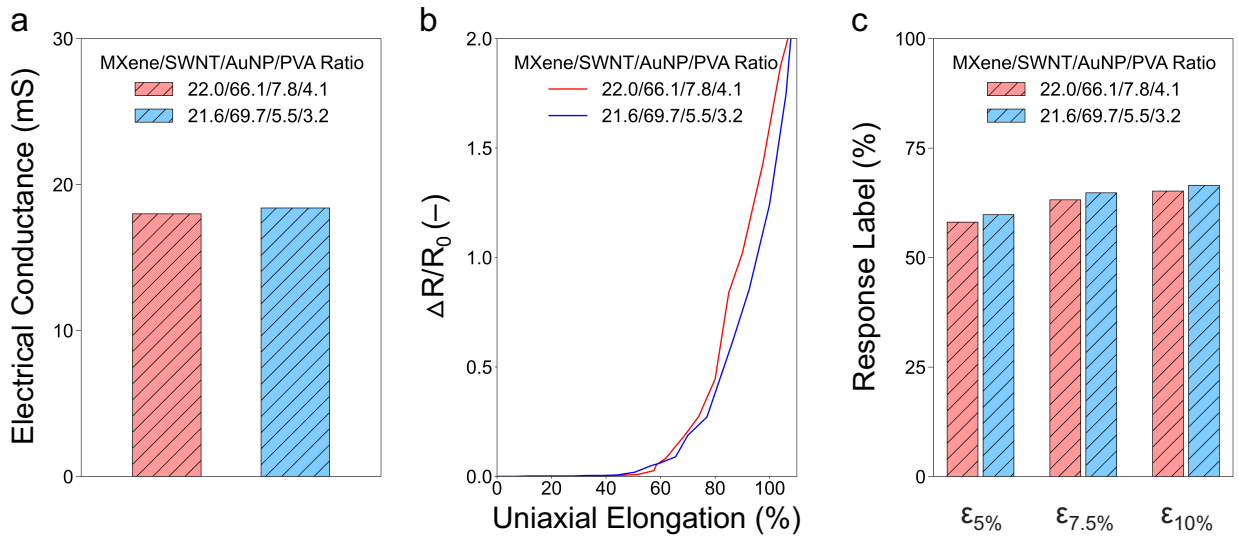

Fig. S9. Performance of G_1/G_2 stretchable nanocomposites upon slight composition variations. With slight variations in the MXene/SWNT/AuNP/PVA ratio (22.0/66.1/7.8/4.1 *vs.* 21.6/69.7/5.5/3.2), two G_1–2D stretchable nanocomposites were fabricated and demonstrated similar (**a**) electrical conductance values (i.e., S_0), (**b**) resistance–elongation curves, and (**c**) response labels (i.e., $\varepsilon_{5\%}, \varepsilon_{7.5\%}, \varepsilon_{10\%}$).

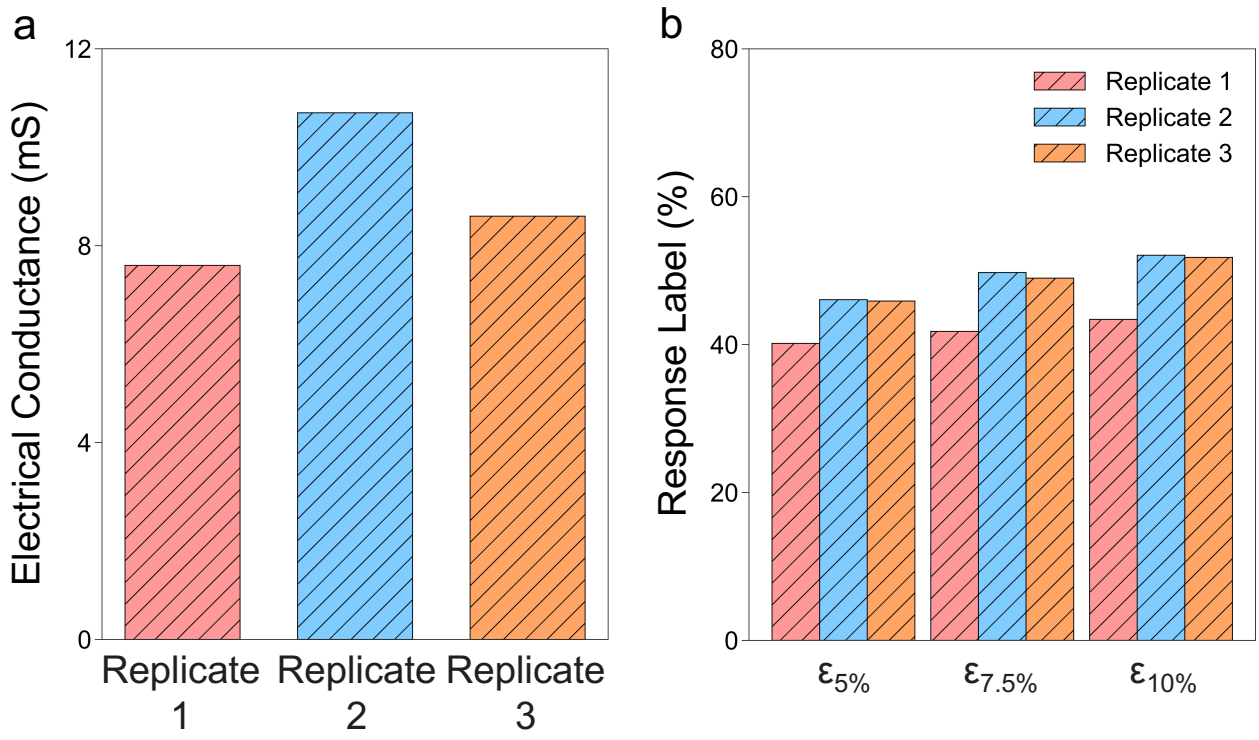

Fig. S10. Measurement variations across G_1/G_2 stretchable nanocomposite replicates. A set of fabrication parameters was used to prepare three G_1–2D replicates, including the MXene/SWNT/AuNP/PVA ratio of 45/45/8/2, the nanocomposite thickness of 1,200 nm, and the deformation sequence of G_1–2D. (**a**) Electrical labels (i.e., S_0) of three G_1–2D replicates. (**b**) Response labels (i.e., $\varepsilon_{5\%}$, $\varepsilon_{7.5\%}$, $\varepsilon_{10\%}$) of three G_1–2D replicates.

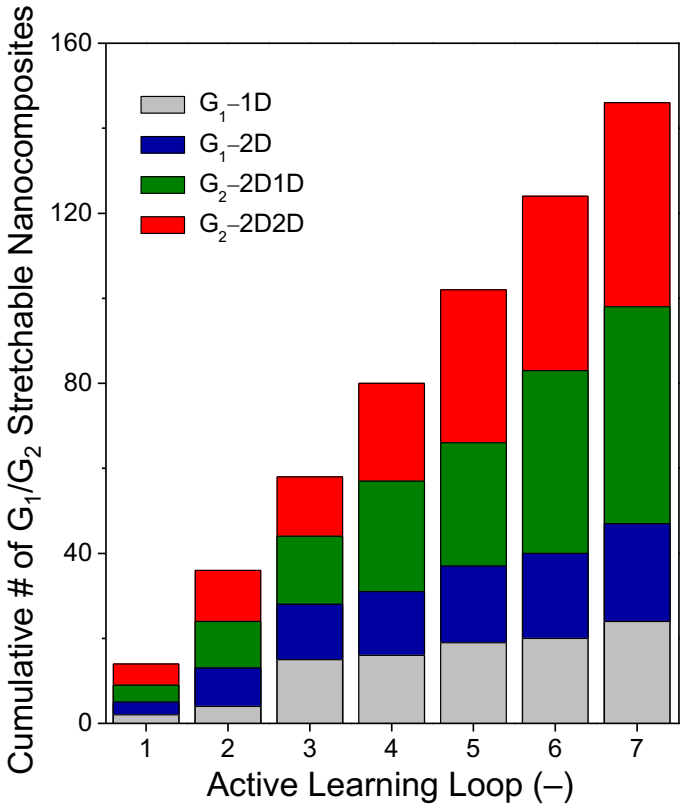

Fig. S11. Cumulative numbers of G_1/G_2 stretchable nanocomposites fabricated across active learning loops. 146 G_1/G_2 stretchable nanocomposites were fabricated across 7 active learning loops, including 24 G_1–1D, 23 G_1–2D, 51 G_2–2D1D, and 48 G_2–2D2D stretchable nanocomposites.

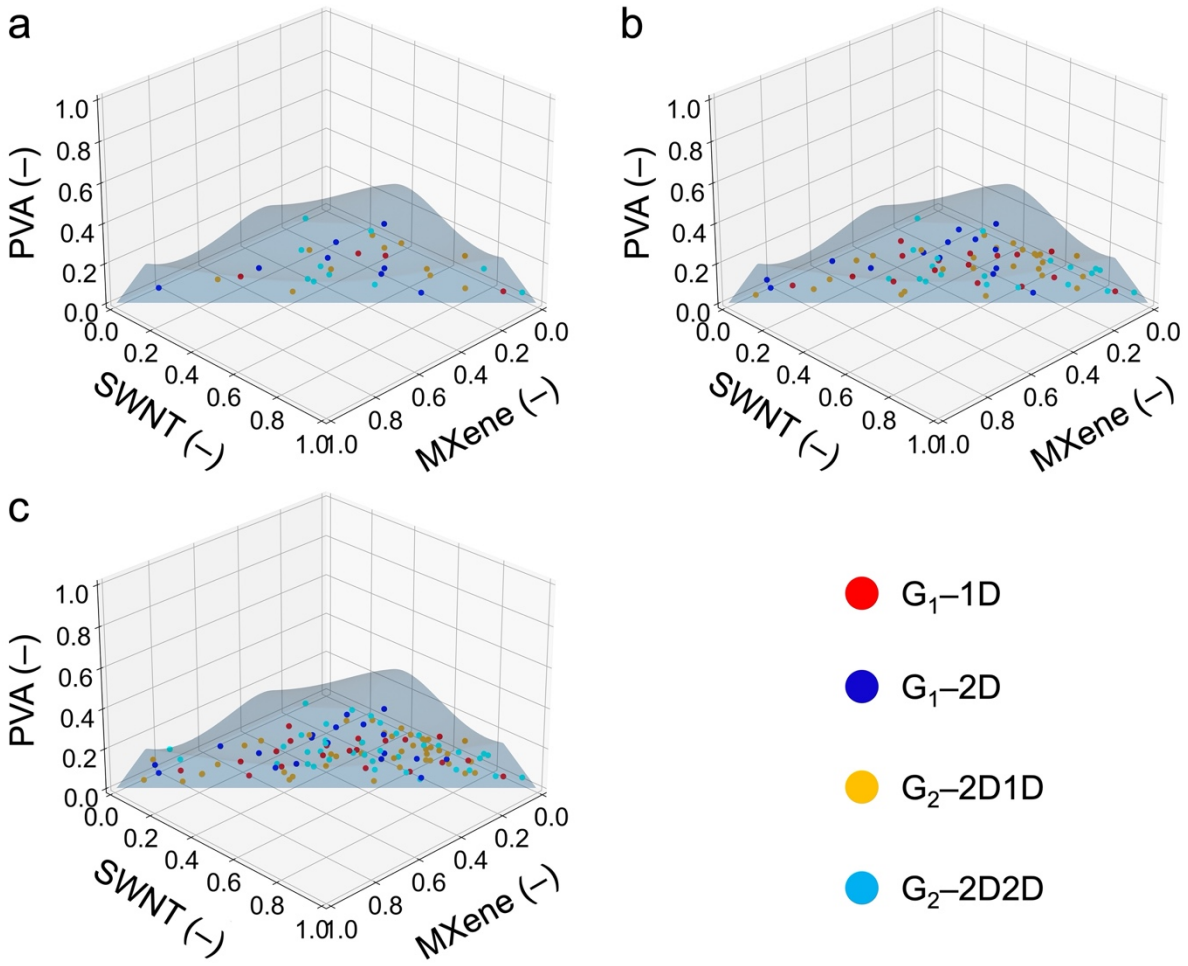

Fig. S12. Spatial distributions of G_1/G_2 stretchable nanocomposites in the feasible parameter space. (**a**) After 2 loops. (**b**) After 4 loops. (**c**) After 6 loops.

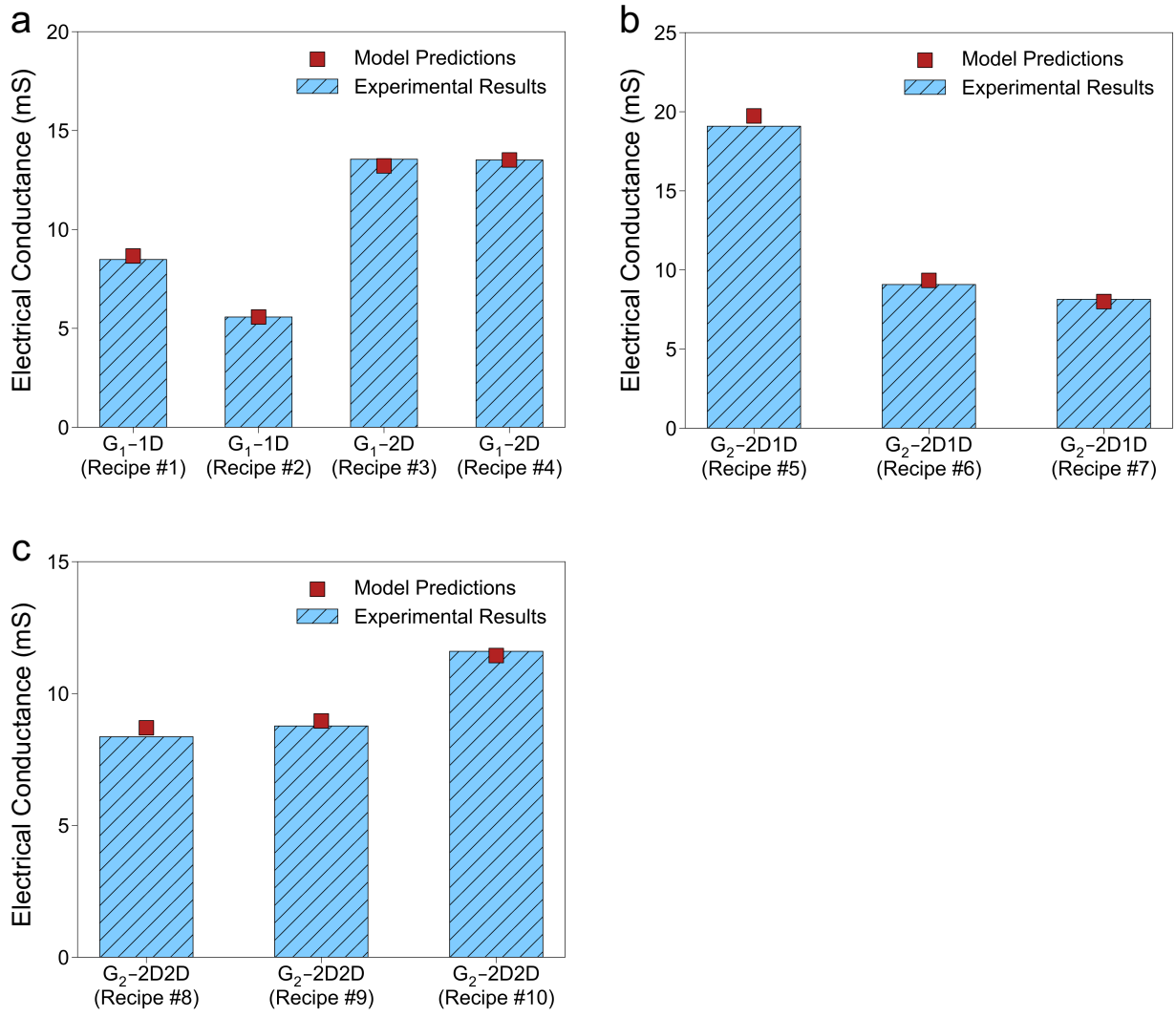

Fig. S13. Comparison between model-predicted and actual electrical conductance. (**a**) G_1–1D and G_1–2D stretchable nanocomposites. (**b**) G_2–2D1D stretchable nanocomposites. (**c**) G_2–2D2D stretchable nanocomposites.

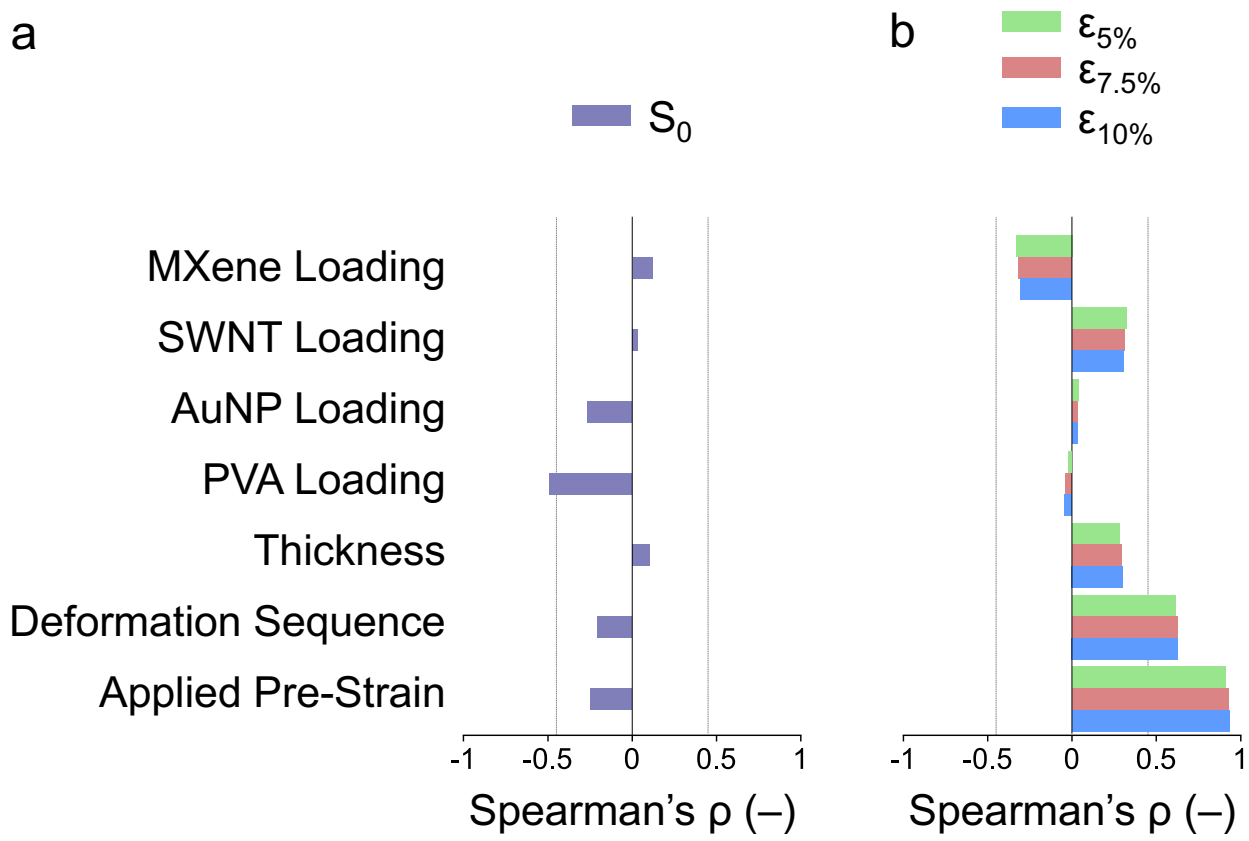

Fig. S14. Statistical analyses between fabrication parameters and nanocomposite properties. Spearman's ρ of MXene loading, SWNT loading, AuNP loading, and PVA loading, nanocomposite thickness, deformation sequence, and applied pre-strain on (**a**) the electrical label (i.e., S_0) and (**b**) the response labels (i.e., $\varepsilon_{5\%}$, $\varepsilon_{7.5\%}$, $\varepsilon_{10\%}$). **Fig. S14a** shows that the PVA loading was negatively correlated with S_0. **Fig. S14b** shows that the deformation sequence and applied pre-strain were positively correlated with three response labels.

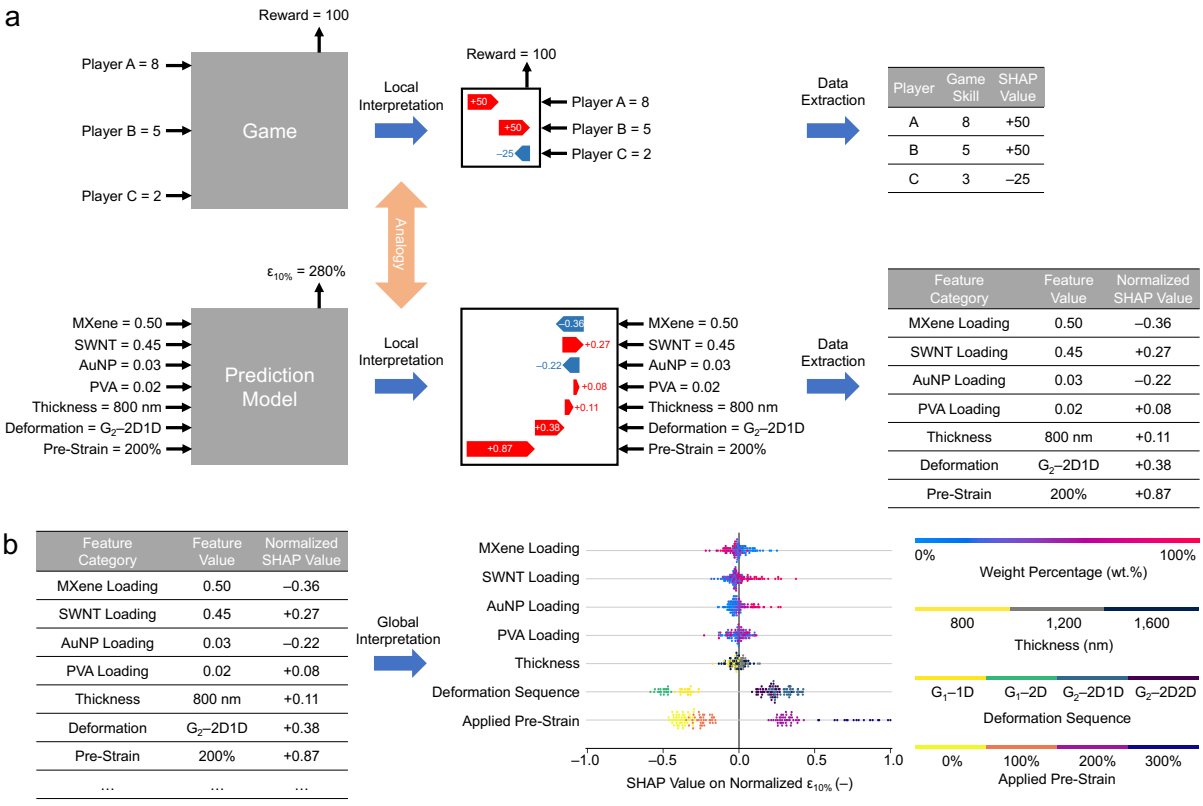

Fig. S15. Working mechanism of SHAP model interpretation. (**a**) An analogy between the interpretation of a specific game and the interpretation of a prediction model. The blue and red bars are the SHAP values (positive as red and negative as blue). (**b**) Figure plotting to get the global interpretation of the prediction model by using the SHAP values of every feature for every data point.

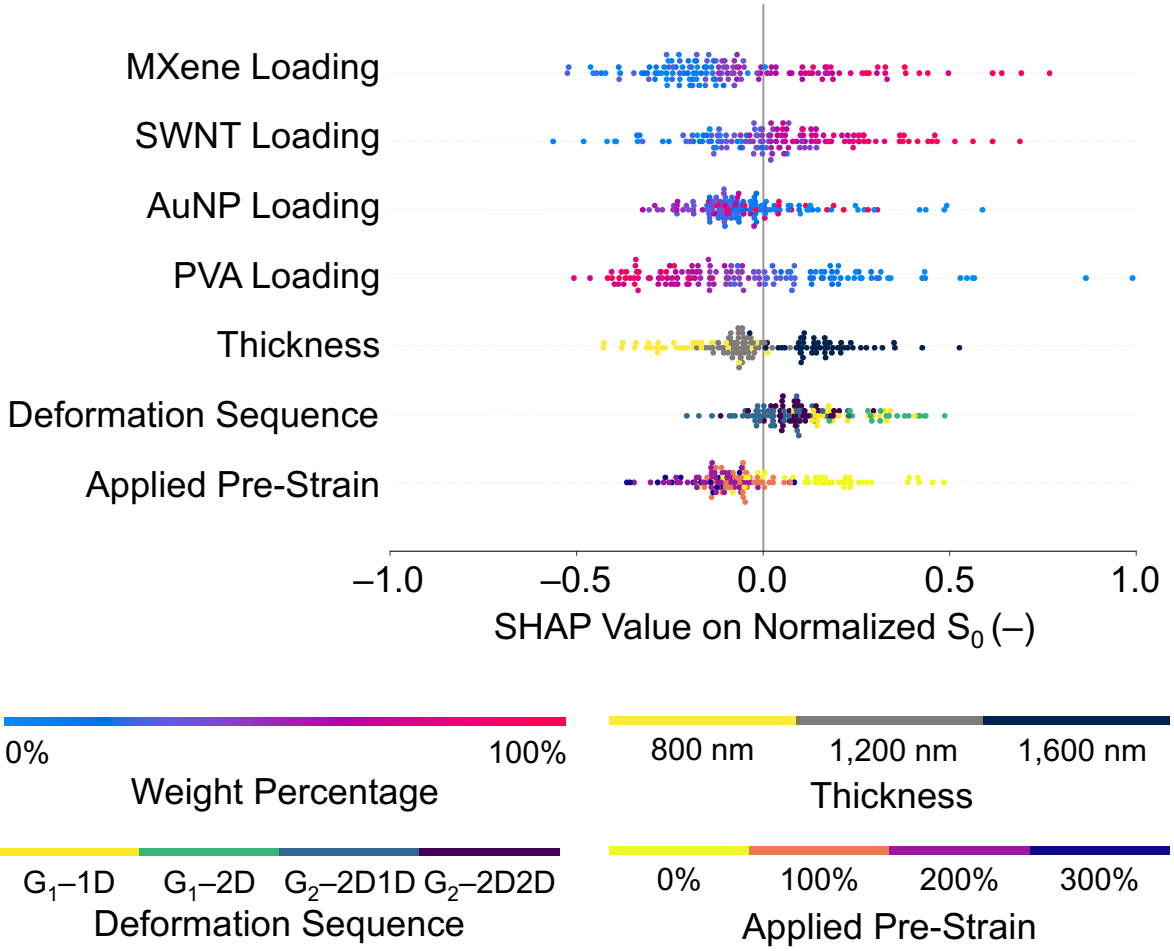

Fig. S16. SHAP interpretation on the S_0 of G_1/G_2 stretchable nanocomposites. Normalized SHAP values of MXene loading, SWNT loading, AuNP loading, PVA loading, nanocomposite thickness, deformation sequence, and applied pre-strain on the S_0 of G_1/G_2 stretchable nanocomposites.

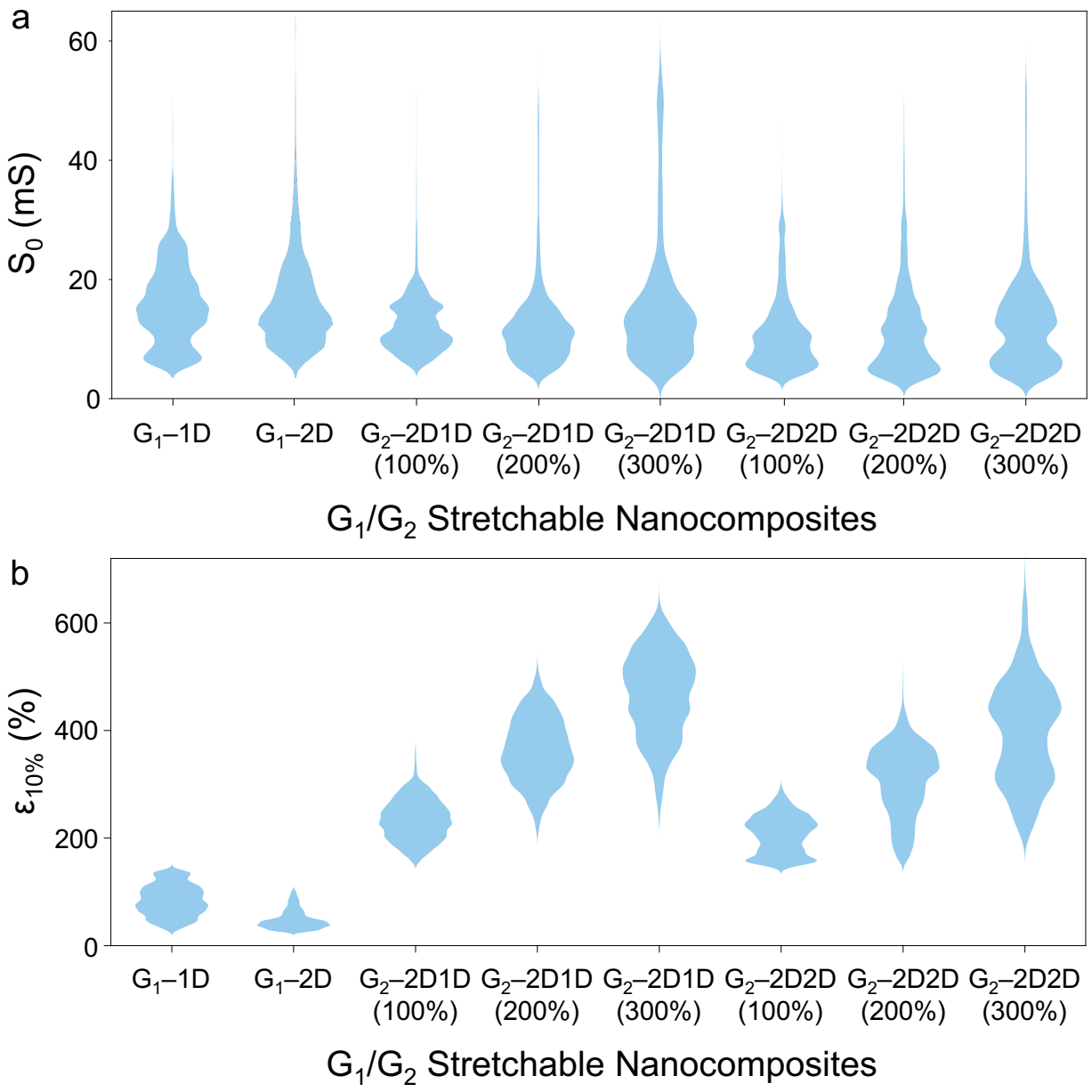

Fig. S17. Violin plots of G_1/G_2 stretchable nanocomposites. (**a**) The electrical label (i.e., S_0) was less responsive to the deformation sequence and applied pre-strain during the fabrication of G_1/G_2 stretchable nanocomposites. (**b**) The response labels (e.g., $\varepsilon_{10\%}$) was highly responsive to the deformation sequence and applied pre-strain during the fabrication of G_1/G_2 stretchable nanocomposites.

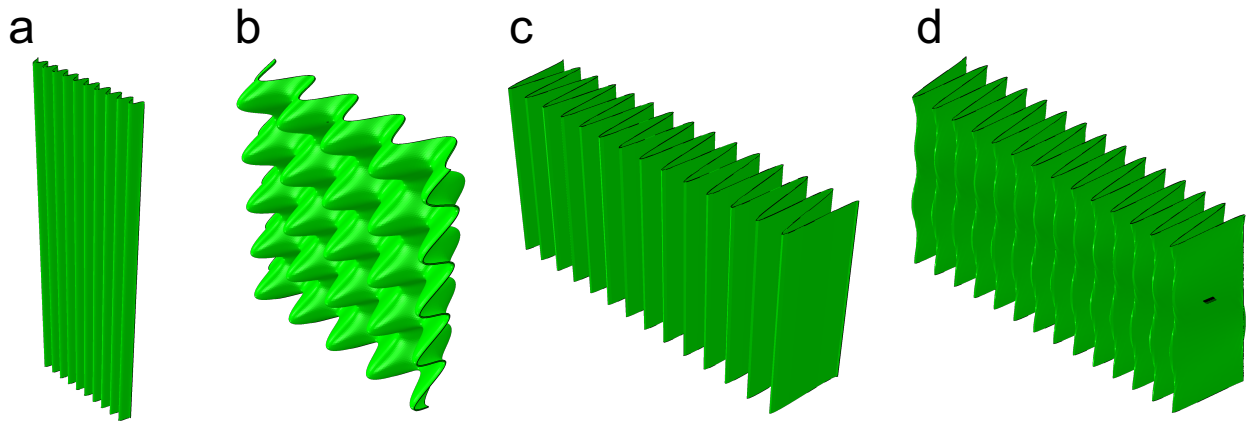

Fig. S18. Two-scale FE models of G_1/G_2 stretchable nanocomposites. (**a**) FE model of a G_1–2D stretchable nanocomposite. The checkerboard mode was utilized to describe the isotropic crumples. (**b**) FE model of a G_2–2D1D stretchable nanocomposite. (**c**) FE model of a G_2–2D1D stretchable nanocomposite. On the small scale, the checkerboard mode was utilized to describe the isotropic crumples. At the large scale, cylindrical (wavy) mode was utilized to depict the parallel wrinkles. (**d**) FE model of a G_2–2D2D stretchable nanocomposite. On the small scale, the checkerboard mode was utilized to describe the isotropic crumples. At the large scale, undulating (*S*-shape) mode was utilized to depict the curvy wrinkles.

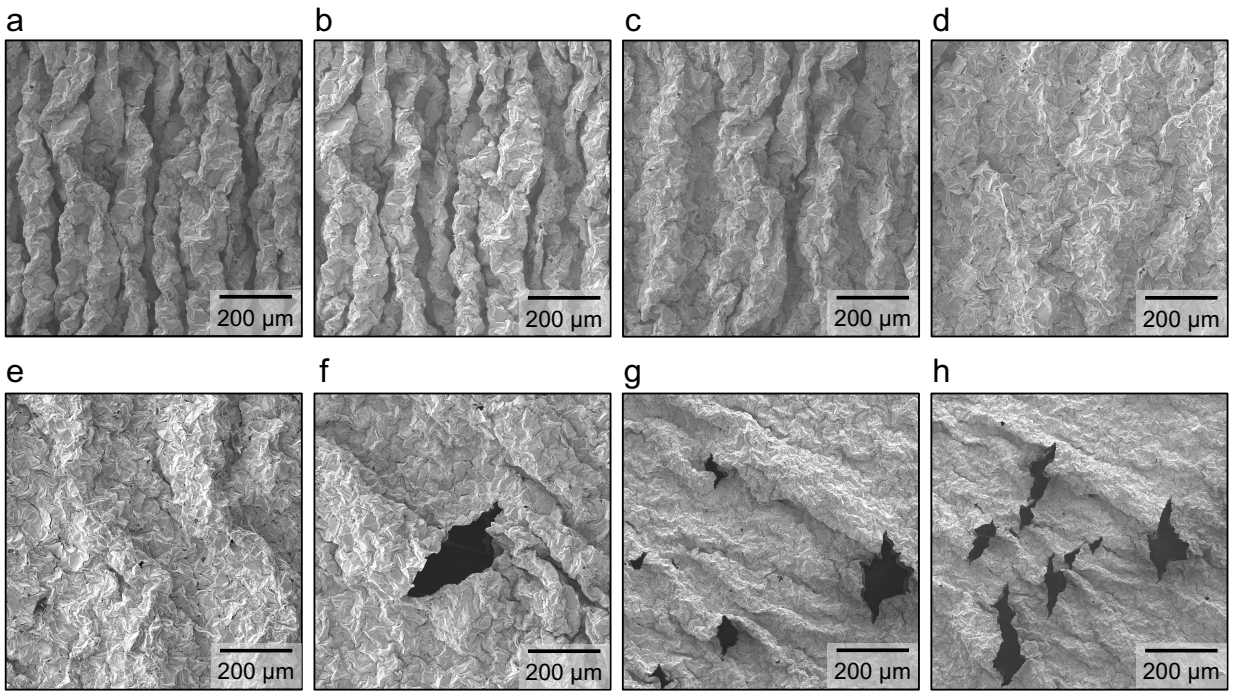

Fig. S19. SEM images of a G_2–2D2D gold conductor during a continuous elongation loading process from 0% to 1,300%. (**a**) 100%. (**b**) 200%. (**c**) 400%. (**d**) 600%. (**e**) 800%. (**f**) 1,000%. (**g**) 1,200%. (**h**) 1,300%.

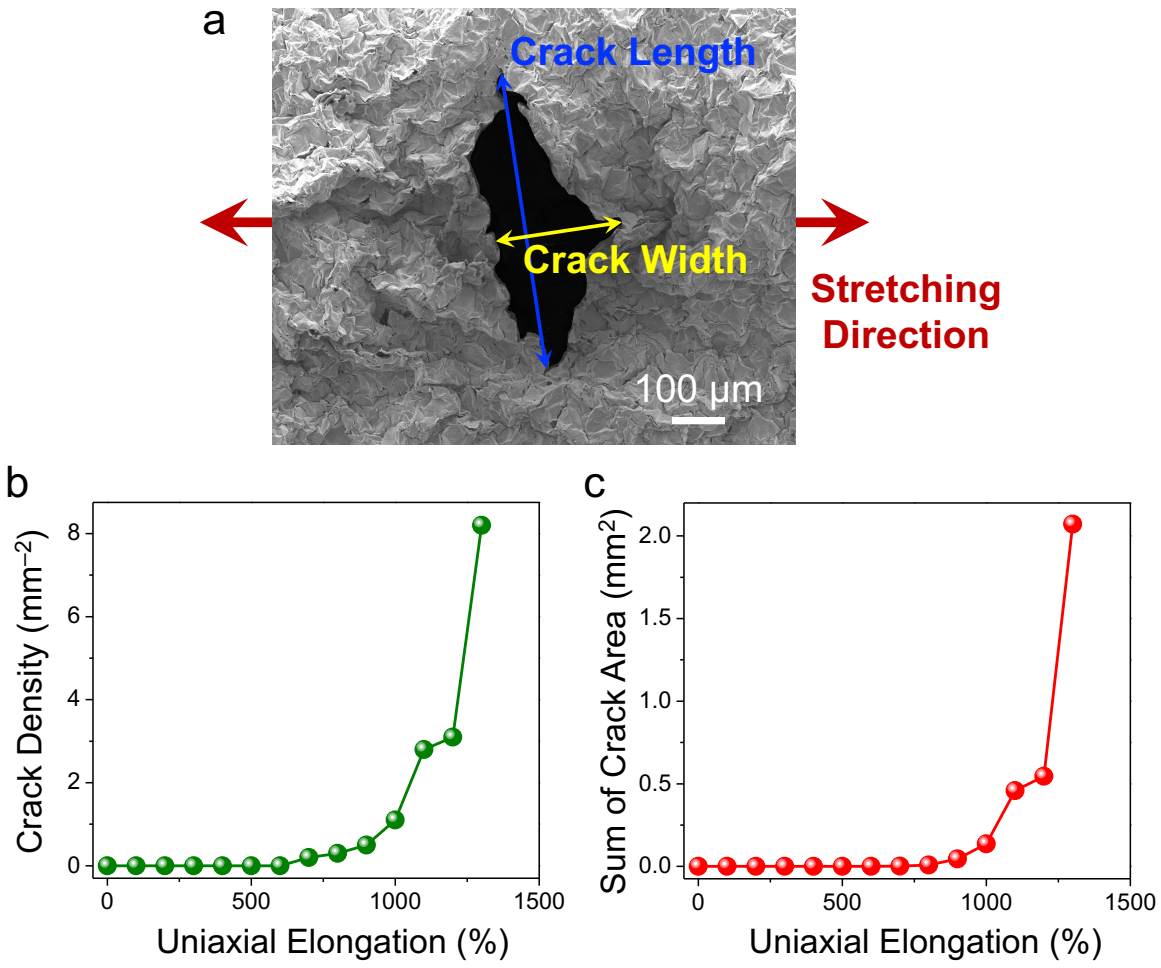

Fig. S20. Crack density and area measurement of a G_2–2D2D stretchable gold conductor. (**a**) The SEM image of a G_2–2D2D stretchable gold conductor under 800% elongation. Crack length (L_1) is defined as the distance between the two furthest points along the perimeter of the crack. Crack width (L_2) is defined as the furthest distance of the crack perpendicular to L_1. (**b**) Crack densities under different elongations. (**c**) Sum of crack areas under different elongations.

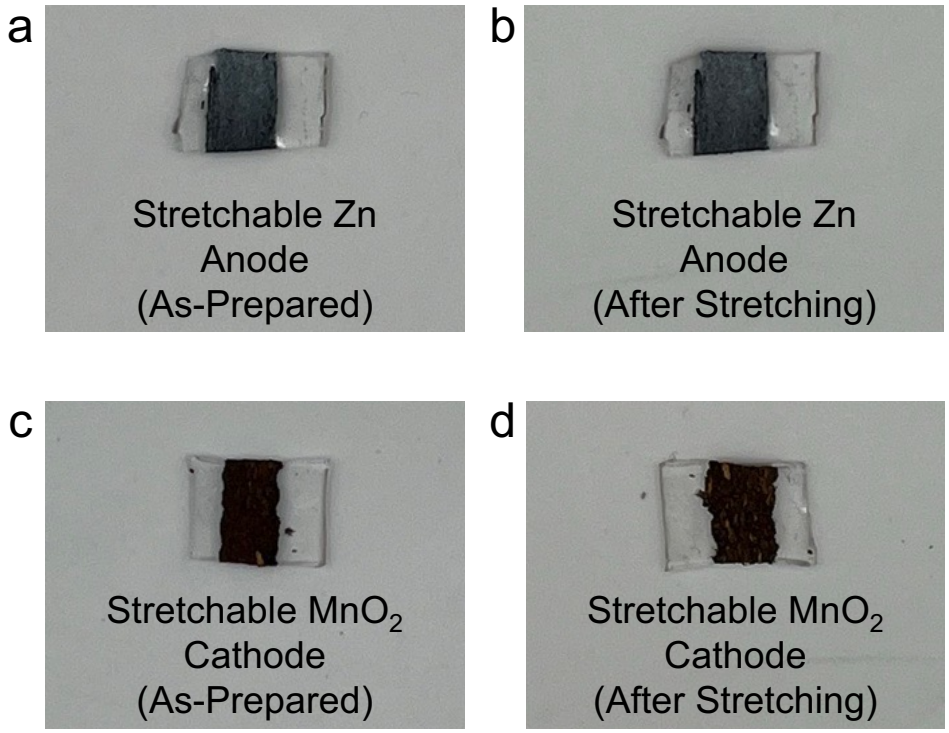

Fig. S21. Photographs of stretchable Zn and MnO_2 electrodes. (**a**) As-prepared stretchable Zn anode. (**b**) Stretchable Zn anode after 3,000 stretching–relaxation cycles. (**c**) As-prepared MnO_2 cathode. (**d**) Stretchable MnO_2 cathode after 3,000 stretching–relaxation cycles.

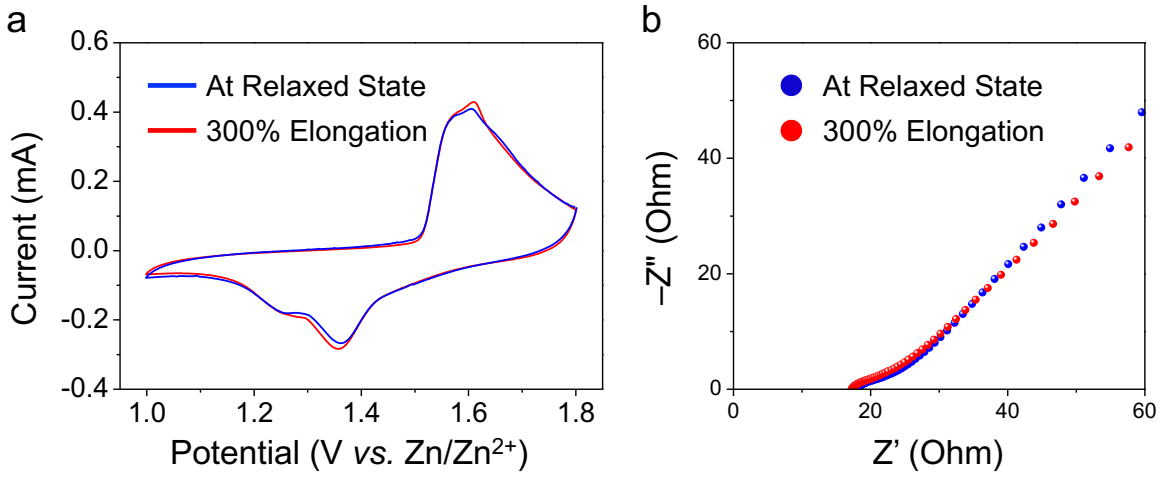

Fig. S22. Electrochemical characterizations of a stretchable Zn//MnO_2 battery at its relaxed state and under 300% elongation. (**a**) CV curves at 1 mV s^{-1}. (**b**) Nyquist plots.

Note S1. Rationale of building block selection and model expansion strategy for G_1/G_2 stretchable nanocomposites.

In this work, four building blocks were selected to fabricate G_1/G_2 stretchable nanocomposites with high electrical conductance and insensitive strain responses. Four building blocks include three electrically conductive nanomaterials, including $Ti_3C_2T_x$ MXene nanosheets, SWNTs, and AuNPs, and polyvinyl alcohol (PVA). First, $Ti_3C_2T_x$ MXene nanosheets, an emerging class of two-dimensional (2D) transition metal carbides, present superior electrical conductivity, intrinsic hydrophilicity, and high aspect ratios[1]. Second, SWNTs, a class of one-dimensional (1D) materials made of a single rolled graphene sheet with a cylindrical nanostructure, demonstrate high tensile strength and superior electrical conductivity[2]. Third, AuNPs, a class of zero-dimensional (0D) materials with an average diameter of 20 nm, can be integrated with the 2D/1D building blocks, which facilitate nanoscale contacts and boost overall electrical conductivity[3]. Last, PVA, as a polymeric binder, is introduced to enhance the structural stability of G_1/G_2 stretchable nanocomposites.

To augment the model's predictive power, we can adopt a model expansion method to incorporate more building blocks into G_1/G_2 stretchable nanocomposites. As shown in **Fig. S1**, additional active learning loops can be performed under the guidance of the prediction model. During the model expansion phase, additional experiments are required to refine the SVM classifier and to update the ANN-based model. By strategically selecting new components in tandem with the model expansion method, the prediction model can consistently enlarge its parameter space and broaden the range of achievable functions. However, this model expansion incurs additional active learning cycles, leading to higher time and cost implications.

Note S2. Tunable wavelengths of G_2–2D1D and G_2–2D2D stretchable nanocomposites.

As shown in **Fig. S4a–c**, the average wavelengths of G_2–2D1D stretchable nanocomposites were tuned from 90 to 48 μm by adjusting the applied pre-strains of VHB substrates from 100% to 300%, respectively. As shown in **Fig. S4d–f**, the average wavelengths of G_2–2D2D stretchable nanocomposites were tuned from 162 to 67 μm, by adjusting the applied pre-strains of VHB substrates from 100% to 300%, respectively.

Note S3. Estimated number of experiments required to build an extensive dataset for G_1/G_2 stretchable nanocomposites.

Three degrees of freedom (DOFs) were recognized in the compositions of G_0 nanocomposites, including MXene loading, SWNT loading, and AuNP loading. Once these three loadings were fixed, the PVA loading was automatically determined. If we set 2.0 wt.% as the step size, the total steps to vary the MXene/SWNT/AuNP/PVA ratio were calculated to be ~23,500. Additionally, the nanocomposites thicknesses, deformation sequences, and applied pre-strain were three other DOFs for the fabrication of G_1/G_2 stretchable nanocomposites. In this work, three thicknesses of G_0 nanocomposites were adopted, including 800 nm, 1,200 nm, and 1,600 nm, and four kinds of deformation sequences were included, containing G_1–1D, G_1–2D, G_2–2D1D, and G_2–2D2D. There were three choices of applied pre-strains during the fabrication of G_2–2D1D and G_2–2D2D stretchable nanocomposites, including 100%, 200%, and 300%. In total, building an extensive dataset for G_1/G_2 stretchable nanocomposites will require ~562,000 experiments if we follow conventional one-factor-at-a-time (OFAT) design of experiment method. For each G_1 or G_2 stretchable nanocomposite, one "electrical" label (S_0) and three "response" labels ($\varepsilon_{5\%}$, $\varepsilon_{7.5\%}$, $\varepsilon_{10\%}$) were needed to be collected. The calculation was conducted using a customized Python program:

https://github.com/yhcbloom14/stretchable_conductor/blob/main/number_of_experiments_for_design_of_experiment.ipynb.

Note S4. Necessity of multistage ML framework.

To demonstrate the necessity of each unit used in the multistage ML framework, justifications are provided as follows to explain why they are superior to other standard methods.

SVM regression model. The SVM regression model served as a critical screening layer in the active learning loops, which drove the prediction model to only recommend the MXene/SWNT/AuNP/PVA ratios that led to the G_0 nanocomposites with high electrical conductance values >6.67 mS. Unlike other data-rich systems with higher tolerance of experiment failure, it would take much time and effort to redo the fabrication of G_0 nanocomposites, if the prediction model suggests the MXene/SWNT/AuNP/PVA ratios that lead to the G_0 nanocomposites with low electrical conductance.

Active learning loops with ensemble modeling. According to **Fig. 3c**, the prediction model (consisting of an ensemble committee with multiple ANNs) demonstrated a low MRE of 13.5% after 7 active learning loops, which accurately predicted the "electrical" and "response" labels of G_1/G_2 stretchable nanocomposites from their fabrication parameters. In comparison, the prediction models based on other algorithms presented higher MREs and were not able to accurately predict the "electrical" and "response" labels, clearly demonstrating the necessity of ANN-based ensemble modeling for such a non-linear and multi-DOF system.

Data augmentation. Data augmentation was conducted to address the major challenges of data scarcity and model overfitting. In this work, the User Input Principle (UIP) method was adopted to synthesize virtual data points, and both real and virtual data points were input to train a prediction model. As shown in **Fig. 3d**, after the UIP method, the model's prediction accuracy was largely improved, and the MREs decreased from 30.6% to 13.5%.

Overall, we believe that the multistage ML framework composed of SVM regression model, active learning loops with ensemble modeling, and data augmentation can synergistically improve the accuracy of a prediction model. In contrast, a simple or single ML tool/method could not achieve such model accuracy based on a small dataset.

Note S5. Training of a support vector machine (SVM) regression model.

To ensure the prediction model to suggest the MXene/SWNT/AuNP/PVA ratio that resulted in the fabrication of a G_0 nanocomposite with high electrical conductance (>6.67 mS), a SVM regression model was constructed. The SVM regression model predicted the electrical conductance of a G_0 nanocomposite from its MXene/SWNT/AuNP/PVA ratio.

To construct a SVM regression model, four steps were involved: (*1*) take the logarithmic term of the electrical conductance, (*2*) select a kernel function, (*3*) optimize SVM hyperparameters, and (*4*) train a SVM model using the training data points. For the first step, as the electrical conductance values ranged widely from 0 to +∞, which was ineffective in training an accurate SVM regression model. Therefore, we calculated the logarithmic conductance value using **Equation S1**,

$$\text{Logarithmic conductance (LC)} = {}^{1}\!/_{\log_{10}(S_0^{-1} + 10)} \quad \text{(S1)}$$

, where S_0 is the electrical conductance of a G_0 nanocomposite, and the LC values range from 0 to +1. For the second step, as the LC values were shown to be non-linear, we decided to select a radial basis function (RBF) as the kernel function to map low-dimension data points into a higher dimensional feature space to find the optimal hyperplanes with maximal margin distances[4]. For the third step, Bayesian optimization (involving Gaussian processes and a 5-fold cross validation) was used to adjust the hyperparameter values[5]. For the fourth step, the SVM regression model was trained by inputting 286 data points (**Table S2**). Finally, the SVM regression model demonstrated a low mean relative error (MRE) of ~17% to predict the LC values of G_0 nanocomposites using 42 testing data points (which were never input into the model training phase, **Table S4**). After setting the electrical conductance threshold of >6.67 mS, a feasible parameter space was defined

in **Fig. S7**. The SVM regression model was able to suggest the MXene/SWNT/AuNP/PVA ratios that were positioned in the feasible parameter space at high accuracy of 95%.

The open-source code to train the SVM regression model in Python is provided in GitHub: https://github.com/yhcbloom14/stretchable_conductor/blob/main/design_boundary.ipynb.

Note S6. User Input Principle (UIP) method for data augmentation.

To address model overfitting challenges upon the use of a small dataset, the data points collected during active learning were augmented using the UIP method. The UIP method is based on the natural principles proposed by expert users. For example, over small variations across specific "composition" label(s), the "electrical" and "response" labels of a stretchable nanocomposite remained approximately the same. As shown in **Fig. S9**, when the MXene/SWNT/AuNP/PVA ratios varied from 22.0/65.2/7.8/5.0 to 21.6/69.7/5.5/3.2, the resulting G_1–2D stretchable nanocomposites exhibited similar "electrical" and "response" labels. Also, measurement variations existed in the "electrical" and "response" labels. As shown in **Fig. S10**, by following the same set of fabrication parameters, the characterized the "electrical" and "response" labels had 10–20% measurement variations among multiple replicates. In this work, based on 146 data points collected during active learning, we used the UIP method to synthesize 1,000-fold virtual data points by introducing Gaussian noises into all "composition", "electrical", and "response" labels.

The open-source code to implement the UIP method in Python is provided in GitHub: https://github.com/yhcbloom14/stretchable_conductor/blob/main/data_augmentation.ipynb.

Note S7. Calculation of *A Score* acquisition function.

In the active learning loops, an acquisition function was introduced to suggest the targeted data points with the highest uncertainty in the feasible parameter space. We defined the acquisition function as *A Score* (**Equation S2**),

$$A\ Score = min(\hat{L}_1, \hat{L}_2) \cdot \hat{\sigma} \tag{S2}$$

, where $\hat{L}_1$ denotes the shortest Euclidian distance between current input labels (within the dataset of prediction model) and targeted input labels (not yet included in the dataset of prediction model), and $\hat{L}_2$ denotes the shortest Euclidian distance between each targeted input label. Input labels include MXene loading, SWNT loading, AuNP loading, PVA loading, nanocomposite thickness, deformation sequence, and applied pre-strain. $\hat{L}_1$ and $\hat{L}_2$ are calculated by **Equation S3,4,** respectively,

$$\hat{L}_1 = \min_{\substack{i \in N \\ j \in M}} \left(||Input_i - Input_j|| \right) \tag{S3}$$

$$\hat{L}_2 = \min_{\substack{j \in M \\ k \in M}} \left(||Input_j - Input_{k \neq j}|| \right) \tag{S4}$$

, where N is the cumulative number of data points in the current dataset, and M is the cumulative number of data points in the targeted dataset. One-hot encoding was used for the input label of deformation sequence in the prediction model. On the other hand, $\hat{\sigma}$ denotes the prediction variance of "electrical" and "response" labels from the ensemble committee of ANNs, which is defined in **Equation S5**,

$$\hat{\sigma} = \sum_{i=1}^{M} \sum_{p=1}^{C} \left[(Output_{p,i}) - (Output_{average,i}) \right]^2 \tag{S5}$$

, where M is the cumulative number of data points in the target dataset, C is the total number of ANNs in the ensemble committee (C = 5), $Output_{p,i}$ is the output labels predicted by the p^{th}

decision program on basis of the input labels of a targeted data point, $Output_{average,i}$ is the average output labels predicted by the ANN committee on basis of the input labels of a targeted data point.

The open-source code to implement *A Score*-based active learning loops in Python is provided in GitHub:

https://github.com/yhcbloom14/stretchable_conductor/blob/main/active_learning.ipynb.

Note S8. SHAP model interpretation.

The SHAP model interpretation is a game theoretic approach to explain the output of any ML model (including any ensemble models). The SHAP model interpretation can find the feature importance inside a ML model, enabling the users to address the black-box challenges of AI/ML predictions. The analytical process of SHAP model interpretation is like investigating the contribution of each player in a collaborative game. To understand how the feature importance is derived in the SHAP analysis, an example is presented below.

As shown in **Fig. S15a**, there are three players, *A*, *B*, and *C*. They collaborate with each other to play a game. When all of them join the game, based on their different skills in a specific game, they can collectively achieve a 100 reward. The task is to quantify how important each player is in getting the reward. To solve this, we assume that three players join the game in a specific sequence (e.g., player *A* first, then player *B*, next player *C*), and the marginal reward of each player is then recorded. For example, player *A* is the first member with a reward of 50, then player *B* joins the game and brings the reward to 90, and next player *C* joins the game to bring the reward to 100. Therefore, the players' respective marginal rewards are "players *A*, *B*, *C* = 50, 40, 10". However, the calculated marginal reward may not accurately represent the contribution of each player. For example, when the sequence is changed from players *A*, *B*, *C* to players *A*, *C*, *B*, the rewards are still 50, 40, and 10, indicating that players *B* and *C* have a similar skill set. Then, the players' respective marginal rewards are changed to "player *A, B*, *C* = 50, 10, 40". Therefore, the sequence of how the players join the game is important.

To get a more accurate reward of each individual player, we need to find out the marginal reward of each player under every possible sequence. The reward for each individual player then can be the sum of these marginal rewards over the number of possible sequences (the calculation

for a specific player is illustrated in **Equation S6**). For example, in the case outlined above, we can simulate the arrival sequences: *ABC*, *ACB*, *BCA*, *BAC*, *CAB*, and *CBA*, and the marginal reward of each player is recorded for each sequence. Then, by averaging all these rewards, we obtain the reward contributed from each player. This reward is the SHAP value,

$$SHAP\ value\ of\ a\ specific\ player = \frac{\sum_N marginal\ reward\ of\ the\ player}{N} \quad \text{(S6)}$$

, where *N* represents number of total possible sequences.

In contrast to the feature importance analysis of a prediction model, we can take the problem as an analogy to the above case. All "composition" (MXene loading, SWNT loading, AuNP loading, and PVA loading), "thickness", "deformation", and "strain" labels are regarded as players, which are fed into the prediction model to obtain the "conductance" and "response" labels. The prediction process is treated as the game, and the deviation (between the predicted "electrical" and "response" label of a specific data point and the average "electrical" and "response" labels from all data points) is treated as the reward. By following **Equation S7**, the SHAP value of each input label on a specific "electrical" or "response" label can be calculated, and this value is used to measure the feature importance.

$$SHAP\ value\ of\ an\ input\ label = \frac{\sum_N marginal\ reward\ of\ an\ input\ label\ on\ a\ specific\ output\ label}{N} \quad \text{(S7)}$$

, where *N* represents number of total possible sequences. The above process is the interpretation of the prediction model on a specific data point which is called the local interpretation. To get the global interpretation of the prediction model over all data points, we can plot the SHAP values of every input label for every data point, as shown in **Fig. S15b**. A wider range of the SHAP value for a specific feature indicates a higher importance, and *vice versa*.

The open-source code to implement SHAP analyses in Python is provided in GitHub: https://github.com/yhcbloom14/stretchable_conductor/blob/main/shap_plotting.ipynb.

Note S9. Two-scale finite element (FE) models of G_1/G_2 stretchable nanocomposites.

The complex topographies of G_1/G_2 stretchable nanocomposites were first generated using different deflection functions. These deflection functions were determined by minimizing the total energy of the binary system (including a conductive nanocomposite and an elastomeric substrate) under varying compressive stresses, as formulated in **Equation S8**[6],

$$\xi_t(\{u,v,w\}) = \xi_s(\{w\}) + \xi_{fb}(\{w\}) + \xi_{fs}(\{u,v,w\}) \quad \text{(S8)}$$

, where $\xi_t(\{u,v,w\})$ represents the total energy of a binary nanocomposite–substrate system, $\xi_s(\{w\})$ is the energy of an elastomeric substrate, $\xi_{fb}(\{w\})$ and $\xi_{fs}(\{u,v,w\})$ are the energy of a conductive nanocomposite at the stretching and bending states, respectively. The total energy of a binary nanocomposite–substrate system, $\xi_t(\{u,v,w\})$, is a function of the in-plane displacements, $u(x,y)$ and $v(x,y)$ as well as the out-of-plane displacements, $w(x,y)$.

Audoly and Boudaoud has derived a general deflection function that can capture the four types of buckling modes[6], including the cylindrical, undulating, varicose, and checkerboard modes, as described in **Equation S9**,

$$w(x,y) = Acos(kx) + Bsin(kx)\sin(k'y) + Ccos(kx)\cos(k'y) + D\cos(k'y) \quad \text{(S9)}$$

, where k is the wavenumber in the x direction (horizontal, in plane), k' is the wavenumber in the y direction (perpendicular to the x direction), A, B, C, D are the correlation parameters that tuned the amplitude(s) of a specific buckling mode. The relation between k and the wavelength (λ) was correlated by **Equation S10**,

$$k = 2\pi/\lambda \quad \text{(S10)}$$

, where λ is the wavelength of a G_1 or G_2 stretchable nanocomposite characterized from a Keyence laser confocal microscope. In this work, k' was assumed to be 1/10. **Table S8** summarizes the

correlation parameters selected to construct the FE models of G_1–1D, G_1–2D, G_2–2D1D, G_2–2D2D stretchable nanocomposites.

FE model of G_1–1D stretchable nanocomposites. As shown in **Fig. S18a**, the post-buckled topography of a G_1–1D stretchable nanocomposite was described as a cylindrical mode with a sinusoidal cross-section in an equilibrium state when subjected to uniaxial compression. To describe the wrinkle-like microtextures, a deflection function was derived in **Equation S11**,

$$w(x,y) = Acos(kx) \tag{S11}$$

FE model of G_1–2D stretchable nanocomposites. As shown in **Fig. S18b**, the post-buckled topography of a G_1–2D stretchable nanocomposite was described as a checkerboard mode in an equilibrium state when subjected to biaxial compression[7,8]. To describe the crumple-like microtextures, a deflection function was derived in **Equation S12**,

$$w(x,y) = Acos(kx) + D\cos(k'y) \tag{S12}$$

FE models of G_2–2D1D and G_2–2D2D stretchable nanocomposites. As shown in **Fig. S18c,d**, the hierarchical topographies of G_2–2D1D and G_2–2D2D stretchable nanocomposites arising from sequential deformations were described using a two-scale modeling approach. At the smaller scale, the crumple-like topography was described as a checkerboard mode, similar as the FE model of G_1–2D stretchable nanocomposites. At the larger scale, the G_2–2D1D stretchable nanocomposite exhibited straight strips and was simulated as a cylindrical mode with a sinusoidal cross-section, similar as the FE model of G_1–1D stretchable nanocomposites. At the larger scale, the G_2–2D2D

stretchable nanocomposites exhibited S-shaped strips and was simulated as an undulating mode, and a deflection function was derived in **Equation S13**,

$$w(x,y) = Acos(kx) + bsin(kx)\sin(k'y) \quad \text{(S13)}$$

The complex surfaces of G_1–1D, G_1–2D, G_2–2D1D, G_2–2D2D stretchable nanocomposites were simulated, meshed, and exported to the STL files using MATLAB's stlwrite function[9] (https://www.mathworks.com/matlabcentral/fileexchange/20922-stlwrite-write-ascii-or-binary-stl-files). The STL files were then imported into Abaqus 2022/Standard FE solver, and the geometries were reconstructed using a plug-in tool developed by the SIMULIA Benelux office (https://www.mathworks.com/matlabcentral/fileexchange/20922-stlwrite-write-ascii-or-binary-stl-files).

Subsequently, a linear, elastic material model was introduced to all FE models with a Young's modulus of 1 GPa and a Poisson's ratio of 0.227[10]. These FE models aimed to simulate the deformation mechanisms of G_1–1D, G_1–2D, G_2–2D1D, G_2–2D2D stretchable nanocomposites. The modeling accuracy was maintained with 238,287 elements for the G_1–1D stretchable nanocomposites, 244,216 elements for the G_1–2D stretchable nanocomposites, 591,893 elements for the G_2–2D1D stretchable nanocomposites, and 566,176 elements for the G_2–2D2D stretchable nanocomposites, utilizing 4-node linear tetrahedron elements.

Note S10. Clustering analysis.

In this work, we use the DBSCAN algorithm to search the clusters with both high S_0 and $\varepsilon_{10\%}$ values in the feasible parameter space. The acronym stands for "**Density-based Spatial Clustering of Applications with Noise" [11].** The central component to the DBSCAN algorithm is the concept of *"core samples"*, which are the samples in the high-density areas. There are two crucial parameters to the DBSCAN algorithm, (1) *min_samples* and (2) *eps*. Higher *min_samples* or lower *eps* indicate higher density necessary to form a cluster. In this work, we set the *min_samples* and *eps* values to be 70 and 0.05, respectively. The *eps* parameter was chosen appropriately, which was used to control the local neighborhood of the data points. When *eps* was chosen to be too small, most data points would not be clustered at all. When *eps* was chosen to be too large, it caused close clusters to be merged into one cluster, and eventually the entire data set to be returned as a single cluster. It should be noted that, before the model was employed to identify any champion samples through clustering analysis, the MRE value (using an independent testing data points) needed to be sufficiently low. Afterward, a certain amount of experimental validation can be conducted near the model-suggested clusters with global maximum. Through both approaches, one can gain more confidence in the discovery of functional materials with superior properties.

The open source code to implement clustering analyses in Python is provided in GitHub: https://github.com/yhcbloom14/stretchable_conductor/blob/main/clustering_analysis.ipynb.

Note S11. Crack propagation of G_2–2D2D gold conductors.

Quantified by the SEM images of a G_2–2D2D gold conductor during a continuous strain loading process (in **Fig. 5e**), the statistical analyses of crack densities and crack areas are provided in **Fig. S20**. **Fig. S20a** illustrates how crack areas were measured. First, crack density is defined as the total number of cracks over a characterization area of SEM images. As shown in **Fig. S20b,c**, under 600% elongation, the G_2–2D2D stretchable gold conductor showed no obvious cracks. Under 900% elongation, the sums of crack width and length were characterized as 886 and 432 μm, respectively, resulting in the total crack area estimated to be 0.045 mm^2. Meanwhile, the crack density increased to 0.5 mm^{-2}. Once the elongation increased over 1,300%, the sums of crack width and length quickly increased to 16 and 13 mm, respectively, resulting in the total crack area estimated to be 2.072 mm^2, and the crack density increased to 8.2 mm^{-2}.

Table S1. Photos of 286 G_0 nanocomposites with different MXene/SWNT/AuNP/PVA ratios as the training data points for the SVM regression model.

1	2	3	4	5
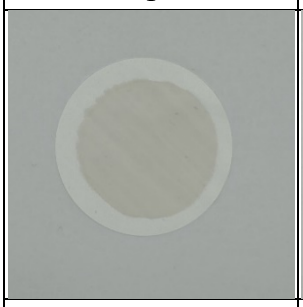	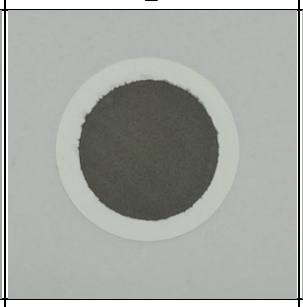	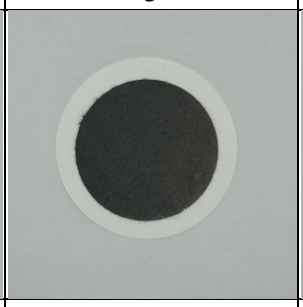	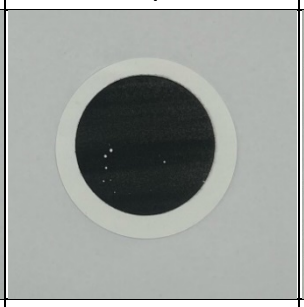	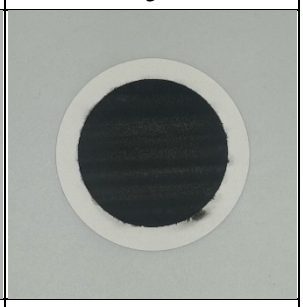
6	7	8	9	10
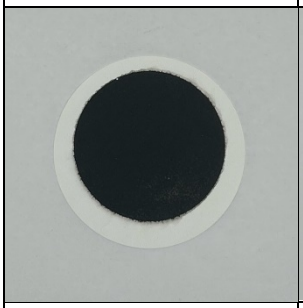	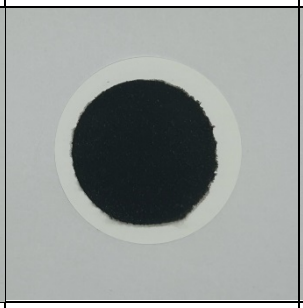	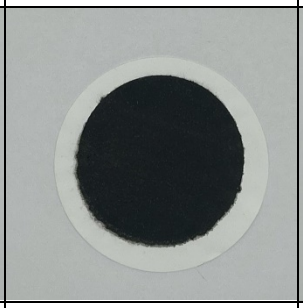		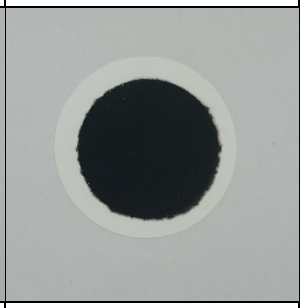
11	12	13	14	15
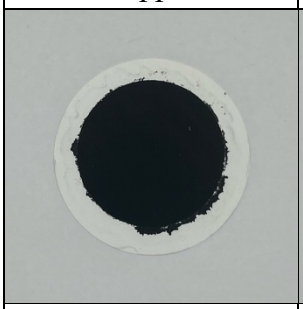	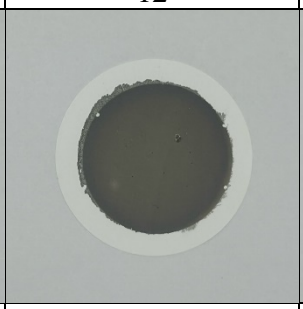	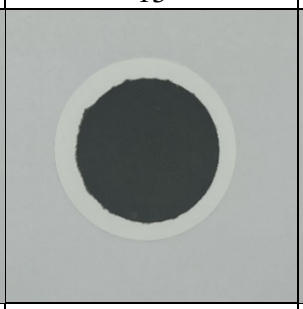	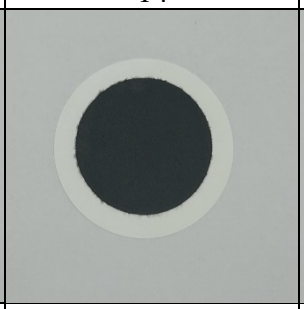	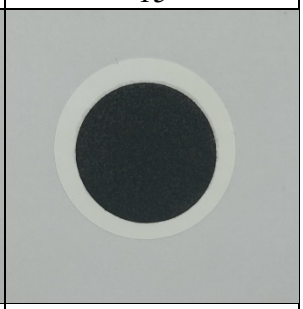
16	17	18	19	20
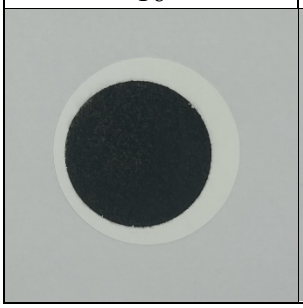	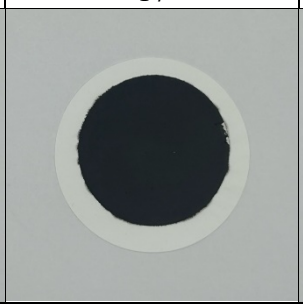	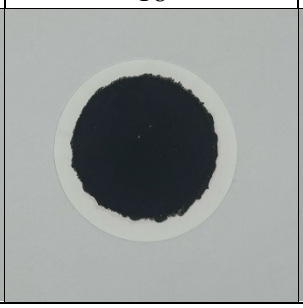	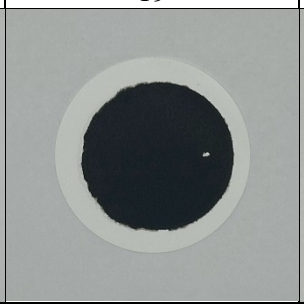	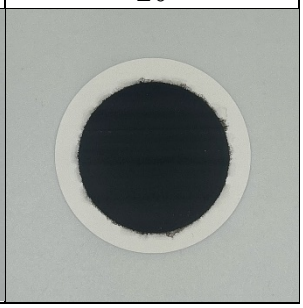

21	22	23	24	25
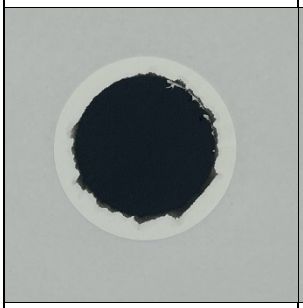	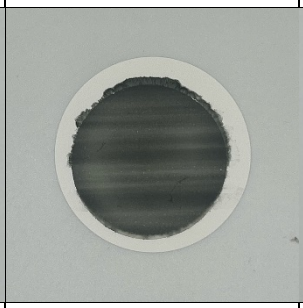	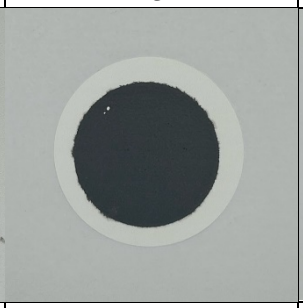	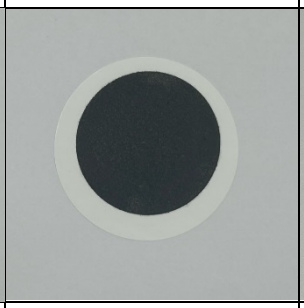	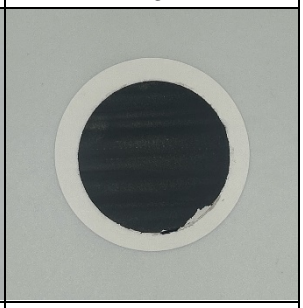
26	27	28	29	30
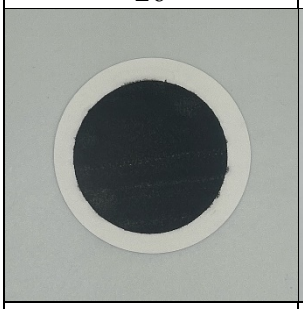	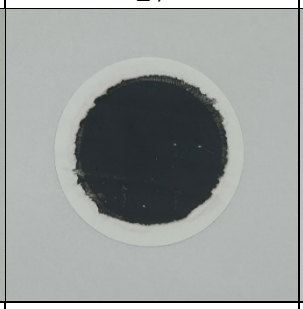	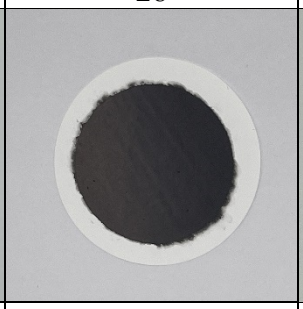	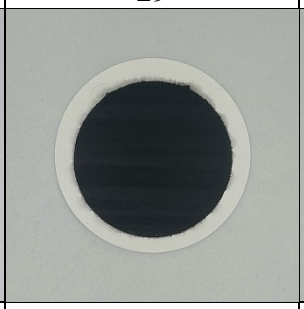	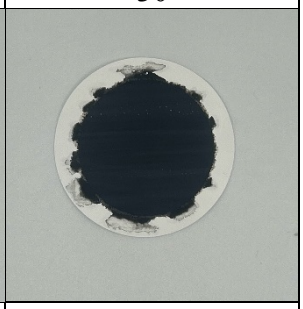
31	32	33	34	35
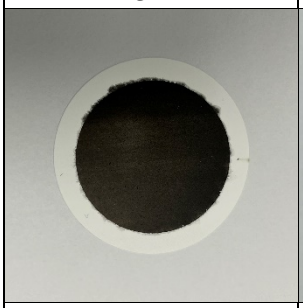	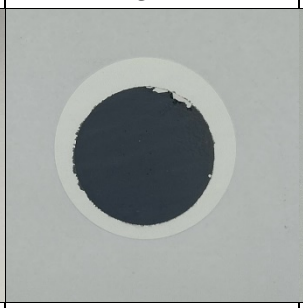	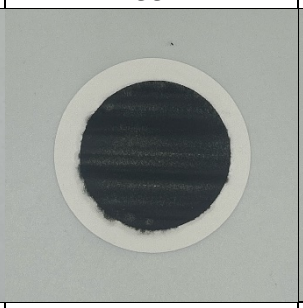	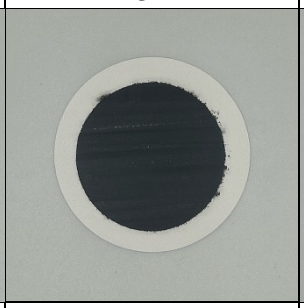	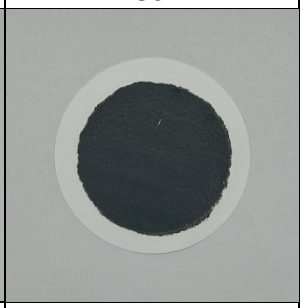
36	37	38	39	40
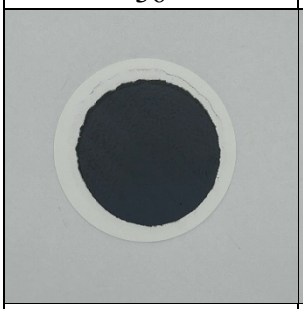	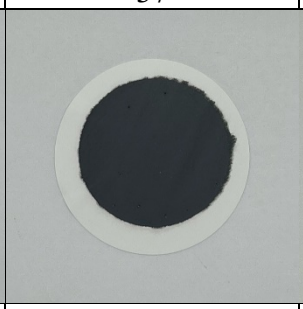	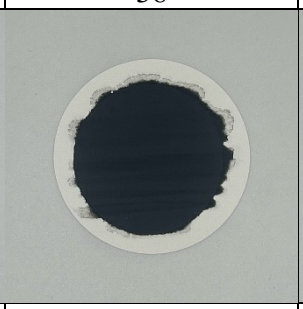	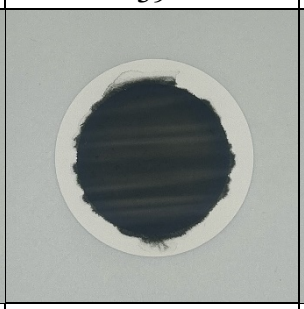	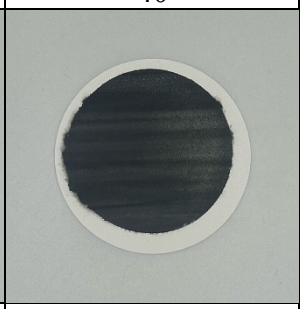
41	42	43	44	45
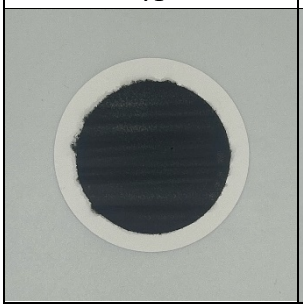	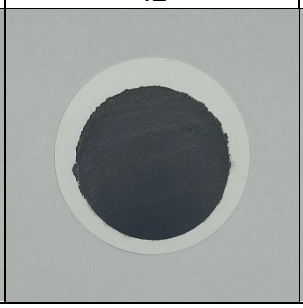	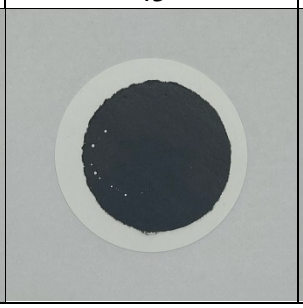	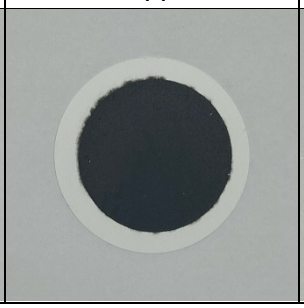	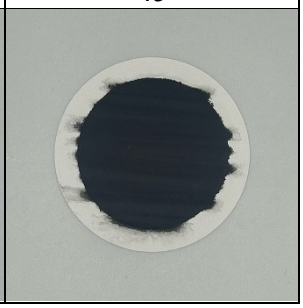

46	47	48	49	50
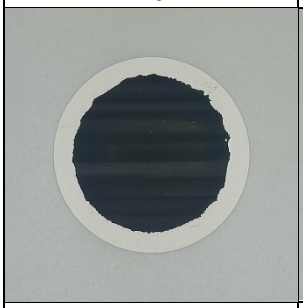	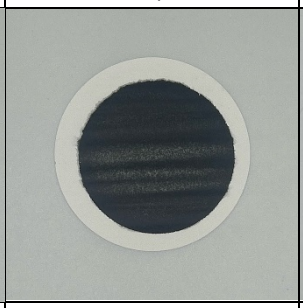	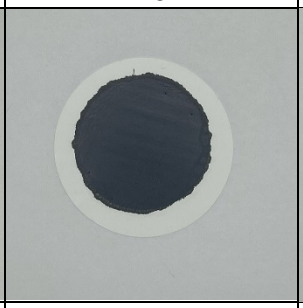	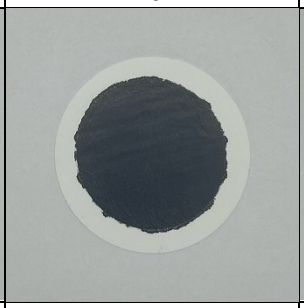	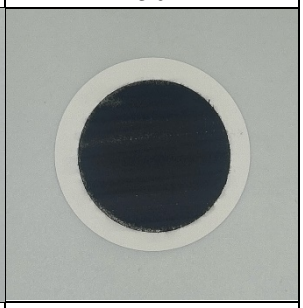
51	52	53	54	55
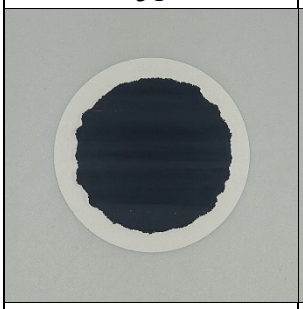	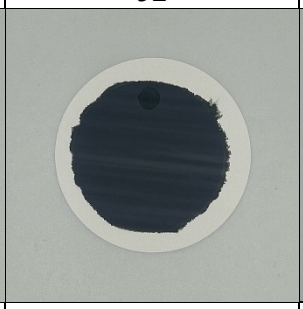	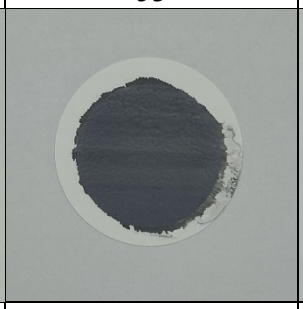	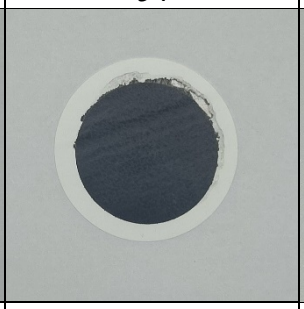	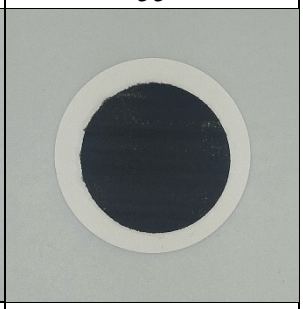
56	57	58	59	60
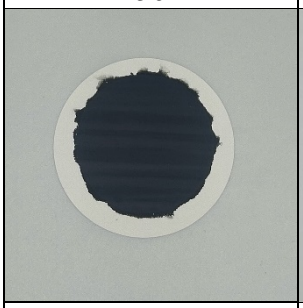	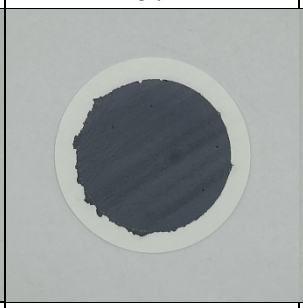	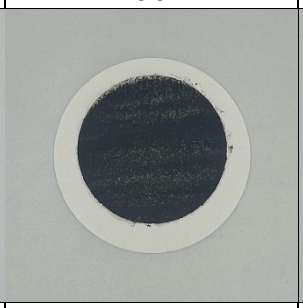	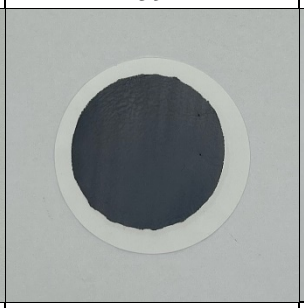	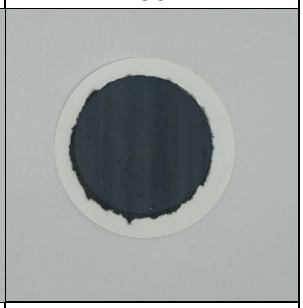
61	62	63	64	65
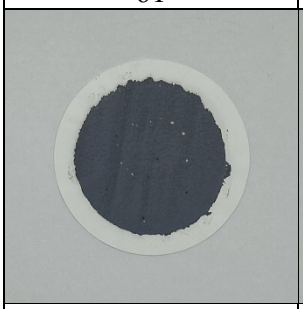	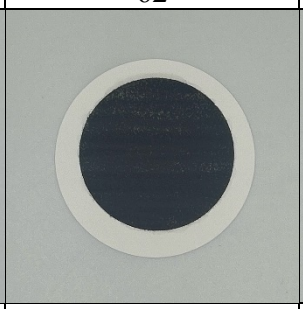	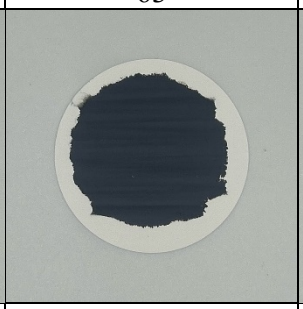	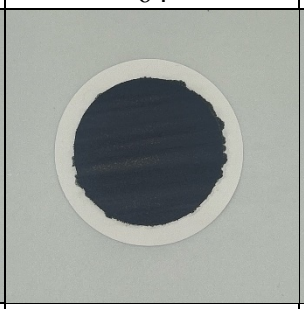	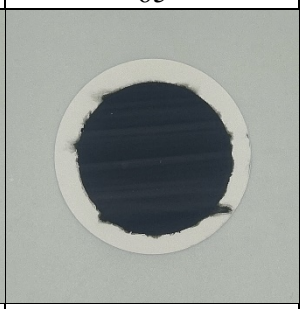
66	67	68	69	70
		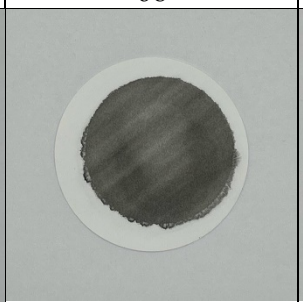	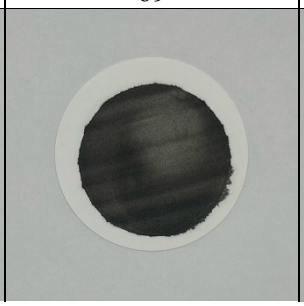	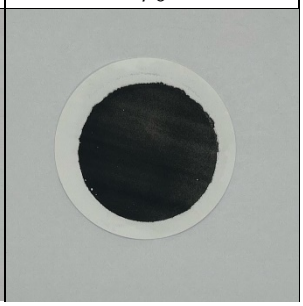

71	72	73	74	75
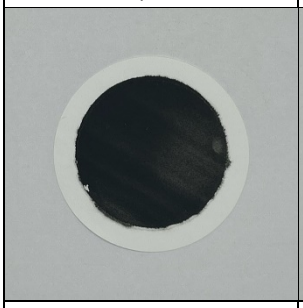	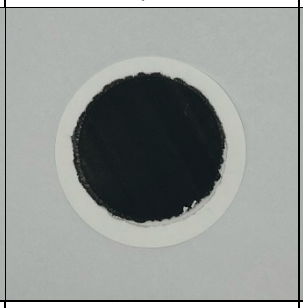	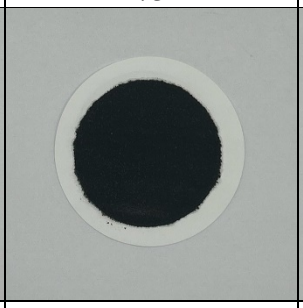	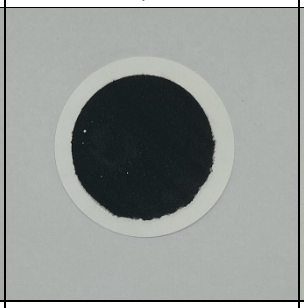	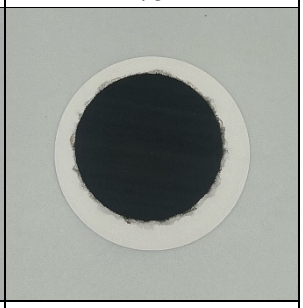
76	77	78	79	80
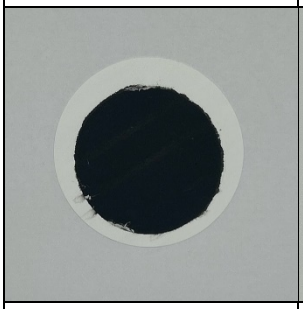	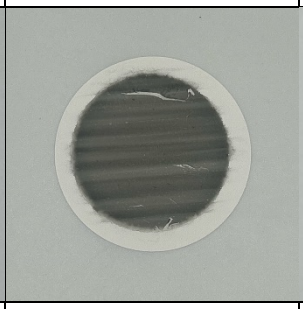	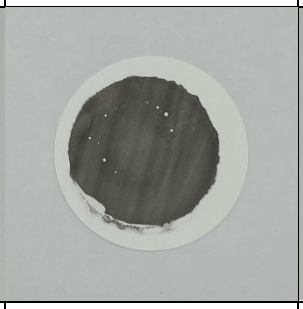	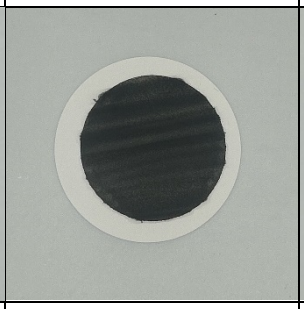	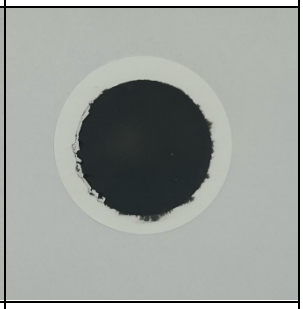
81	82	83	84	85
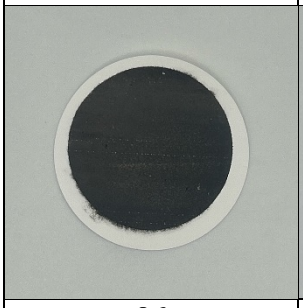	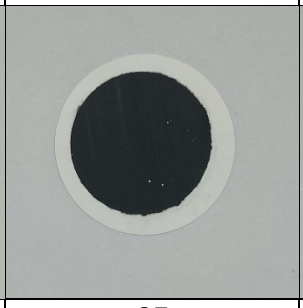	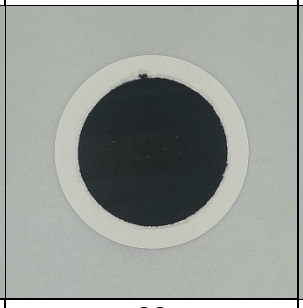	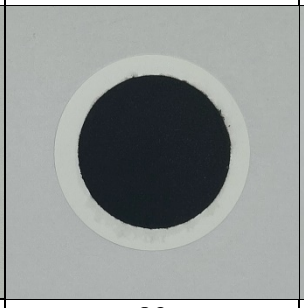	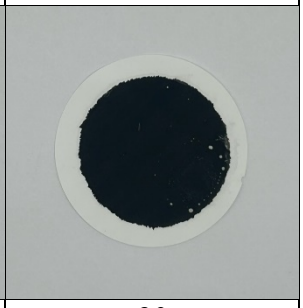
86	87	88	89	90
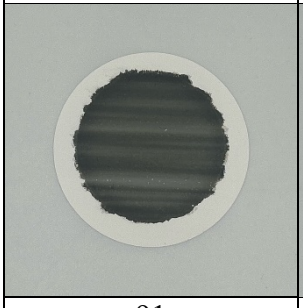	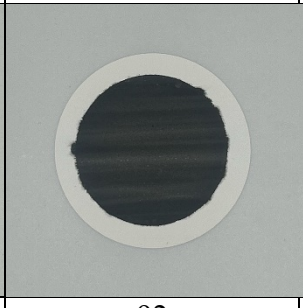	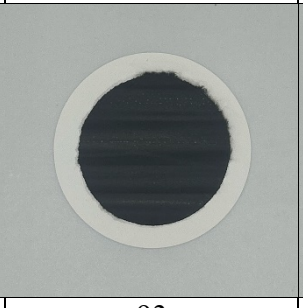	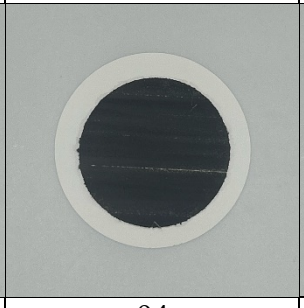	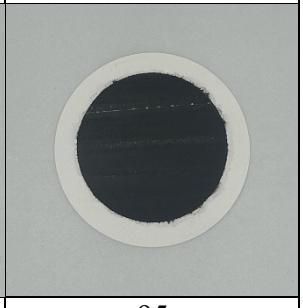
91	92	93	94	95
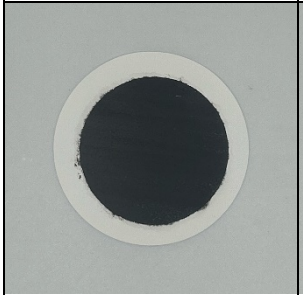	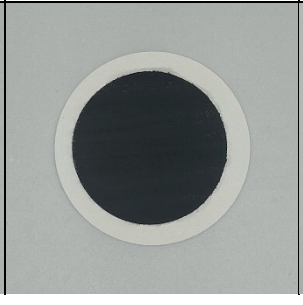	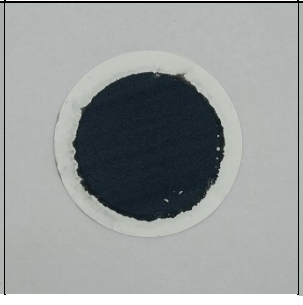		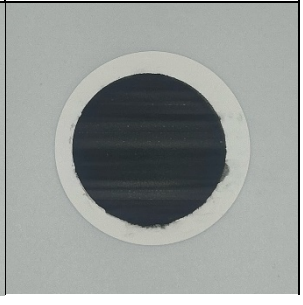

96	97	98	99	100
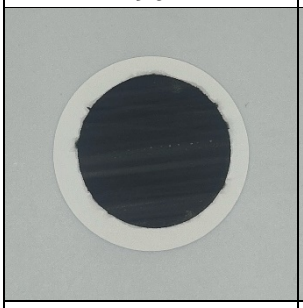	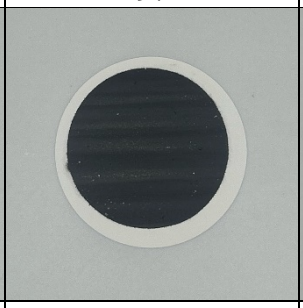		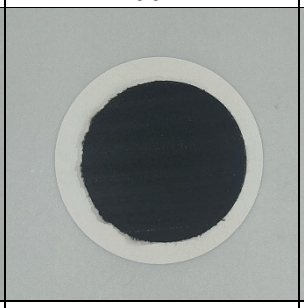	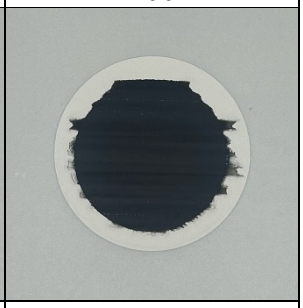
101	102	103	104	105
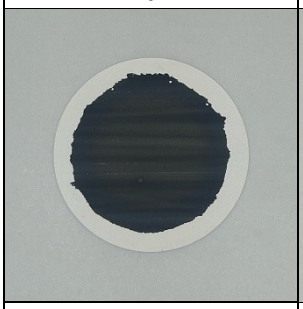	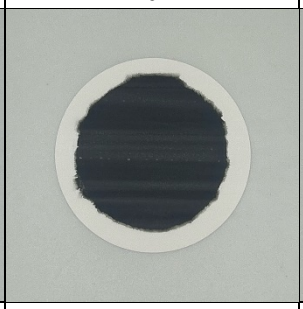	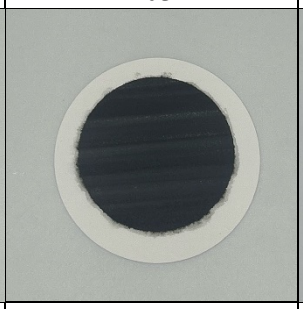	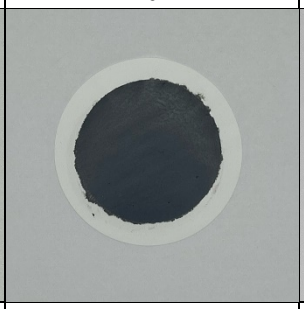	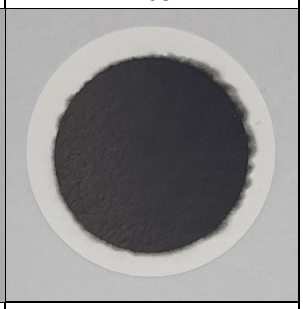
106	107	108	109	110
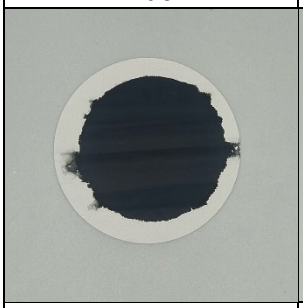	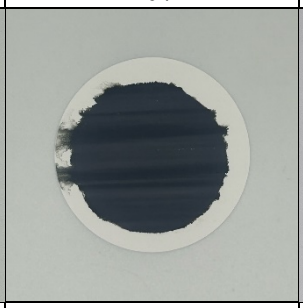	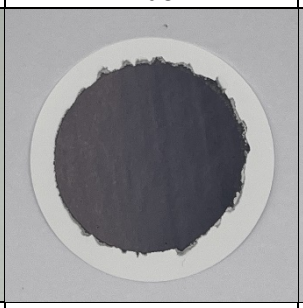	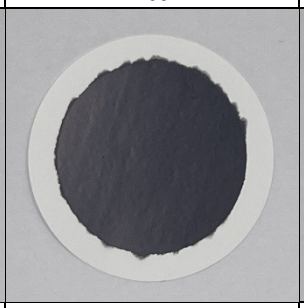	
111	112	113	114	115
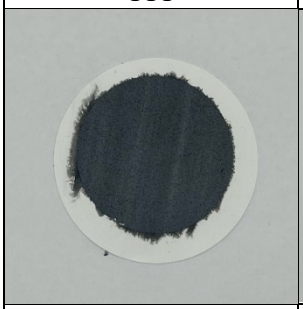	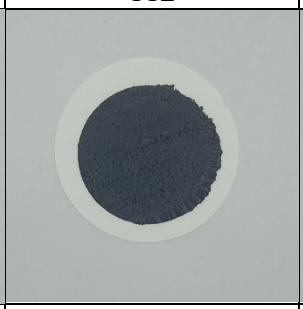			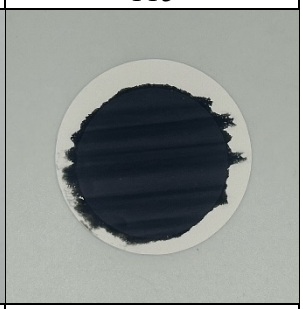
116	117	118	119	120
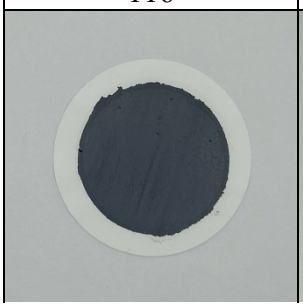	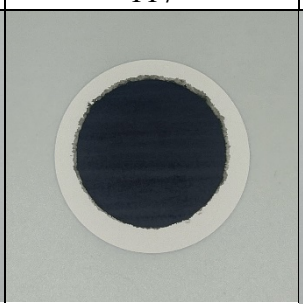	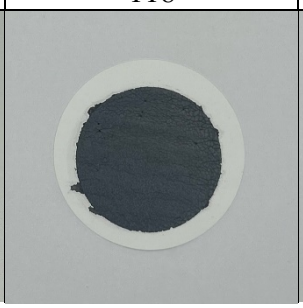	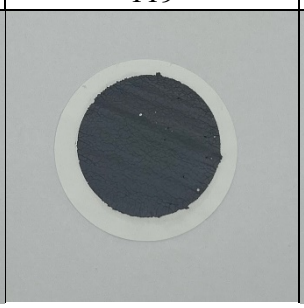	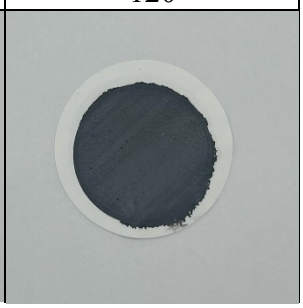

121	122	123	124	125
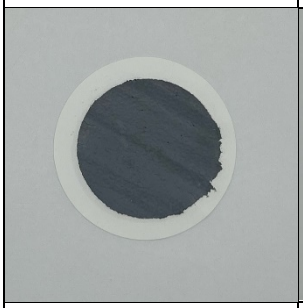	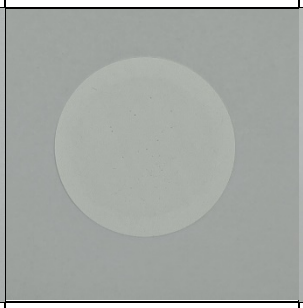	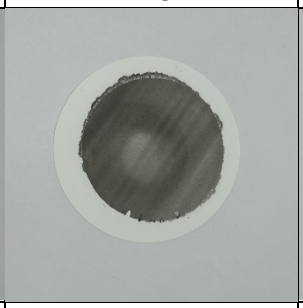	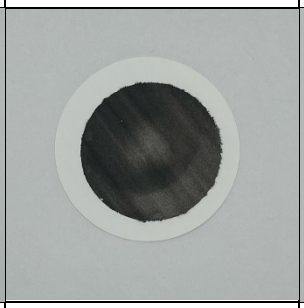	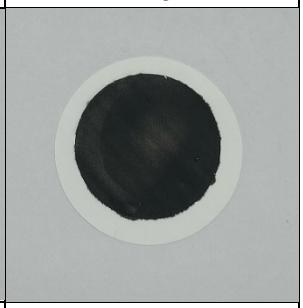
126	127	128	129	130
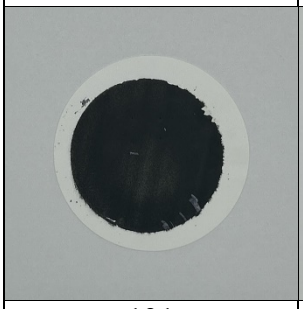	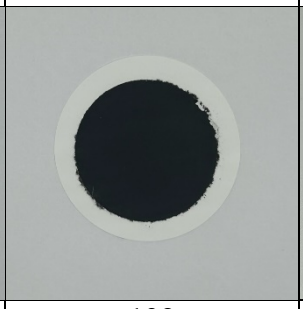	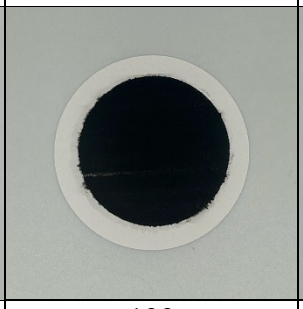	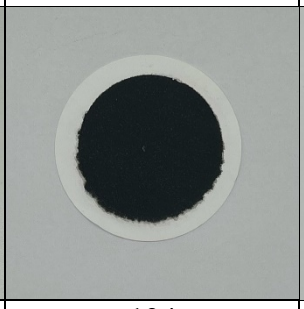	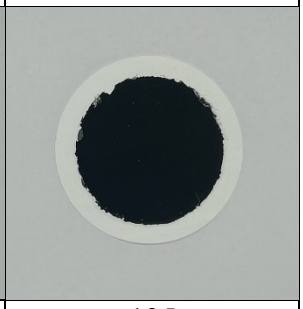
131	132	133	134	135
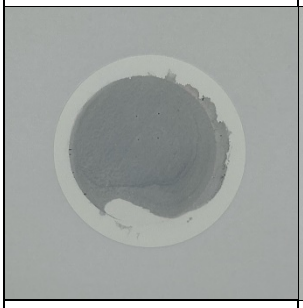	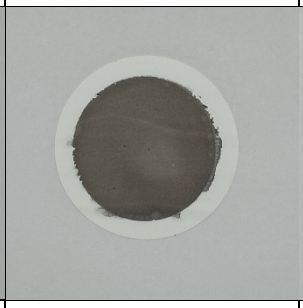	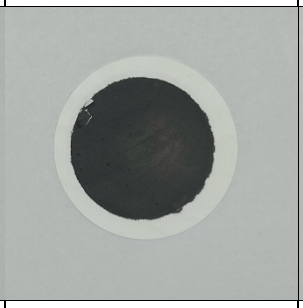	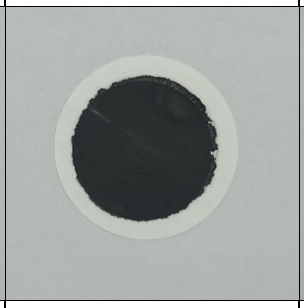	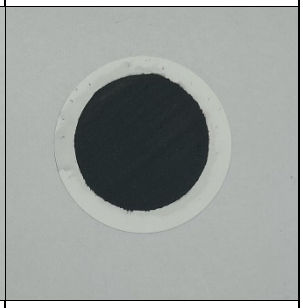
136	137	138	139	140
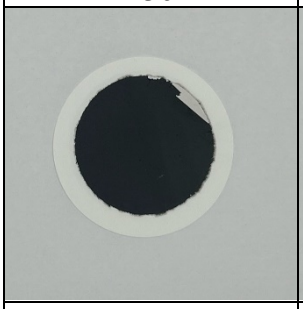		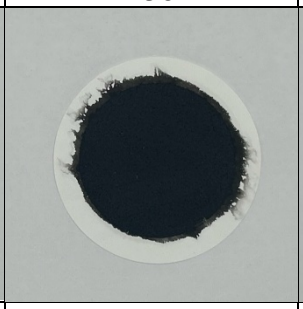	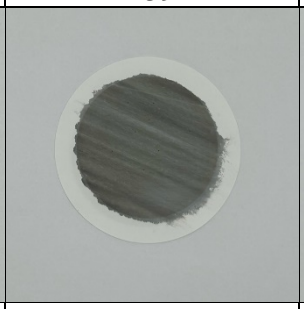	
141	142	143	144	145
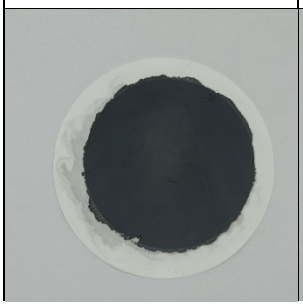	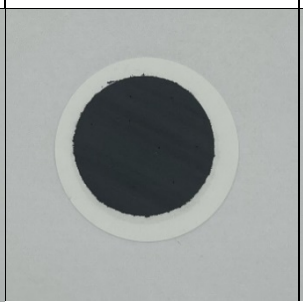	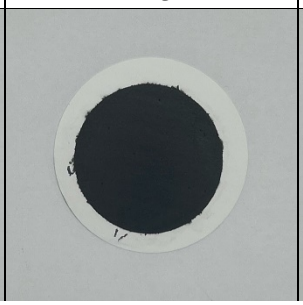	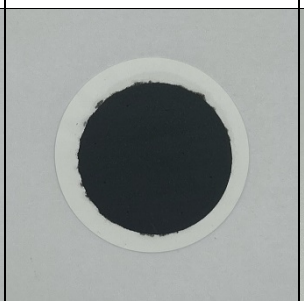	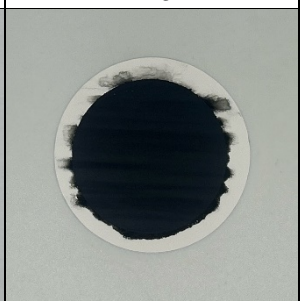

146	147	148	149	150
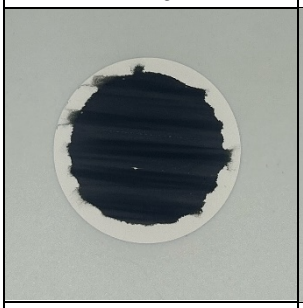	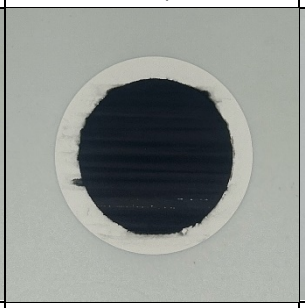	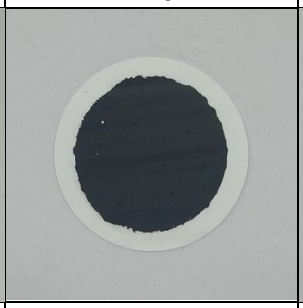	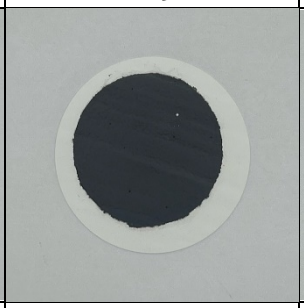	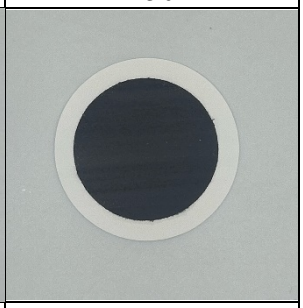
151	152	153	154	155
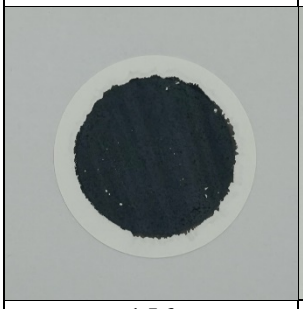			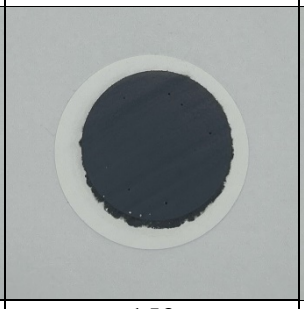	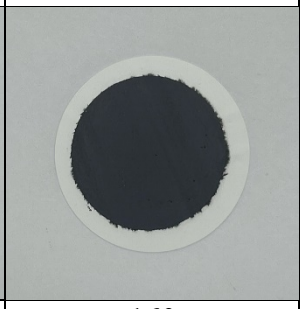
156	157	158	159	160
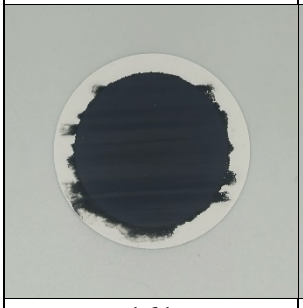	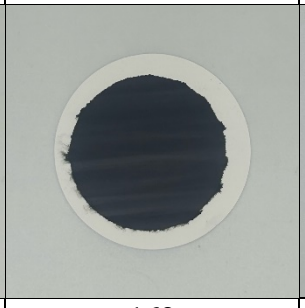	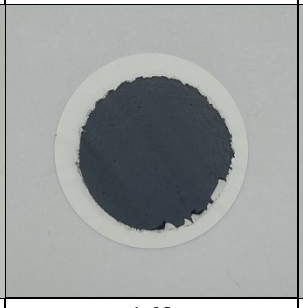	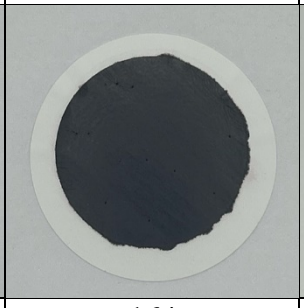	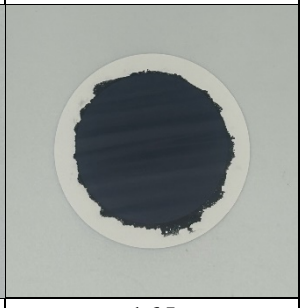
161	162	163	164	165
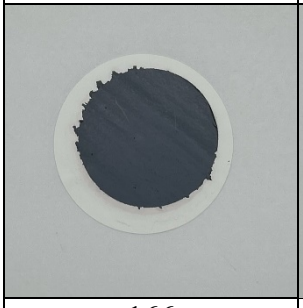	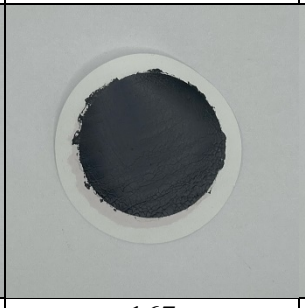	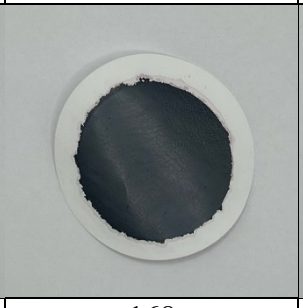	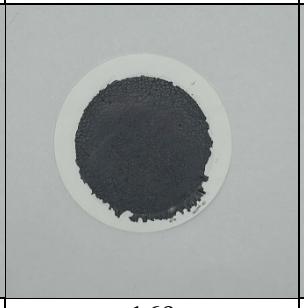	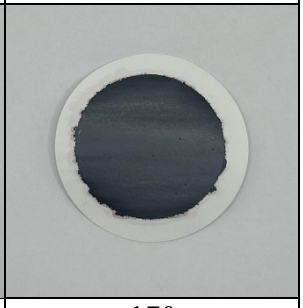
166	167	168	169	170
		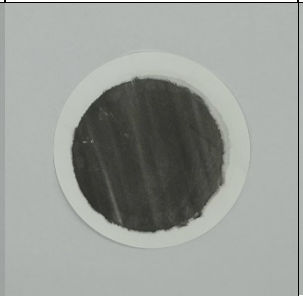	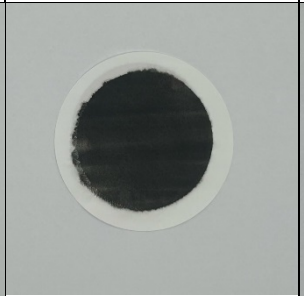	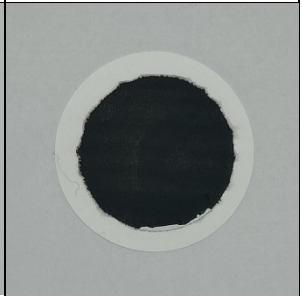

171	172	173	174	175
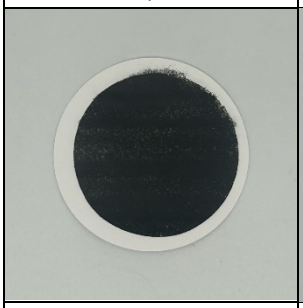	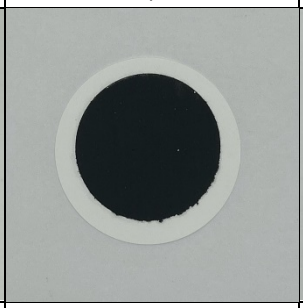	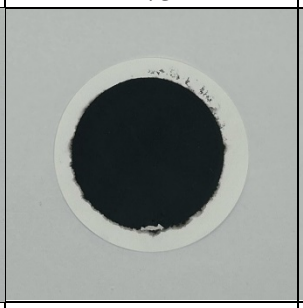	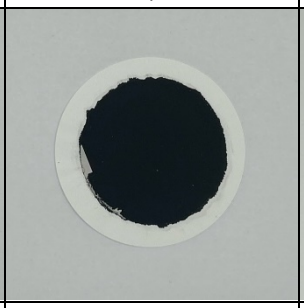	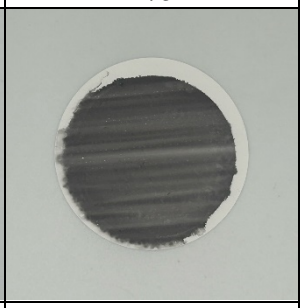
176	177	178	179	180
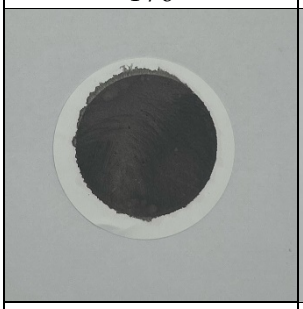	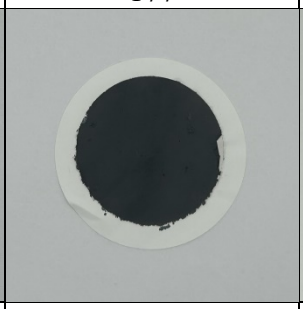	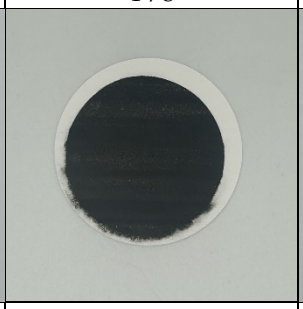	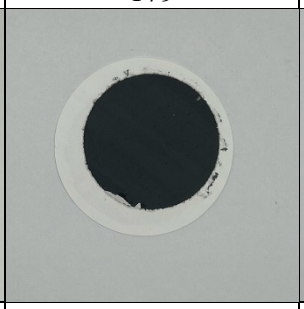	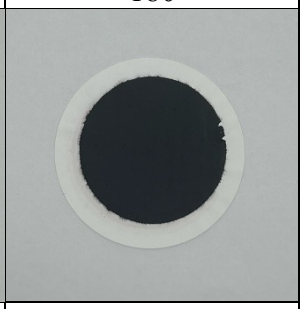
181	182	183	184	185
	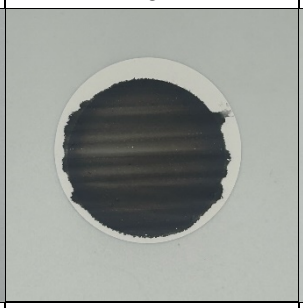	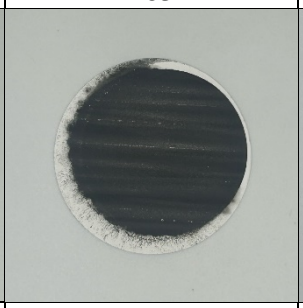	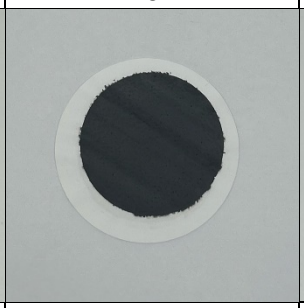	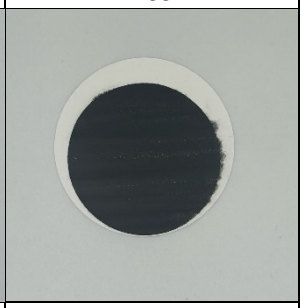
186	187	188	189	190
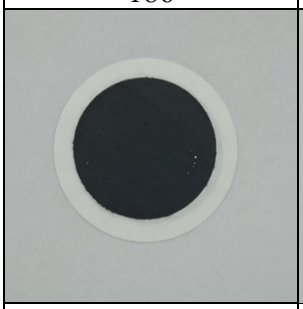	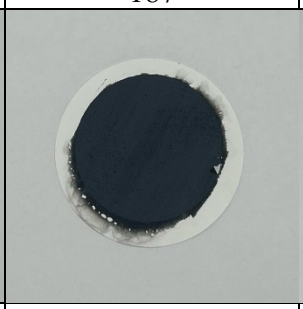	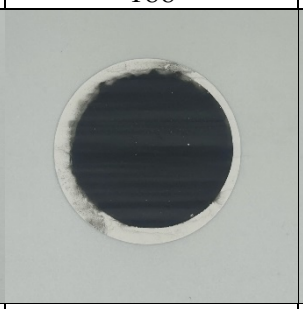	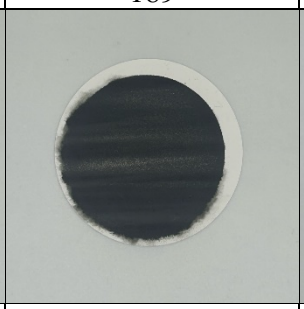	
191	192	193	194	195
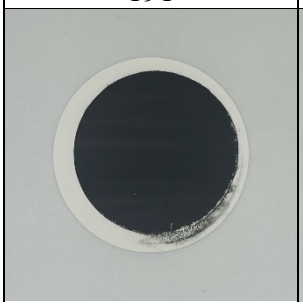	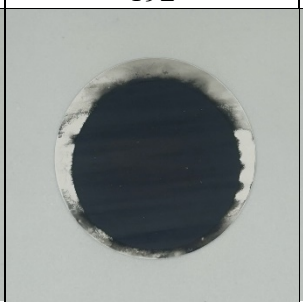	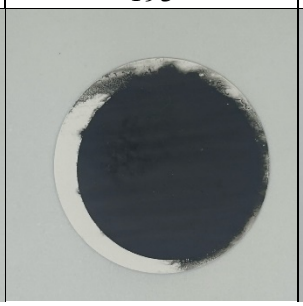	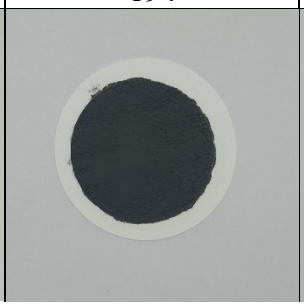	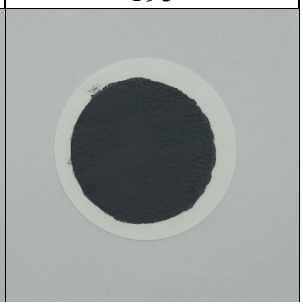

196	197	198	199	200
	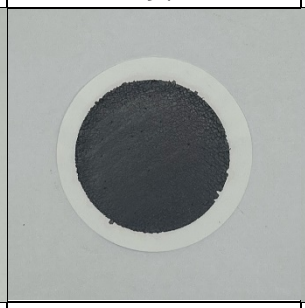	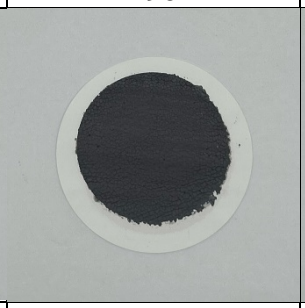		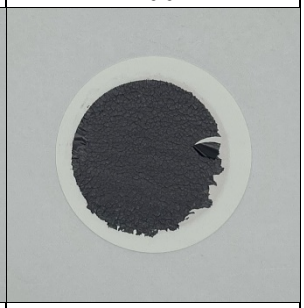
201	202	203	204	205
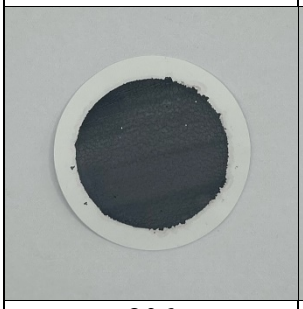	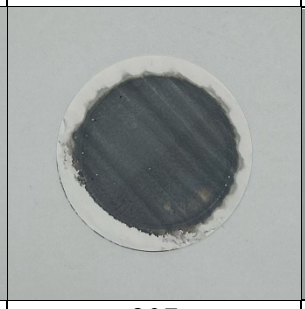		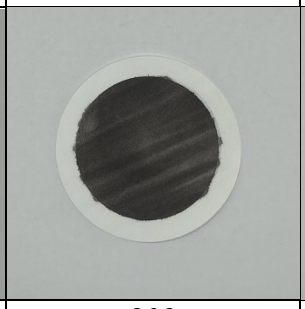	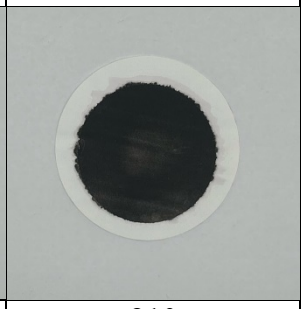
206	207	208	209	210
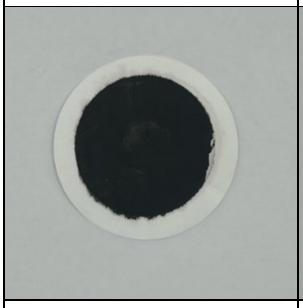	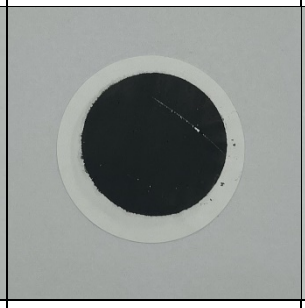	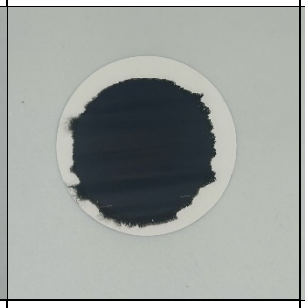	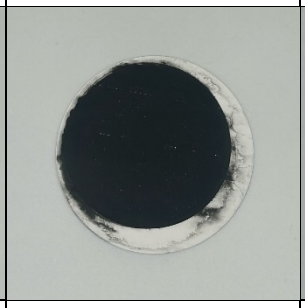	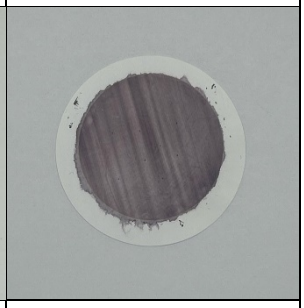
211	212	213	214	215
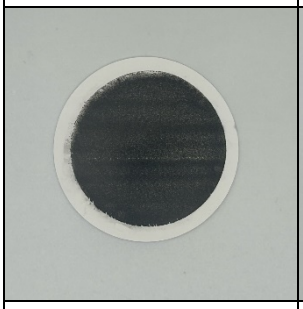	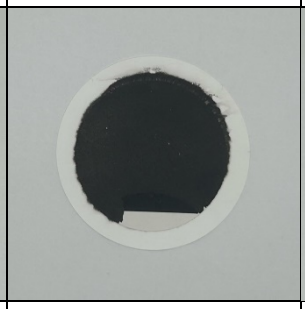	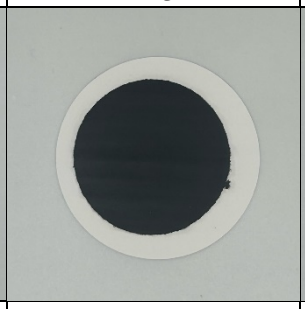	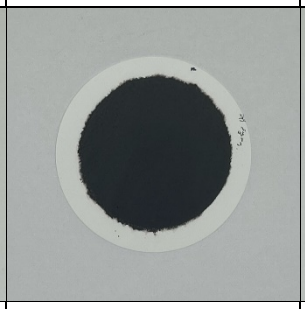	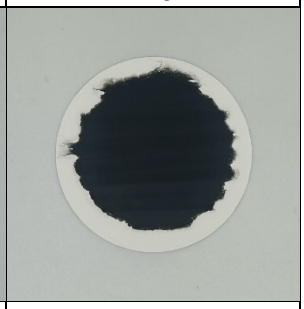
216	217	218	219	220
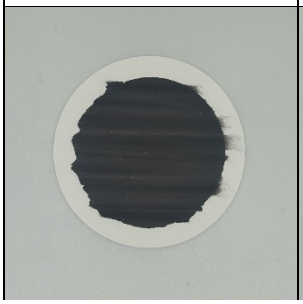	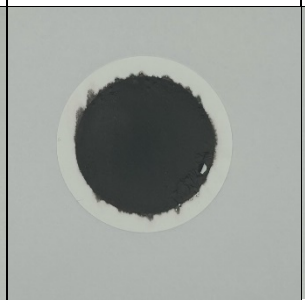	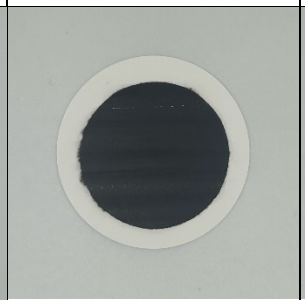	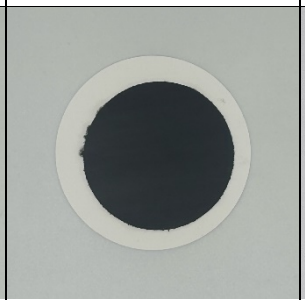	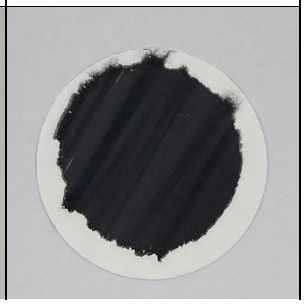

221	222	223	224	225
	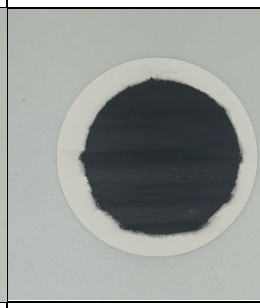	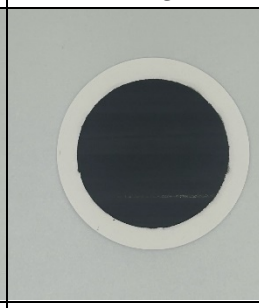	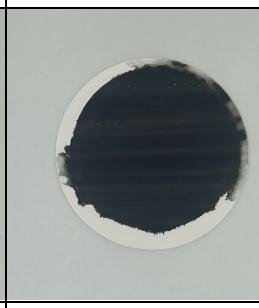	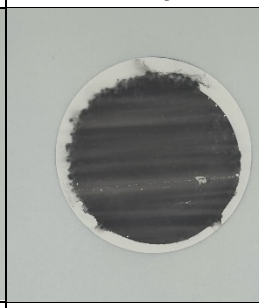
226	227	228	229	230
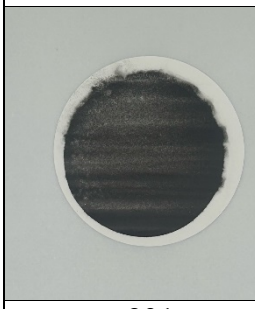	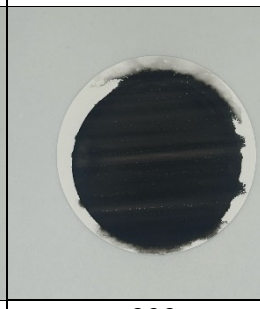		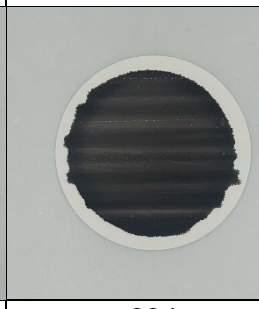	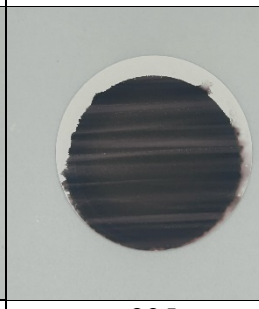
231	232	233	234	235
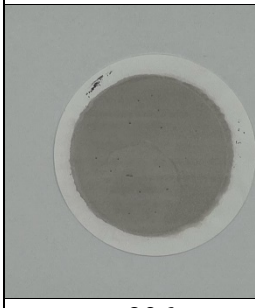	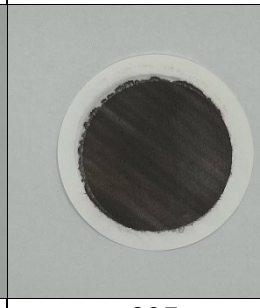	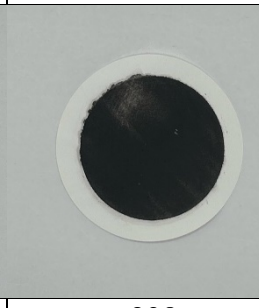	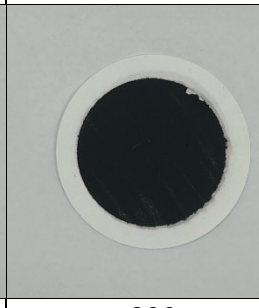	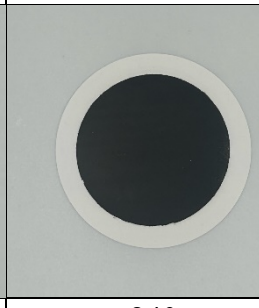
236	237	238	239	240
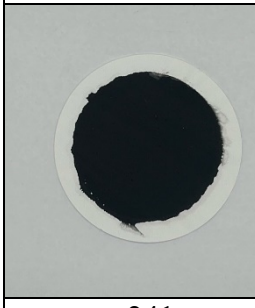		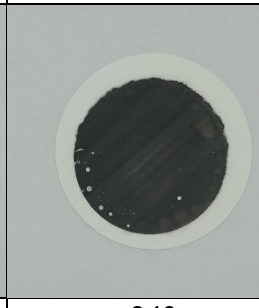	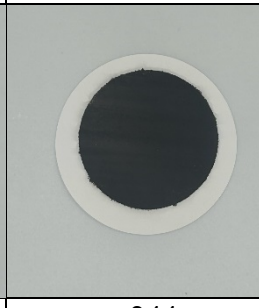	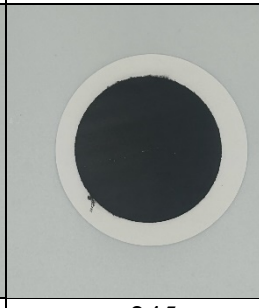
241	242	243	244	245
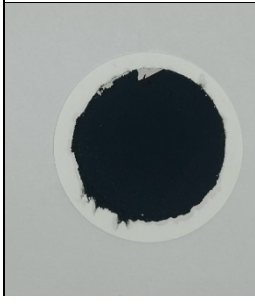	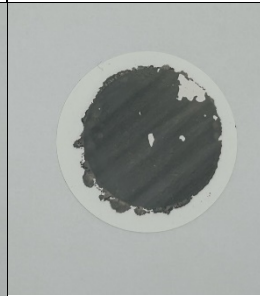	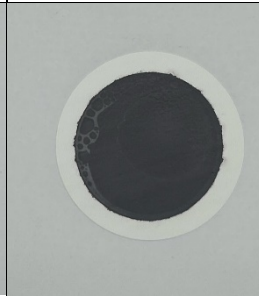	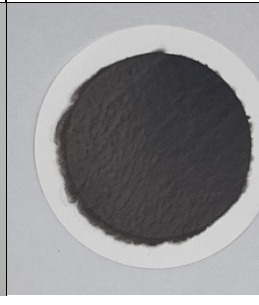	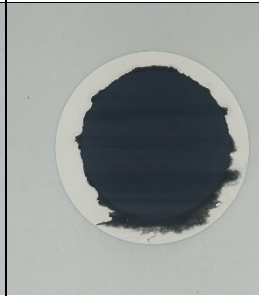

246	247	248	249	250
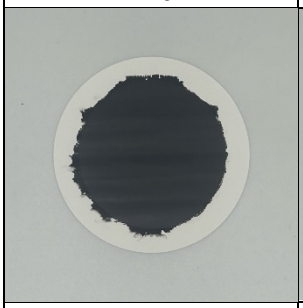	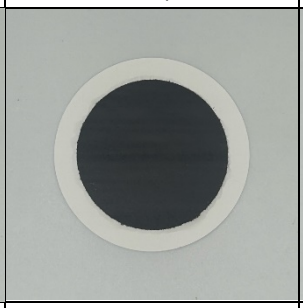	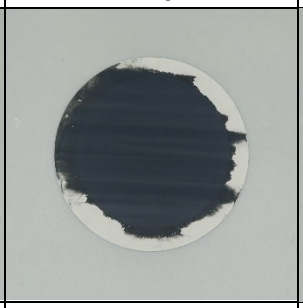	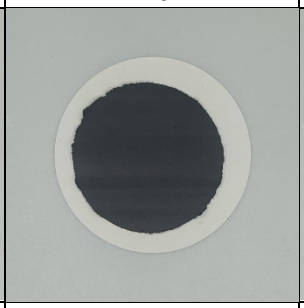	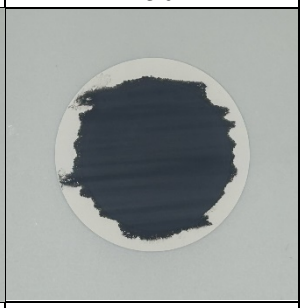
251	252	253	254	255
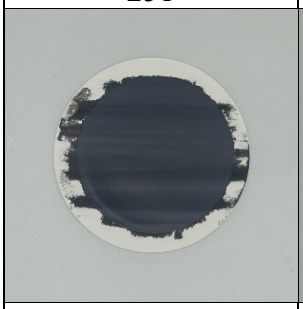	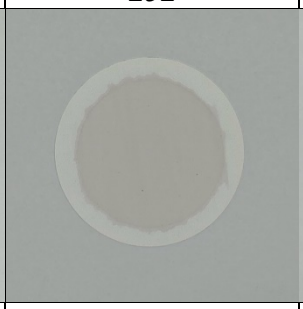	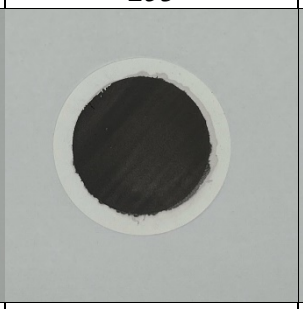	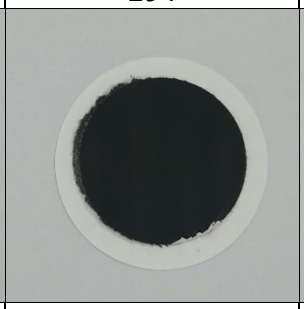	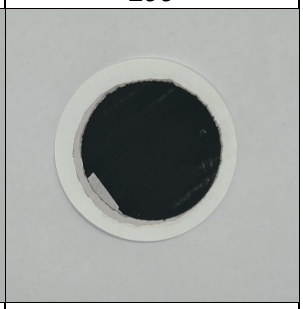
256	257	258	259	260
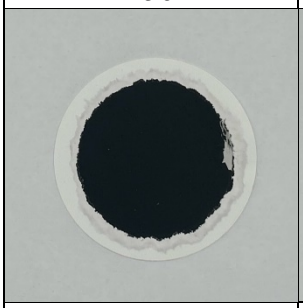	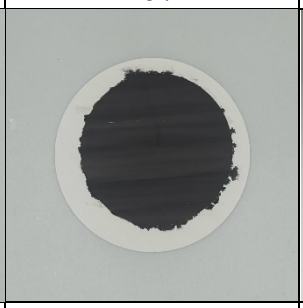	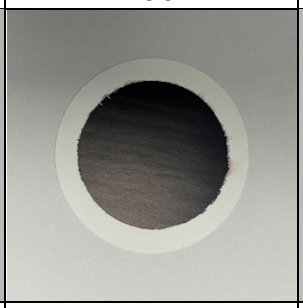	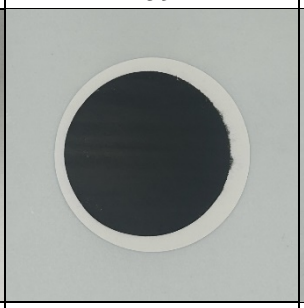	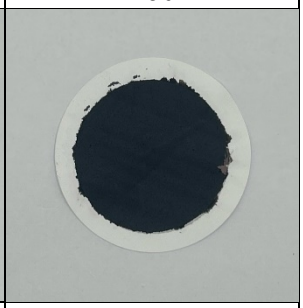
261	262	263	264	265
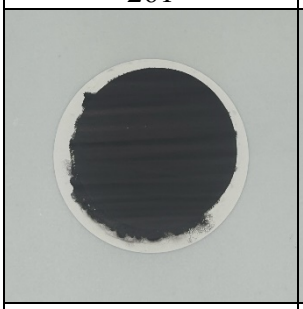	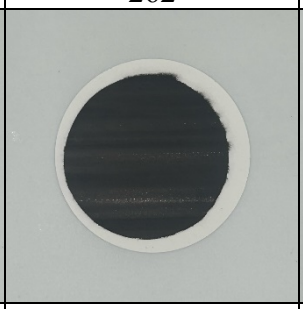	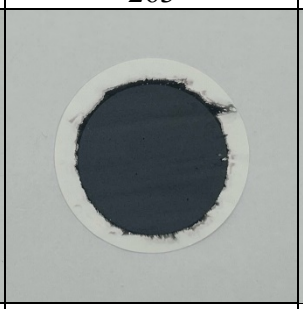	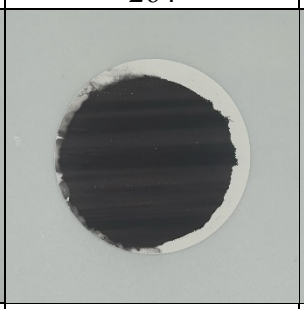	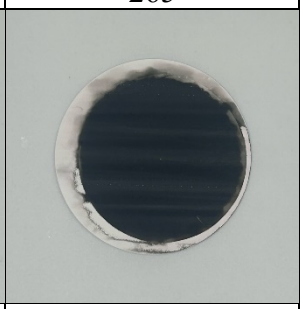
266	267	268	269	270
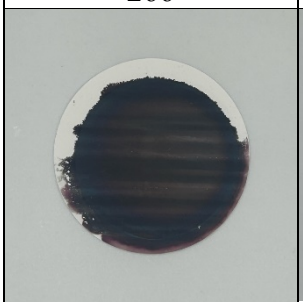		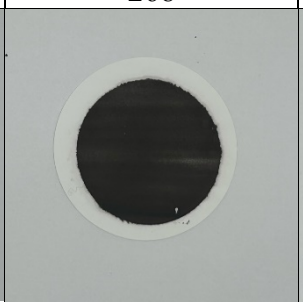	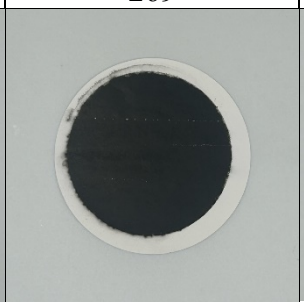	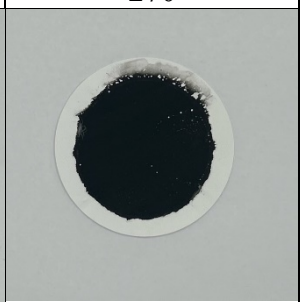

271	272	273	274	275
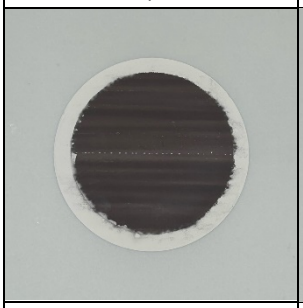	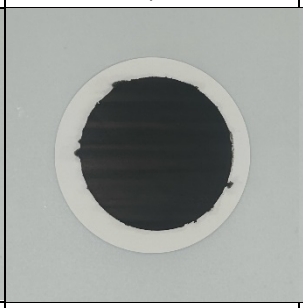	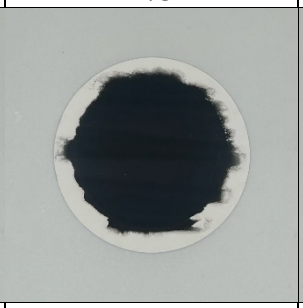	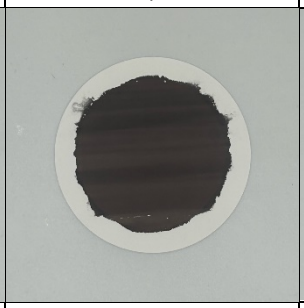	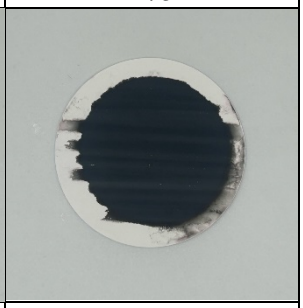
276	277	278	279	280
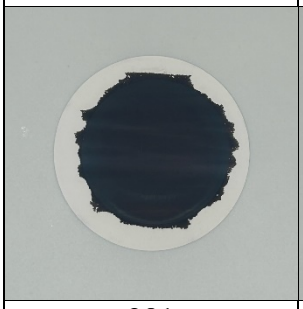	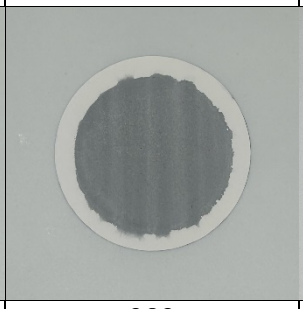	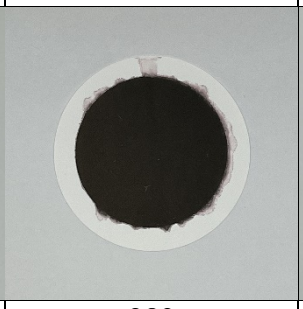	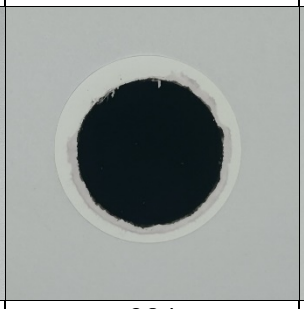	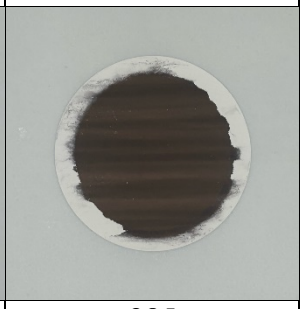
281	282	283	284	285
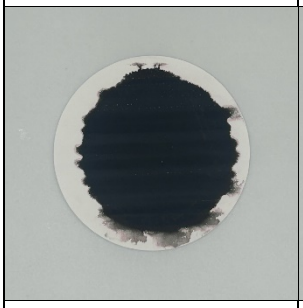	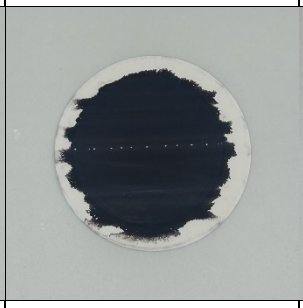		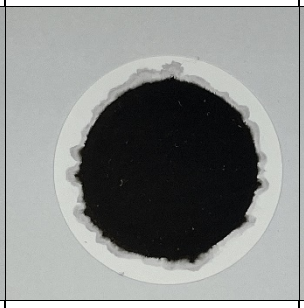	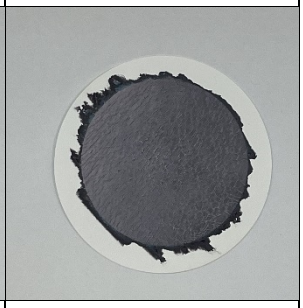
286				
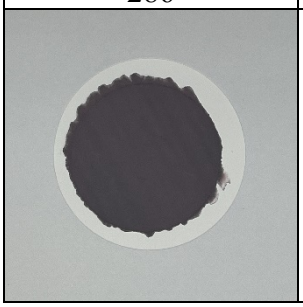				

Table S2. Electrical conductance of 286 G_0 nanocomposites with different MXene/SWNT/AuNP/PVA ratios as the training data points for the SVM regression model.

ID	MXene/SWNT/AuNP/PVA Ratio				S_0 (mS)
	MXene Loading (wt.%)	SWNT Loading (wt.%)	AuNP Loading (wt.%)	PVA Loading (wt.%)	
1	0	0	0	100	0.00
2	10	0	0	90	0.19
3	20	0	0	80	0.32
4	30	0	0	70	0.59
5	40	0	0	60	1.02
6	50	0	0	50	1.39
7	60	0	0	40	3.05
8	70	0	0	30	4.07
9	80	0	0	20	6.29
10	90	0	0	10	8.06
11	100	0	0	0	40.00
12	0	10	0	90	0.00
13	10	10	0	80	0.09
14	20	10	0	70	0.18
15	30	10	0	60	0.33
16	40	10	0	50	0.43
17	50	10	0	40	0.65
18	60	10	0	30	1.15
19	70	10	0	20	4.55
20	80	10	0	10	5.41
21	90	10	0	0	15.15
22	0	20	0	80	0.07
23	10	20	0	70	0.26
24	20	20	0	60	0.53
25	30	20	0	50	0.56
26	40	20	0	40	2.60
27	50	20	0	30	3.29
28	60	20	0	20	3.79
29	70	20	0	10	6.58
30	80	20	0	0	18.18
31	0	30	0	70	0.24
32	10	30	0	60	0.32
33	20	30	0	50	0.53
34	30	30	0	40	2.00
35	40	30	0	30	4.05

36	50	30	0	20	4.59
37	60	30	0	10	5.95
38	70	30	0	0	17.86
39	0	40	0	60	0.07
40	10	40	0	50	0.61
41	20	40	0	40	0.83
42	30	40	0	30	3.24
43	40	40	0	20	5.05
44	50	40	0	10	8.55
45	60	40	0	0	23.26
46	0	50	0	50	0.16
47	10	50	0	40	1.80
48	20	50	0	30	2.94
49	30	50	0	20	4.59
50	40	50	0	10	10.00
51	50	50	0	0	27.78
52	0	60	0	40	0.83
53	10	60	0	30	2.49
54	20	60	0	20	3.73
55	30	60	0	10	7.30
56	40	60	0	0	26.32
57	0	70	0	30	0.78
58	10	70	0	20	2.53
59	20	70	0	10	6.99
60	30	70	0	0	21.28
61	0	80	0	20	0.83
62	10	80	0	10	6.45
63	20	80	0	0	31.25
64	0	90	0	10	5.46
65	10	90	0	0	35.71
66	0	100	0	0	55.56
67	0	0	10	90	0.00
68	10	0	10	80	0.20
69	20	0	10	70	0.34
70	30	0	10	60	0.72
71	40	0	10	50	1.30
72	50	0	10	40	1.90
73	60	0	10	30	3.25
74	70	0	10	20	5.43
75	80	0	10	10	20.00
76	90	0	10	0	28.57

77	0	10	10	80	0.11
78	10	10	10	70	0.16
79	20	10	10	60	0.39
80	30	10	10	50	0.47
81	40	10	10	40	0.69
82	50	10	10	30	3.23
83	60	10	10	20	4.35
84	70	10	10	10	6.17
85	80	10	10	0	21.28
86	0	20	10	70	0.17
87	10	20	10	60	0.25
88	20	20	10	50	0.34
89	30	20	10	40	0.61
90	40	20	10	30	1.10
91	50	20	10	20	3.50
92	60	20	10	10	5.85
93	70	20	10	0	29.41
94	0	30	10	60	0.96
95	10	30	10	50	1.12
96	20	30	10	40	1.48
97	30	30	10	30	3.77
98	40	30	10	20	4.76
99	50	30	10	10	7.69
100	60	30	10	0	22.22
101	0	40	10	50	0.75
102	10	40	10	40	2.52
103	20	40	10	30	4.74
104	30	40	10	20	5.05
105	40	40	10	10	8.33
106	50	40	10	0	33.33
107	0	50	10	40	1.95
108	10	50	10	30	4.39
109	20	50	10	20	6.10
110	30	50	10	10	7.69
111	40	50	10	0	20.83
112	0	60	10	30	3.31
113	10	60	10	20	4.24
114	20	60	10	10	7.09
115	30	60	10	0	18.52
116	0	70	10	20	2.76
117	10	70	10	10	6.76

118	20	70	10	0	16.67
119	0	80	10	10	4.13
120	10	80	10	0	16.13
121	0	90	10	0	15.15
122	0	0	20	80	0.00
123	10	0	20	70	0.43
124	20	0	20	60	0.71
125	30	0	20	50	2.50
126	40	0	20	40	4.13
127	50	0	20	30	6.62
128	60	0	20	20	10.10
129	70	0	20	10	12.66
130	80	0	20	0	25.00
131	0	10	20	70	0.16
132	10	10	20	60	0.23
133	20	10	20	50	0.37
134	30	10	20	40	0.58
135	40	10	20	30	1.43
136	50	10	20	20	3.05
137	60	10	20	10	4.24
138	70	10	20	0	10.75
139	0	20	20	60	0.41
140	10	20	20	50	0.88
141	20	20	20	40	1.14
142	30	20	20	30	2.96
143	40	20	20	20	4.35
144	50	20	20	10	4.57
145	60	20	20	0	33.33
146	0	30	20	50	0.52
147	10	30	20	40	1.28
148	20	30	20	30	3.56
149	30	30	20	20	4.35
150	40	30	20	10	6.58
151	50	30	20	0	10.75
152	0	40	20	40	1.16
153	10	40	20	30	2.99
154	20	40	20	20	4.76
155	30	40	20	10	5.49
156	40	40	20	0	16.39
157	0	50	20	30	2.35
158	10	50	20	20	3.23

159	20	50	20	10	4.72
160	30	50	20	0	11.76
161	0	60	20	20	3.95
162	10	60	20	10	7.63
163	20	60	20	0	35.71
164	0	70	20	10	7.25
165	10	70	20	0	23.81
166	0	80	20	0	22.73
167	0	0	30	70	0.00
168	10	0	30	60	0.32
169	20	0	30	50	0.73
170	30	0	30	40	1.78
171	40	0	30	30	4.17
172	50	0	30	20	9.35
173	60	0	30	10	14.08
174	70	0	30	0	28.57
175	0	10	30	60	0.25
176	10	10	30	50	0.56
177	20	10	30	40	0.82
178	30	10	30	30	2.08
179	40	10	30	20	3.80
180	50	10	30	10	4.59
181	60	10	30	0	14.49
182	0	20	30	50	0.68
183	10	20	30	40	1.20
184	20	20	30	30	1.84
185	30	20	30	20	3.37
186	40	20	30	10	6.10
187	50	20	30	0	31.25
188	0	30	30	40	0.65
189	10	30	30	30	1.60
190	20	30	30	20	2.33
191	30	30	30	10	4.13
192	40	30	30	0	34.48
193	0	40	30	30	2.30
194	10	40	30	20	3.48
195	20	40	30	10	7.58
196	30	40	30	0	18.87
197	0	50	30	20	5.38
198	10	50	30	10	7.69
199	20	50	30	0	21.28

200	0	60	30	10	9.43
201	10	60	30	0	21.74
202	0	70	30	0	18.87
203	0	0	40	60	0.00
204	10	0	40	50	0.83
205	20	0	40	40	1.73
206	30	0	40	30	3.79
207	40	0	40	20	7.25
208	50	0	40	10	10.64
209	60	0	40	0	6.94
210	0	10	40	50	0.43
211	10	10	40	40	0.54
212	20	10	40	30	1.20
213	30	10	40	20	3.22
214	40	10	40	10	5.21
215	50	10	40	0	8.20
216	0	20	40	40	1.01
217	10	20	40	30	1.57
218	20	20	40	20	2.82
219	30	20	40	10	4.26
220	40	20	40	0	11.36
221	0	30	40	30	1.79
222	10	30	40	20	3.07
223	20	30	40	10	5.21
224	30	30	40	0	13.70
225	0	40	40	20	5.24
226	10	40	40	10	6.17
227	20	40	40	0	38.46
228	0	50	40	10	8.55
229	10	50	40	0	47.62
230	0	60	40	0	12.82
231	0	0	50	50	0.00
232	10	0	50	40	0.80
233	20	0	50	30	1.87
234	30	0	50	20	7.25
235	40	0	50	10	8.26
236	50	0	50	0	28.57
237	0	10	50	40	0.49
238	10	10	50	30	0.89
239	20	10	50	20	1.29
240	30	10	50	10	3.34

241	40	10	50	0	12.35
242	0	20	50	30	2.22
243	10	20	50	20	4.12
244	20	20	50	10	4.65
245	30	20	50	0	11.49
246	0	30	50	20	6.49
247	10	30	50	10	7.75
248	20	30	50	0	38.46
249	0	40	50	10	8.55
250	10	40	50	0	19.23
251	0	50	50	0	20.83
252	0	0	60	40	0.00
253	10	0	60	30	1.15
254	20	0	60	20	5.10
255	30	0	60	10	8.85
256	40	0	60	0	29.41
257	0	10	60	30	0.22
258	10	10	60	20	0.38
259	20	10	60	10	3.42
260	30	10	60	0	13.16
261	0	20	60	20	4.65
262	10	20	60	10	5.78
263	20	20	60	0	30.30
264	0	30	60	10	10.10
265	10	30	60	0	37.04
266	0	40	60	0	9.80
267	0	0	70	30	0.00
268	10	0	70	20	4.85
269	20	0	70	10	6.37
270	30	0	70	0	25.64
271	0	10	70	20	2.22
272	10	10	70	10	6.90
273	20	10	70	0	8.47
274	0	20	70	10	10.10
275	10	20	70	0	9.35
276	0	30	70	0	10.42
277	0	0	80	20	0.00
278	10	0	80	10	2.70
279	20	0	80	0	29.41
280	0	10	80	10	3.69
281	10	10	80	0	17.86

282	0	20	80	0	10.00
283	0	0	90	10	0.00
284	10	0	90	0	22.22
285	0	10	90	0	5.15
286	0	0	100	0	0.00

Table S3. Photos of 42 G_0 nanocomposites with different MXene/SWNT/AuNP/PVA ratios as the testing data points for the SVM regression model.

1	2	3	4	5
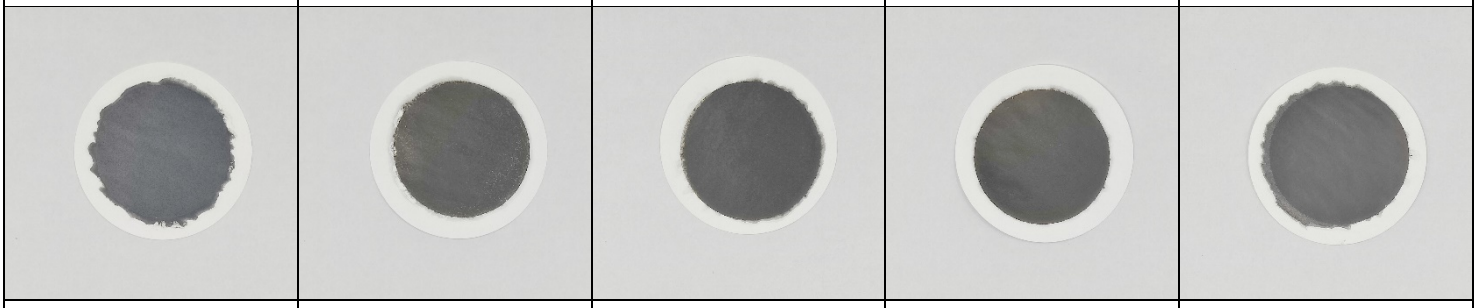				
6	7	8	9	10
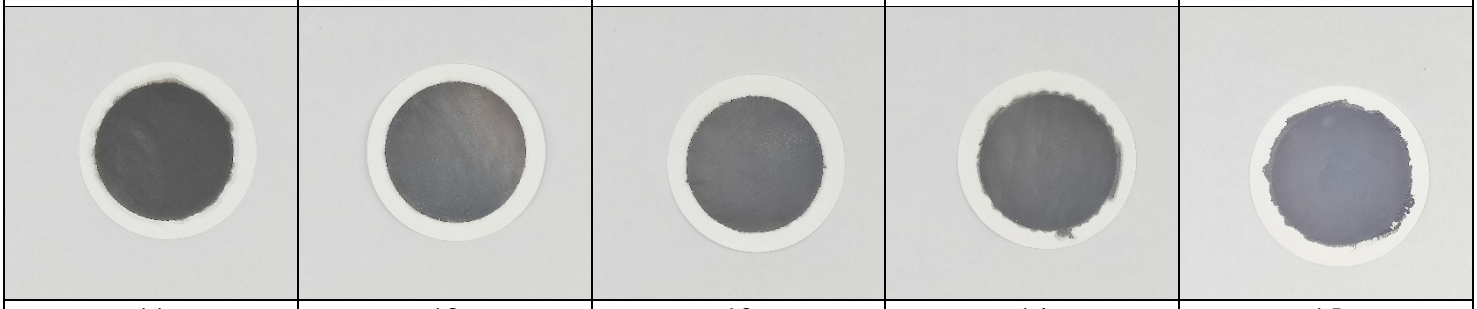				
11	12	13	14	15
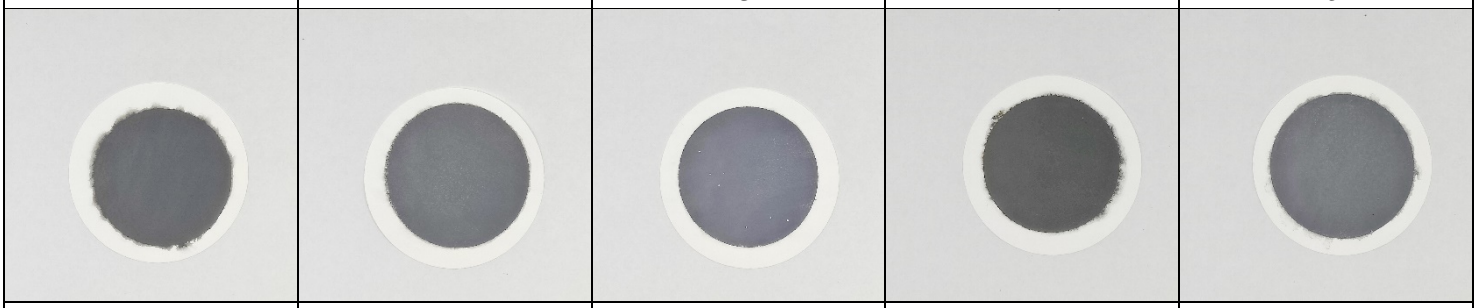				
16	17	18	19	20
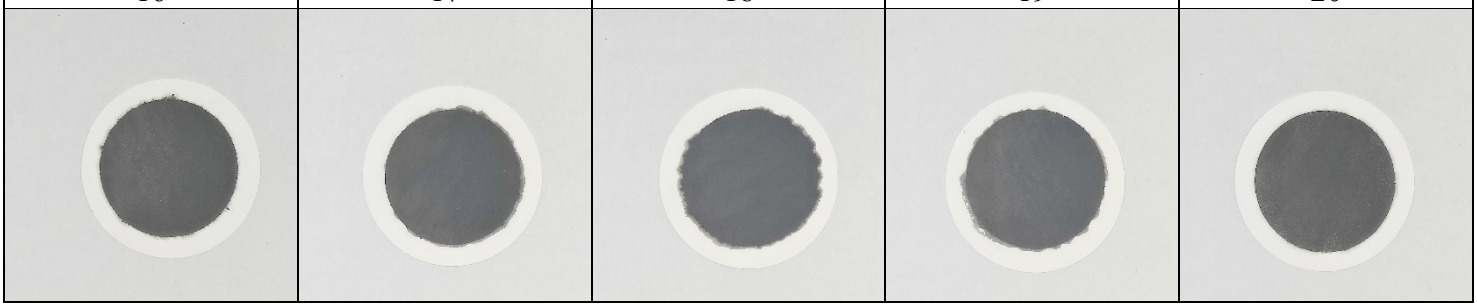				

21	22	23	24	25
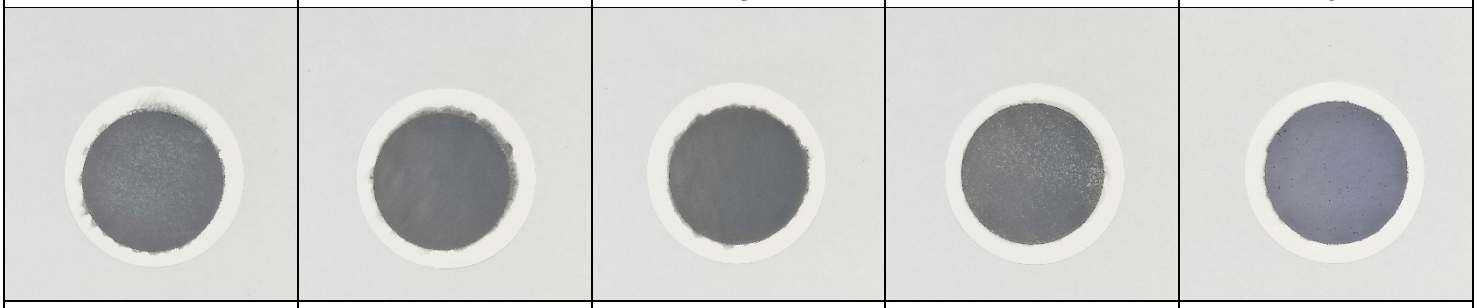				
26	27	28	29	30
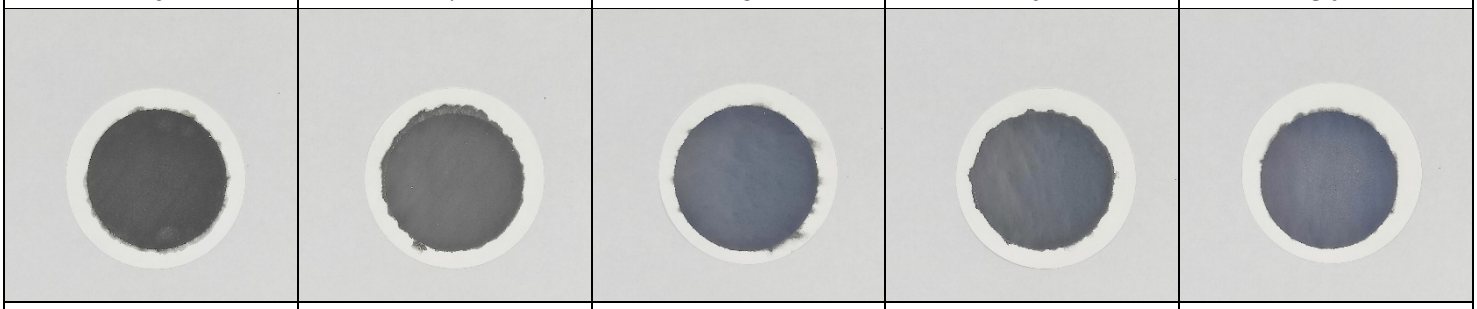				
31	32	33	34	35
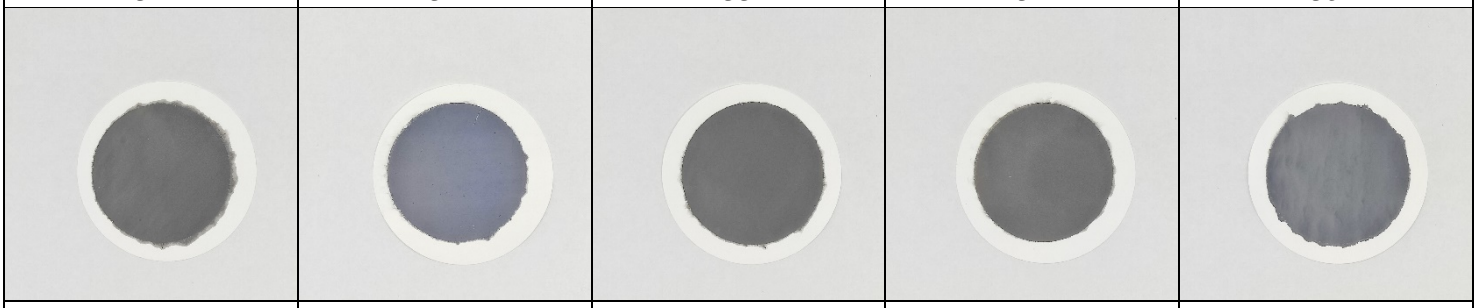				
36	37	38	39	40
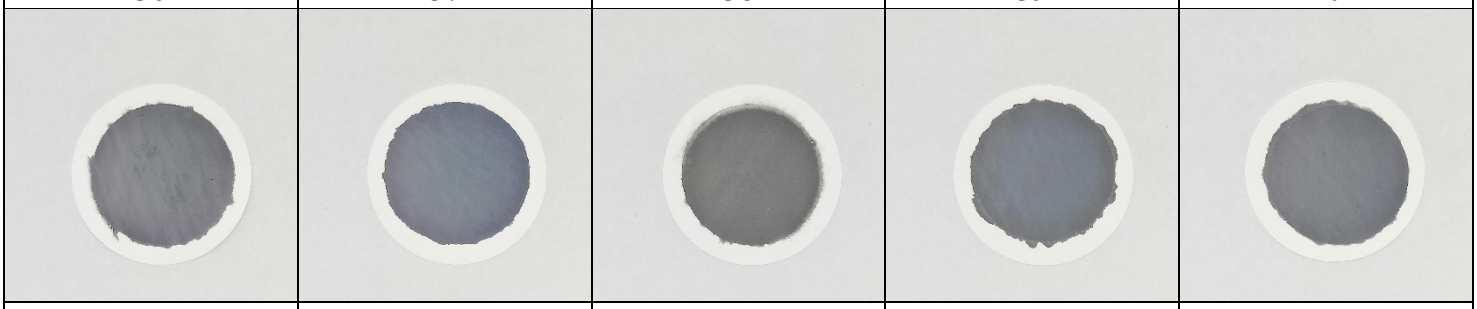				
41	42			
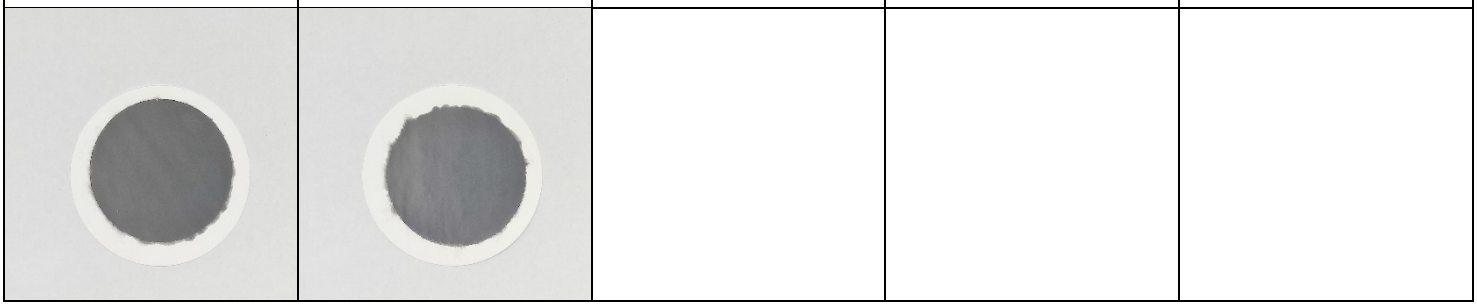				

Table S4. Electrical conductance of 42 G_0 nanocomposites with different MXene/SWNT/AuNP/PVA ratios as the testing data points for the SVM regression model.

ID	MXene/SWNT/AuNP/PVA Ratio				S_0 (mS)
	MXene Loading (wt.%)	SWNT Loading (wt.%)	AuNP Loading (wt.%)	PVA Loading (wt.%)	
1	49.5	50.5	0.0	0.0	76.92
2	12.7	41.0	41.3	5.0	7.87
3	12.3	78.3	6.5	2.9	12.50
4	7.2	30.0	59.4	3.4	8.33
5	34.9	32.1	31.0	2.1	7.14
6	4.9	86.9	6.2	2.0	20.00
7	40.2	44.8	21.4	3.6	13.51
8	40.2	42.4	8.8	8.6	8.77
9	45.8	36.8	13.9	3.5	7.14
10	84.4	4.6	8.6	2.4	7.58
11	17.5	67.0	9.2	6.4	8.55
12	41.9	33.8	9.4	14.9	2.22
13	65.9	15.3	6.8	12.0	3.12
14	5.7	79.0	7.7	7.6	14.29
15	55.9	32.6	5.3	6.2	6.90
16	12.5	53.2	24.3	10.0	2.50
17	23.6	63.4	11.0	1.9	8.93
18	20.2	47.8	20.8	11.3	2.22
19	36.3	56.9	4.9	1.9	8.13
20	7.4	76.5	7.5	8.6	7.25
21	55.8	35.2	6.6	2.4	8.33
22	29.4	51.5	15.1	4.1	7.35
23	25.5	63.6	8.2	2.6	8.47
24	27.2	52.9	10.8	9.1	6.76
25	73.7	7.2	5.4	13.7	2.58
26	5.8	53.3	0.0	40.8	1.13
27	12.5	21.7	11.7	54.2	0.39
28	38.3	20.3	7.2	34.2	0.32
29	30.0	19.2	17.5	33.3	0.36
30	70.0	9.2	7.0	13.8	2.28
31	18.3	38.3	25.0	18.3	2.02
32	70.8	4.7	8.7	15.8	2.14
33	6.3	42.8	16.7	34.2	1.18
34	8.7	38.8	12.5	40.0	0.91
35	28.3	11.7	28.3	31.7	0.21

36	25.0	10.0	34.2	30.8	0.17
37	41.7	13.3	10.0	35.0	0.19
38	7.5	26.7	0.0	65.8	0.43
39	18.3	17.5	15.8	48.3	0.29
40	32.5	18.3	19.2	30.0	0.35
41	12.5	43.3	15.8	28.3	1.05
42	23.3	18.3	41.7	16.7	0.50

Table S5. Training data points for the prediction model.

Round #	Composition Labels				Thickness Labels	Deformation Labels	Strain Labels	Electrical Labels	Response Labels		
	MXene Loading (wt.%)	SWNT Loading (wt.%)	AuNP Loading (wt.%)	PVA Loading (wt.%)	Thickness (nm)	Deformation Sequence	Pre-Strain (%)	S_0 (mS)	$\varepsilon_{5\%}$ (%)	$\varepsilon_{7.5\%}$ (%)	$\varepsilon_{10\%}$ (%)
1	61.0	20.0	15.0	4.0	1,200	G_1–1D	0	5.57	67	67	67
1	5.0	80.0	5.0	10.0	1,200	G_2–2D2D	100	9.06	198	202	206
1	46.0	40.0	10.0	4.0	1,200	G_2–2D2D	300	13.39	240	291	330
1	56.0	40.0	0.0	4.0	800	G_2–2D1D	100	9.05	209	218	222
1	67.0	15.0	15.0	3.0	1,200	G_2–2D1D	100	19.92	200	217	229
1	23.5	50.0	25.0	1.5	1,600	G_1–2D	0	20.16	43	45	47
1	100.0	0.0	0.0	0.0	1,600	G_1–2D	0	128.21	30	33	33
1	0.0	93.0	5.0	2.0	1,200	G_2–2D2D	200	15.34	383	388	393
1	25.0	70.0	2.0	3.0	1,600	G_1–2D	0	29.41	35	38	40
1	20.0	80.0	0.0	0.0	1,200	G_2–2D2D	200	20.16	266	341	363
1	49.5	50.5	0.0	0.0	1,200	G_2–2D2D	100	31.15	184	194	201
1	12.7	41.0	41.3	5.0	1,200	G_2–2D1D	200	7.48	415	450	460
1	12.3	78.3	6.5	2.9	1,200	G_2–2D1D	300	8.52	564	586	602
1	17.0	45.6	31.9	5.4	800	G_1–1D	0	6.48	93	93	93
2	7.2	30.0	59.4	3.4	1,200	G_2–2D1D	100	7.70	264	269	270
2	34.9	32.1	31.0	2.1	800	G_2–2D2D	200	6.62	279	296	305
2	10.0	32.0	50.0	8.0	1,600	G_2–2D2D	200	4.64	341	361	369
2	35.0	58.0	1.0	6.0	800	G_2–2D2D	200	10.38	305	315	323
2	42.0	30.0	15.0	13.0	1,600	G_2–2D2D	100	7.65	188	205	216
2	3.9	87.9	6.2	2.0	1,200	G_1–1D	0	16.21	83	84	85
2	2.8	31.4	57.9	7.9	1,200	G_1–2D	0	7.70	40	43	45
2	30.2	34.8	21.4	13.6	800	G_1–2D	0	6.59	33	35	36
2	24.6	40.0	27.9	7.6	1,600	G_1–1D	0	15.20	40	42	42

2	34.8	35.4	21.6	8.2	800	G_1–2D	0	8.81	43	48	50
2	40.2	42.4	8.8	8.6	1,600	G_2–2D1D	200	15.92	281	303	316
2	17.9	7.6	68.1	6.5	1,200	G_2–2D2D	100	9.94	262	267	269
2	45.8	36.8	13.9	3.5	1,200	G_2–2D2D	200	23.75	296	320	332
2	36.6	38.0	23.8	1.7	800	G_2–2D2D	100	8.18	185	197	208
2	4.2	41.0	51.6	3.2	1,600	G_2–2D1D	100	15.53	364	369	381
2	84.4	4.6	8.6	2.4	1,600	G_1–2D	0	22.32	28	31	33
2	19.6	47.7	31.4	1.2	800	G_1–2D	0	13.51	62	64	66
2	55.9	23.6	13.1	7.5	800	G_1–2D	0	6.03	45	50	53
2	17.5	67.0	9.2	6.4	1,200	G_2–2D1D	100	13.26	234	239	242
2	41.9	33.8	9.4	14.9	1,200	G_2–2D1D	100	5.62	277	286	292
2	15.7	63.7	13.5	7.1	1,600	G_2–2D1D	100	10.96	284	290	293
2	3.3	69.8	16.3	10.6	1,200	G_2–2D1D	100	11.39	308	312	315
3	54.5	23.3	9.2	13.1	1,600	G_2–2D1D	200	6.96	333	365	374
3	3.5	58.4	30.9	7.2	1,200	G_1–1D	0	17.01	81	82	82
3	14.6	52.7	24.3	8.4	800	G_1–1D	0	5.95	57	58	58
3	13.6	69.0	13.1	4.3	800	G_1–1D	0	6.27	62	64	64
3	31.0	45.6	15.6	7.8	800	G_1–1D	0	7.13	81	83	86
3	65.9	15.3	6.8	12.0	800	G_1–2D	0	6.73	47	50	53
3	80.7	11.6	2.5	5.2	1,200	G_1–1D	0	18.45	133	133	135
3	64.2	7.4	13.8	14.7	1,200	G_2–2D2D	100	8.01	151	160	166
3	12.0	62.2	18.0	7.8	1,600	G_2–2D1D	300	6.37	499	525	539
3	9.4	19.6	68.8	2.3	1,600	G_1–2D	0	17.12	38	44	46
3	5.7	79.0	7.7	7.6	1,600	G_2–2D2D	300	6.16	649	660	671
3	42.0	40.3	9.7	7.9	1,600	G_1–1D	0	20.08	73	74	76
3	7.3	55.0	32.4	5.3	1,600	G_2–2D1D	300	6.93	540	576	612
3	42.4	24.4	18.1	15.1	1,200	G_1–1D	0	7.49	89	90	91
3	10.3	28.6	59.2	2.0	800	G_1–2D	0	9.31	60	62	63
3	55.9	34.6	3.3	6.2	1,200	G_1–1D	0	18.83	44	45	45
3	38.2	20.8	37.5	3.5	1,200	G_1–1D	0	9.35	107	108	108

3	83.5	1.7	10.4	4.4	1,600	G_1–2D	0	41.67	77	86	94
3	32.0	32.1	32.2	3.7	800	G_1–1D	0	6.51	105	106	106
3	4.2	73.7	19.7	2.4	1,600	G_2–2D1D	200	11.19	391	408	416
3	31.8	50.6	16.3	1.4	800	G_1–1D	0	20.24	37	37	38
3	90.3	3.7	4.7	1.3	800	G_2–2D1D	200	14.49	265	283	299
4	12.5	53.2	24.3	10.0	1,600	G_2–2D1D	100	5.12	260	261	263
4	23.6	63.4	11.0	1.9	800	G_1–1D	0	8.06	42	43	43
4	36.1	35.8	19.5	8.6	1,600	G_2–2D2D	100	5.49	196	203	209
4	20.2	47.8	20.8	11.3	800	G_1–2D	0	6.21	35	37	38
4	5.8	86.3	5.7	2.2	1,200	G_2–2D2D	100	12.66	220	224	229
4	20.0	56.1	17.3	6.7	1,200	G_2–2D1D	200	4.96	363	386	402
4	15.3	77.0	2.1	5.7	800	G_2–2D2D	100	8.51	211	217	222
4	19.9	37.1	41.4	1.6	1,600	G_2–2D1D	100	8.42	214	225	229
4	36.3	58.9	3.5	1.3	1,200	G_2–2D1D	100	9.31	215	222	225
4	38.3	31.2	20.1	10.4	1,600	G_1–2D	0	7.07	31	34	38
4	9.8	59.0	22.0	9.2	1,600	G_2–2D1D	200	3.62	447	467	478
4	3.4	80.5	7.5	8.6	1,600	G_2–2D2D	300	6.51	432	438	446
4	55.8	38.2	4.6	1.4	1,600	G_2–2D1D	200	26.88	184	261	284
4	5.9	69.4	18.9	5.9	1,200	G_2–2D2D	300	6.45	602	606	606
4	59.2	20.1	9.3	11.4	1,600	G_2–2D1D	200	7.06	232	244	253
4	30.7	47.5	15.0	6.8	1,200	G_2–2D1D	300	7.69	375	393	401
4	52.3	28.6	16.4	2.8	1,600	G_2–2D2D	200	12.27	161	189	209
4	74.3	15.0	9.0	1.7	800	G_2–2D1D	100	9.92	178	185	189
4	5.9	60.3	29.2	4.6	1,600	G_2–2D2D	300	11.63	471	505	521
4	29.4	51.5	15.1	4.1	1,200	G_2–2D2D	200	6.26	300	317	325
4	7.4	54.1	32.9	5.7	1,200	G_2–2D1D	200	8.70	442	447	454
4	25.5	63.6	8.2	2.6	1,600	G_2–2D2D	200	9.12	240	256	273
5	20.5	55.1	20.7	3.7	1,600	G_2–2D2D	300	8.67	365	381	404
5	8.0	52.9	31.8	7.4	1,600	G_2–2D2D	300	8.26	363	374	381
5	27.6	62.5	4.2	5.7	1,200	G_2–2D1D	200	6.87	445	456	461

5	8.1	79.0	11.7	1.3	1,200	G_2–2D1D	300	8.08	575	589	602
5	7.0	19.8	69.5	3.7	1,200	G_2–2D2D	200	2.71	330	352	363
5	32.7	32.3	28.3	6.7	1,200	G_2–2D2D	200	7.39	264	292	307
5	24.9	42.2	26.2	6.7	1,200	G_2–2D2D	200	5.06	329	350	363
5	5.8	32.3	59.5	2.5	1,200	G_2–2D2D	200	8.00	354	364	370
5	27.2	52.9	10.8	9.1	1,600	G_2–2D2D	300	5.13	312	315	319
5	55.3	35.2	6.1	3.4	800	G_2–2D1D	100	10.33	51	100	162
5	33.2	51.4	6.1	9.3	1,200	G_2–2D2D	200	3.85	290	305	313
5	50.9	36.6	6.2	6.3	800	G_1–2D	0	11.63	32	37	38
5	13.6	71.0	8.3	7.1	1,200	G_1–2D	0	15.53	24	26	28
5	20.2	63.4	9.7	6.8	800	G_1–2D	0	11.36	33	35	36
5	78.7	9.3	3.3	8.7	1,200	G_2–2D2D	100	6.52	199	214	226
5	10.0	57.1	27.5	5.4	1,600	G_2–2D2D	200	8.72	236	296	338
5	33.0	45.8	13.9	7.3	1,600	G_2–2D2D	200	8.45	324	369	396
5	63.7	26.9	7.6	1.8	1,600	G_1–1D	0	23.04	126	126	127
5	5.7	73.8	16.7	3.8	1,600	G_1–1D	0	26.25	63	64	64
5	11.4	79.4	4.7	4.5	1,200	G_2–2D2D	200	8.83	333	345	350
5	22.7	22.6	49.2	5.5	1,200	G_2–2D2D	100	4.08	200	215	222
5	51.4	27.4	13.1	8.1	1,600	G_1–1D	0	5.63	100	102	103
6	55.0	30.7	11.0	3.3	800	G_1–2D	0	10.26	27	30	30
6	84.1	1.6	7.0	7.4	1,600	G_2–2D1D	100	15.46	200	203	206
6	11.7	45.7	36.0	6.6	1,200	G_2–2D2D	200	4.29	343	361	371
6	16.1	26.0	52.3	5.6	1,600	G_2–2D1D	100	11.01	172	183	190
6	35.1	46.2	9.0	9.7	1,200	G_1–1D	0	8.46	94	97	100
6	24.3	56.6	13.4	5.7	800	G_2–2D1D	100	6.64	249	251	254
6	10.8	42.8	43.2	3.2	1,200	G_2–2D1D	200	5.64	372	382	392
6	13.2	71.0	6.3	9.5	800	G_2–2D1D	200	3.93	310	324	338
6	12.1	70.7	13.5	3.8	1,600	G_2–2D1D	200	8.66	389	406	415
6	8.9	57.1	31.2	2.8	1,200	G_2–2D1D	200	7.24	343	347	350
6	14.0	67.9	8.1	10.1	1,600	G_2–2D1D	300	3.70	476	496	502

6	40.7	40.6	16.9	1.9	1,200	G_2–2D1D	200	16.13	315	331	343
6	24.4	68.9	5.5	1.3	1,200	G_2–2D2D	200	15.20	433	456	472
6	38.8	29.6	29.2	2.4	1,200	G_2–2D2D	100	6.46	150	157	162
6	34.0	27.2	31.2	7.6	1,200	G_1–2D	0	5.70	36	41	43
6	77.1	2.3	11.2	9.5	1,600	G_2–2D2D	100	3.95	136	157	161
6	82.2	14.1	2.0	1.7	1,200	G_2–2D1D	200	11.53	288	306	320
6	20.6	67.9	3.0	8.5	1,600	G_2–2D1D	300	6.68	425	457	464
6	13.6	55.5	24.7	6.2	1,600	G_2–2D1D	300	5.81	498	511	536
6	74.1	15.0	9.0	1.9	1,200	G_2–2D1D	200	5.52	323	333	348
6	44.9	24.2	25.2	5.7	1,600	G_2–2D2D	100	5.74	120	139	156
6	40.4	45.1	5.6	8.9	1,600	G_2–2D1D	100	9.05	217	230	241
7	17.4	71.2	5.9	5.6	800	G_1–1D	0	9.18	44	44	44
7	47.8	20.8	24.5	6.8	800	G_1–1D	0	5.48	135	135	135
7	52.6	28.3	11.2	7.9	1,600	G_2–2D2D	100	5.60	179	188	196
7	46.4	27.2	21.3	5.1	800	G_1–1D	0	9.78	64	65	65
7	43.1	23.4	30.5	3.0	1,600	G_2–2D1D	100	15.67	210	217	225
7	65.3	17.9	12.5	4.3	1,600	G_2–2D1D	200	8.76	250	308	340
7	41.8	34.7	15.6	7.8	1,200	G_2–2D1D	200	4.74	327	336	345
7	28.1	50.6	14.0	7.3	800	G_1–1D	0	5.35	82	82	82
7	7.2	69.6	19.0	4.3	1,600	G_2–2D2D	100	11.39	259	262	264
7	9.5	50.7	36.4	3.4	800	G_1–1D	0	7.09	76	76	77
7	45.2	32.4	12.8	9.7	1,200	G_2–2D2D	100	6.97	211	215	219
7	75.4	4.5	11.3	8.8	1,200	G_2–2D2D	100	9.90	227	231	235
7	58.5	17.3	15.4	8.8	1,600	G_2–2D1D	100	6.75	212	221	232
7	52.9	22.9	21.5	2.8	1,200	G_2–2D1D	200	10.33	301	340	359
7	22.0	38.1	36.1	3.8	1,200	G_2–2D1D	200	8.66	410	425	434
7	2.7	65.9	25.7	5.7	1,600	G_1–2D	0	13.39	28	29	30
7	50.5	34.9	9.0	5.6	1,600	G_2–2D1D	100	9.78	201	205	209
7	22.8	31.7	43.3	2.3	800	G_1–1D	0	13.26	74	75	75
7	20.5	27.9	49.3	2.3	1,200	G_2–2D2D	200	5.94	502	526	528

7	33.3	47.4	13.6	5.7	1,600	G_2–2D1D	100	9.35	249	255	260
7	45.3	37.9	12.7	4.1	1,600	G_2–2D1D	200	11.67	406	420	421
7	12.3	70.0	13.8	4.0	1,600	G_2–2D2D	300	7.79	499	557	567

Table S6. Testing data points for the prediction model.

ID	Composition Labels				Thickness Labels	Deformation Labels	Strain Labels	Electrical Labels	Response Labels		
	MXene Loading (wt.%)	SWNT Loading (wt.%)	AuNP Loading (wt.%)	PVA Loading (wt.%)	Thickness (nm)	Deformation Sequence	Pre-Strain (%)	S_0 (mS)	$\varepsilon_{5\%}$ (%)	$\varepsilon_{7.5\%}$ (%)	$\varepsilon_{10\%}$ (%)
01	42.0	47.8	3.6	6.6	1,200	G_2–2D2D	200	11.40	304	325	337
02	19.8	68.4	7.0	4.8	1,600	G_2–2D1D	300	8.14	518	529	546
03	32.3	57.0	5.3	5.3	1,600	G_1–2D	0	24.57	37	37	37
04	54.3	27.3	13.7	4.8	800	G_1–2D	0	13.55	41	45	49
05	39.4	44.0	6.1	10.6	1,600	G_1–1D	0	8.48	75	75	75
06	64.5	22.0	6.4	7.2	1,600	G_2–2D2D	200	7.04	188	209	225
07	65.6	14.1	19.0	1.3	1,200	G_2–2D1D	200	6.16	302	326	337
08	15.7	21.2	59.4	3.6	1,600	G_2–2D2D	100	8.87	157	165	171
09	21.9	53.9	21.0	3.3	1,600	G_2–2D2D	300	8.62	337	369	385
10	55.4	26.8	14.9	3.0	1,200	G_2–2D1D	100	8.07	152	172	192
11	49.1	41.8	7.9	1.2	1,600	G_2–2D1D	100	19.08	160	193	207
12	79.2	12.4	3.2	5.2	800	G_1–1D	0	22.73	91	91	91
13	18.4	74.6	3.4	3.6	1,600	G_2–2D1D	200	9.08	403	407	412
14	21.7	58.5	17.1	2.7	1,200	G_2–2D2D	100	11.96	256	265	273

Table S7. 10 fabrication parameter sets of G_1/G_2 stretchable nanocomposites to examine the model's prediction accuracy.

	Composition Labels				Thickness Labels	Deformation Labels	Strain Labels	Electrical Labels	Response Labels		
Recipe #	MXene Loading (wt.%)	SWNT Loading (wt.%)	AuNP Loading (wt.%)	PVA Loading (wt.%)	Thickness (nm)	Deformation Sequence	Pre-Strain (%)	S_0 (mS)	$\varepsilon_{5\%}$ (%)	$\varepsilon_{7.5\%}$ (%)	$\varepsilon_{10\%}$ (%)
1	44.0	39.4	6.1	10.6	1,600	G_1–1D	0	8.48	74	74	76
2	20.0	61.0	15.0	4.0	1,200	G_1–1D	0	5.57	67	67	67
3	27.3	54.3	13.7	4.8	800	G_1–2D	0	13.55	38	42	45
4	47.7	19.6	31.4	1.2	800	G_1–2D	0	13.51	62	64	66
5	41.8	49.1	7.9	1.2	1,600	G_2–2D1D	100	19.08	164	200	219
6	74.6	18.4	3.4	3.6	1,600	G_2–2D1D	200	9.08	388	409	407
7	68.4	19.8	7.0	4.7	1,600	G_2–2D1D	300	8.14	504	521	550
8	58.5	21.7	17.1	2.7	1,200	G_2–2D2D	100	119.62	246	261	274
9	47.8	42.0	3.6	6.6	1,200	G_2–2D2D	200	114.03	312	314	327
10	53.9	21.8	21.0	3.3	1,600	G_2–2D2D	300	86.21	355	365	400

Table S8. Correlation parameters used in the deflection functions of FE models.

Stretchable Nanocomposite	Buckling Mode	A (μm)	B (μm)	C (μm)	D (μm)	λ (μm)
G_1–1D	Cylindrical	16	0	0	0	35
G_1–2D	Checkerboard	33	0	0	33	44
G_2–2D1D	Cylindrical	105	0	0	0	70
G_2–2D2D	Undulating	105	53	0	0	70

A, B, C, and D are the correlation parameters, λ is the wavelength characterized from Keyence microscope. The thicknesses of G_1/G_2 stretchable nanocomposites were set to be 800 nm.

Table S9. Summary of influential components identified in different data analysis methods.

Data Analysis Method	Electrical and Response Labels	
	S_0 (mS)	$\varepsilon_{10\%}$ (%)
Spearman's ρ Analysis	PVA Loading (–)	Deformation Sequence (+) Applied Pre-Strain (+)
SHAP Model Interpretation	MXene Loading (+) PVA Loading (–) Applied Pre-Strain (–)	Deformation Sequence (+) Applied Pre-Strain (+) MXene Loading (–)

Table S10. Comparison of our robotics/ML-integrated framework with the state-of-the-art works in the fields of stretchable conductors

Design Strategy	Fabrication Method	Building Block	Electrical Property at Relaxed State	Maximum Stretchability	$\varepsilon_{10\%}$	Durability	Ref.
Robotics/ML-integrated framework	Sequential deformation	MXene/SWNT/AuNP/ PVA + thin Au layer	2.5×10^6 S m^{-1}	1,300%	1,025%	80k cycles under 400% elongation 50k cycles under 600% elongation 20k cycles at 700% elongation	This work
Design of experiment	Heterogeneous blending	EGaIn + PU	2.1×10^6 S m^{-1}	4,100%	310%	15k cycles under 100% elongation 8k cycles under 300% elongation 1.2k cycles under 500% elongation	[12]
Design of experiment	Bilayer integration	EGaIn + VHB	2.1×10^6 S m^{-1}	1,000%	160%	1.5k cycles under 500% elongation	[13]
Design of experiment	Heterogeneous blending	EGaIn + SBS	1.8×10^6 S m^{-1}	1,800%	100%	150 cycles under elongation 200 cycles under 1,000% elongation 1k cycles under 500% elongation 25k cycles under 100% elongation	[14]
Design of experiment	Heterogeneous blending	EGaIn/Ag flakes + SIB	8.2×10^5 S m^{-1}	1,200%	100%	1k cycles under 100% elongation 550 cycles under 400% elongation	[15]
Design of experiment	Heterogeneous blending	EGaIn + 11-phosphonoundecyl acrylate	2.5×10^5 S m^{-1}	750%	320%	10k cycles under 100% elongation	[16]
Design of experiment	Bilayer integration	EGaIn + pp-TPU	2.3×10^6 S m^{-1}	2,260%	670%	10k cycles under 100% elongation	[17]
Design of experiment	Heterogeneous blending	EGaIn/Ag flakes + EVA	8.3×10^5 S m^{-1}	1,000%	150%	10k cycles under 800% elongation	[18]
Design of experiment	Heterogeneous blending	Ag flakes + Ecoflex	1.3×10^4 S m^{-1}	1,780%	11%	1k cycles under 50% elongation	[19]
Design of experiment	Heterogeneous blending	AgNW/CNT + PVDF	5.7×10^5 S m^{-1}	140%	15%	5k cycles under 20% elongation	[20]
Design of experiment	Heterogeneous blending	AgNW/Au + SBS	4.2×10^6 S m^{-1}	840%	10%	3k cycles under 30% elongation	[21]

Design of experiment	Heterogeneous blending	AuNP + PU	1.1×10^6 S m^{-1}	480%	4%	10k cycles under 5% elongation	[3]
Design of experiment	Heterogeneous blending	Ag flakes + PAA	3.7×10^4 S m^{-1}	250%	10%	1k cycles under 100% elongation	[22]
Design of experiment	Heterogeneous blending	Ag flakes + alginate/PAM hydrogel	1.4×10^5 S m^{-1}	1,000%	300%	200 cycles under 300% elongation	[23]
Design of experiment	Heterogeneous blending	Ag flakes + fluorine rubbers	4.0×10^5 S m^{-1}	400%	85%	547 cycles under 50% elongation	[24]
Design of experiment	Heterogeneous blending	PEDOT:PSS + STEC	3.4×10^5 S m^{-1}	800%	45%	1k cycles under 100% elongation	[25]
Design of experiment	Heterogeneous blending	PEDOT:PSS + PR	7.0×10^4 S m^{-1}	125%	25%	100 cycles under 40% elongation	[26]
Design of experiment	Heterogeneous blending	PEDOT:PSS + EMIM TCB	1.0×10^5 S m^{-1}	180%	20%	20 cycles under 40% elongation	[27]
Design of experiment	Heterogeneous blending	Graphene flakes + TPU	4.3×10^2 S m^{-1}	500%	300%	10k cycles under 300% elongation	[28]
Design of experiment	Heterogeneous blending	CNT/graphite + PDMS	1.3×10^2 S m^{-1}	150%	130%	1k cycles under 60% elongation	[29]
Design of experiment	Heterogeneous blending	CNT + PU	1.0×10^2 S m^{-1}	300%	30%	100 cycles under 80% elongation	[30]
Design of experiment	Bilayer integration	CNT + PDMS	1.1×10^5 S m^{-1}	150%	14%	10k cycles under 25% elongation	[31]

Abbreviations: SWNT – single-walled carbon nanotubes; AuNP– gold nanoparticle; PVA – poly(vinyl alcohol); EGaIn – eutectic gallium-indium; PU – polyurethane; EVA – ethylene vinyl acetate copolymer; SIB – styrene–isoprene block copolymers; SBS – poly(styrene-block-butadiene-block-styrene); pp-TPU – polyester polyol-rich thermoplastic polyurethane; VHB – very high bond; AgNW – silver nanowire; PAA – polyacrylamide alginate; CNT – carbon nanotube; PVDF – polyvinylidene fluoride; PAM – polyacrylamide; PEDOT:PSS – poly(3,4-ethylenedioxythiophene): poly(styrene sulfonate); PVDF – polyvinylidene fluoride; STEC – stretchability and electrical conductivity; EMIM TCB – 1-ethyl-3-methylimidazolium tetracyanoborate; PR – polyrotaxane; PDMS – polydimethylsiloxane.

Table S11. Fitted EIS parameters of stretchable Zn//MnO_2 batteries at different stretching states.

Stretching State	R_{int} (Ω)	R_{ct} (Ω)
0%	18.1	2.42
300%	17.2	2.86

Equivalent Circuit Model

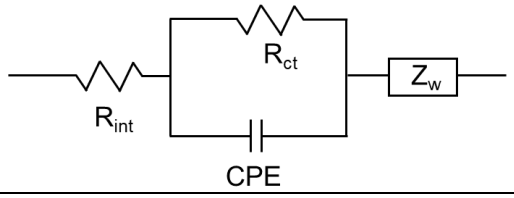

The parameters were obtained using the equivalent circuit model shown above, where R_{int}, R_{ct}, and Z_w represent the internal resistance, the charge transfer resistance, and the Warburg impedance that is related to the diffusion of Zn^{2+} at low frequencies, respectively. CPE is the constant phase element.

Table S12. Comparison of our stretchable Zn//MnO_2 battery with the state-of-the-art stretchable Zn-based and Li-ion batteries with co-planar configurations.

Stretchable Battery	Uniaxial Stretchability (%)	Electrolyte (Condition)	Specific Capacity at Relaxed State	Rechargeability	Ref.
Zn//MnO_2	300%	2.0 M $ZnSO_4$ 0.2 M $MnSO_4$ PVA Gel (Neutral)	260 mAh g^{-1} @ 100 mA g^{-1}	Yes	This work
Zn@Ti-MXene//V-MXene	50%	2.0 M $ZnCl_2$ 2.0 M LiCl PVA Gel (Neutral)	118.5 mAh g^{-1} @ 50 mA g^{-1}	Yes	[32]
Zn//MnO_2	50%	2.0 M $ZnSO_4$ 0.5 M $MnSO_4$ PAM Gel (Neutral)	75.6 mAh g^{-1} @ 308 mA g^{-1}	Yes	[33]
Zn//MnO_2	25%	40 wt.% KOH CMC Gel (Alkaline)	20.4 mAh g^{-1} @ 0.6 mA g^{-1}	No	[34]
Zn//MnO_2	50%	26 wt.% NH_4Cl 8 wt.% $ZnCl_2$ Xanthan Gel (Neutral)	3.5 mAh cm^{-2} @ 0.5 mA cm^{-2}	No	[35]
Zn//MnO_2	100%	PAA Gel (Alkaline)	2.3 mAh cm^{-2} @ 0.12 mA cm^{-2}	No	[36]
Zn//MnO_2	100%	6.0 M KOH 0.4 M ZnO PAA Gel (Alkaline)	3.8 mAh cm^{-2} @ 0.175 mA cm^{-2}	No	[37]

Zn//Ag	100%	6.0 M KOH 1.0 M LiOH PAA Gel (Alkaline)	2.5 mAh cm^{-2} @ 3 mA cm^{-2}	Yes	[38]
Zn//Ag	80%	10 M NaOH (Alkaline)	0.05 mAh cm^{-2} @ 1.0 mA cm^{-2}	Yes	[39]
Zn//Ag	11.1%	6.0 M KOH 1.0 M LiOH PAA Gel (Alkaline)	0.6 mAh cm^{-2} @ 0.15 mA cm^{-2}	Yes	[40]
Zn//Ni-Co	50%	1.0 M KOH 0.02 M $Zn(Ac)_2$ 0.005 M LiOH 0.005 M $Ca(OH)_2$ PVA Gel (Alkaline)	105 mAh g^{-1} @ 1.0 A g^{-1}	Yes	[41]
V_2O_5//LMO	50%	10 M LiTFSI (Neutral)	100 mAh g^{-1} @ 120 mA g^{-1}	Yes	[42]
AC//LMO	100%	1.0 M Li_2SO_4 (Neutral)	90 mAh g^{-1} @ 1.8 A g^{-1}	Yes	[43]

Abbreviations: PVA – poly(vinyl alcohol); PAM – polyacrylamide; CMC – carboxymethyl cellulose sodium salt; PAA – polyacrylic acid; Ac – acetate, [CH_3COO^-]; LMO – $LiMn_2O_4$; LiTFSI – lithium bis(trifluoromethanesulfonyl)imide; AC – active carbon.

Movie S1. Automated pipetting robot for preparing various MXene/SWNT/AuNP/PVA mixtures.

Movie S2. FE simulation of G_2–2D1D and G_2–2D2D stretchable nanocomposites under uniaxial elongations in top and perspective views.

Supporting Reference

1 Wang, J., Ma, X., Zhou, J., Du, F. & Teng, C. Bioinspired, high-strength, and flexible mxene/aramid fiber for electromagnetic interference shielding papers with joule heating performance. *ACS Nano* **16**, 6700–6711 (2022).

2 Cai, L. *et al.* Highly transparent and conductive stretchable conductors based on hierarchical reticulate single-walled carbon nanotube architecture. *Adv. Funct. Mater.* **22**, 5238–5244 (2012).

3 Kim, Y. *et al.* Stretchable nanoparticle conductors with self-organized conductive pathways. *Nature* **500**, 59–63 (2013).

4 Awad, M. & Khanna, R. *Efficient learning machines: theories, concepts, and applications for engineers and system designers* (Springer Nature, 2015).

5 Head, T., Kumar, M., Nahrstaedt, H., Louppe, G. & Shcherbatyi, I. Scikit-optimize/scikit-optimize: V0.9.0. (2021).

6 Audoly, B. & Boudaoud, A. Buckling of a stiff film bound to a compliant substrate—part ii. *J. Mech. Phys. Solids* **56**, 2422–2443 (2008).

7 Cai, S., Breid, D., Crosby, A. J., Suo, Z. & Hutchinson, J. W. Periodic patterns and energy states of buckled films on compliant substrates. *J. Mech. Phys. Solids* **59**, 1094–1114 (2011).

8 Huang, R. *Mechanical self-assembly: Science and applications* 69–109 (Springer, 2012).

9 Inc, T. Matlab version: 9.13.0 (r2022b). *The MathWorks Inc* (2022).

10 Yang, H. *et al.* Wireless $Ti_3C_2T_x$ MXene strain sensor with ultrahigh sensitivity and designated working windows for soft exoskeletons. *ACS Nano* **14**, 11860–11875 (2020).

11 Chen, T. *et al.* Machine intelligence-accelerated discovery of all-natural plastic substitutes.

Nat. Nanotechnol. (2024).

12 Lee, W. *et al.* Universal assembly of liquid metal particles in polymers enables elastic printed circuit board. *Science* **378**, 637–641 (2022).

13 Liu, S., Shah, D. S. & Kramer-Bottiglio, R. Highly stretchable multilayer electronic circuits using biphasic gallium-indium. *Nat. Mater.* **20**, 851–858 (2021).

14 Ma, Z. *et al.* Permeable superelastic liquid-metal fibre mat enables biocompatible and monolithic stretchable electronics. *Nat. Mater.* **20**, 859–868 (2021).

15 Lopes, P. A., Santos, B. C., de Almeida, A. T. & Tavakoli, M. Reversible polymer-gel transition for ultra-stretchable chip-integrated circuits through self-soldering and self-coating and self-healing. *Nat. Commun.* **12**, 4666 (2021).

16 Thrasher, C. J., Farrell, Z. J., Morris, N. J., Willey, C. L. & Tabor, C. E. Mechanoresponsive polymerized liquid metal networks. *Adv. Mater.* **31**, 1903864 (2019).

17 Chen, S. *et al.* Ultrahigh strain-insensitive integrated hybrid electronics using highly stretchable bilayer liquid metal based conductor. *Adv. Mater.* **35**, 2208569 (2023).

18 Wang, J. *et al.* Printable superelastic conductors with extreme stretchability and robust cycling endurance enabled by liquid-metal particles. *Adv. Mater.* **30**, 1706157 (2018).

19 Kim, S. H. *et al.* Ultrastretchable conductor fabricated on skin-like hydrogel-elastomer hybrid substrates for skin electronics. *Adv. Mater.* **30**, 1800109 (2018).

20 Chun, K. Y. *et al.* Highly conductive, printable and stretchable composite films of carbon nanotubes and silver. *Nat. Nanotechnol.* **5**, 853–857 (2010).

21 Choi, S. *et al.* Highly conductive, stretchable and biocompatible Ag-Au core-sheath nanowire composite for wearable and implantable bioelectronics. *Nat. Nanotechnol.* **13**, 1048–1056 (2018).

22 Ohm, Y. *et al.* An electrically conductive silver–polyacrylamide–alginate hydrogel composite for soft electronics. *Nat. Electron.* **4**, 185–192 (2021).

23 Hui, Y. *et al.* Three-dimensional printing of soft hydrogel electronics. *Nat. Electron.* **5**, 893–903 (2022).

24 Matsuhisa, N. *et al.* Printable elastic conductors by *in situ* formation of silver nanoparticles from silver flakes. *Nat. Mater.* **16**, 834–840 (2017).

25 Wang, Y. *et al.* A highly stretchable, transparent, and conductive polymer. *Sci. Adv.* **3**, e1602076 (2017).

26 Zhang, Z. *et al.* High-brightness all-polymer stretchable led with charge-trapping dilution. *Nature* **603**, 624–630 (2022).

27 Teo, M. Y. *et al.* Highly stretchable and highly conductive PEDOT:PSS/ionic liquid composite transparent electrodes for solution-processed stretchable electronics. *ACS Appl. Mater. Interfaces* **9**, 819–826 (2017).

28 Park, H. J. *et al.* Fluid-dynamics-processed highly stretchable, conductive, and printable graphene inks for real-time monitoring sweat during stretching exercise. *Adv. Funct. Mater.* **31**, 2011059 (2021).

29 Zhang, F. *et al.* 3D interconnected conductive graphite nanoplatelet welded carbon nanotube networks for stretchable conductors. *Adv. Funct. Mater.* **31**, 2107082 (2021).

30 Shin, M. K. *et al.* Elastomeric conductive composites based on carbon nanotube forests. *Adv. Mater.* **22**, 2663–2667 (2010).

31 Lipomi, D. J. *et al.* Skin-like pressure and strain sensors based on transparent elastic films of carbon nanotubes. *Nat. Nanotechnol.* **6**, 788–792 (2011).

32 Li, Y. *et al.* Stretchable Zn-ion hybrid battery with reconfigurable V_2CT_x and $Ti_3C_2T_x$

MXene electrodes as a magnetically actuated soft robot. *Adv. Energy Mater.* **11**, 2101862 (2021).

33 Liu, T., Chen, X., Tervoort, E., Kraus, T. & Niederberger, M. Design and fabrication of transparent and stretchable zinc ion batteries. *ACS Appl. Energy Mater.* **4**, 6166–6179 (2021).

34 Kettlgruber, G. *et al.* Intrinsically stretchable and rechargeable batteries for self-powered stretchable electronics. *J. Mater. Chem. A* **1**, 5505–5508 (2013).

35 Kaltenbrunner, M., Kettlgruber, G., Siket, C., Schwodiauer, R. & Bauer, S. Arrays of ultracompliant electrochemical dry gel cells for stretchable electronics. *Adv. Mater.* **22**, 2065–2076 (2010).

36 Zhu, H.-W. *et al.* Dip-coating processed sponge-based electrodes for stretchable Zn-MnO_2 batteries. *Nano Res.* **11**, 1554–1562 (2018).

37 Gaikwad, A. M. *et al.* Highly stretchable alkaline batteries based on an embedded conductive fabric. *Adv. Mater.* **24**, 5071–5076 (2012).

38 Kumar, R. *et al.* All-printed, stretchable Zn-Ag_2O rechargeable battery *via* hyperelastic binder for self-powering wearable electronics. *Adv. Energy Mater.* **7**, 1602096 (2016).

39 Yan, C. *et al.* Stretchable silver-zinc batteries based on embedded nanowire elastic conductors. *Adv. Energy Mater.* **4**, 1301396 (2013).

40 Berchmans, S. *et al.* An epidermal alkaline rechargeable Ag–Zn printable tattoo battery for wearable electronics. *J. Mater. Chem. A* **2**, 15788–15795 (2014).

41 Guo, Z. H. *et al.* Stretchable textile rechargeable zn batteries enabled by a wax dyeing method. *Adv. Mater. Technol.* **5**, 2000544 (2020).

42 Chen, Z.-F. *et al.* A thin, intrinsically stretchable MXene-MWCNTs/polymer current

collector for deformable aqueous Li-ion batteries. *J. Mater. Chem. A* **12**, 2444–2455 (2024).

43 Song, W. J. *et al.* Jabuticaba-inspired hybrid carbon filler/polymer electrode for use in highly stretchable aqueous Li-ion batteries. *Adv. Energy Mater.* **8**, 1702478 (2018).